Fluorinated Metal Complexes as MRI Contrast Agents

A THESIS SUBMITTED TO THE FACULTY OF THE
UNIVERSITY OF MINNESOTA
BY

Evan August Weitz

IN PARTIAL FULFILLMENT OF THE REQUIREMENTS
FOR THE DEGREE OF
DOCTOR OF PHILOSOPHY

Valérie C. Pierre, Adviser

August, 2015

Acknowledgements

i. I would like to thank my adviser, Prof. Valérie Pierre for her continuous support and guidance. Dr. Pierre has always provided excellent ideas and suggestions for scientific research and has kept me motivated at all times. Providing opportunities to learn and to develop my skills in all scientific disciplines is only a part of what Dr. Pierre has done for me in establishing a strong scientific discipline.

ii. I would also like to thank Prof. Mark Distefano for accepting to serve as chair on my examination committee, and Prof. Will Pomerantz and Prof. Rick Wagner as well for participating on my committee.

iii. To Sylvie Pailloux I extend my utmost gratitude in formatting this thesis for submission to the Department and the University.

iv. I would also like to thank Dr. Letitia Yao for her support and advice for acquiring paramagnetic ^{19}F NMR profiles and guidance in analyzing complicated ^{19}F NMR data. Also, allowing me to use the magnets for long time periods and at high temperatures is also appreciated.

v. Colleagues of the Pierre group I would like to thank for providing critical information reported in this thesis include: Cutler Lewandowsky, for his synthesis of F-DOTPME and *in vivo* studies and analysis of biodistribution; Dr. Kriti Srivastava, for growing crystals of metal complexes that were analyzed by X-ray crystallography, and obtaining DFT calculations; Dr. Vic Young for his extensive analysis and resolution of fluorinated metal complexes; and Dr. Katie Peterson for providing and explaining theoretical parameters of the complexes.

vi. Collaborators at the University of Minnesota I would like to thank include: Dr. Małgorzata Marjańska at the Center for Magnetic Resonance Imaging for days and nights of acquiring ^{19}F phantom images; and Dr. Henry Wong for providing his expertise for *in vivo* studies, working with the animals, and systematic, biological experiments with live rats.

vii. Collaborators outside the University of Minnesota include: Prof. David Parker in Durham, England, for providing me a free trip to Durham to sit down at the magnets for three weeks collecting T_1 data, as well as providing me with his own perspective in the field; Prof. Mauro Botta in Alessandria, Italy for tuning his fast-field-cycling device to ^{19}F and acquiring data at low field, as well as providing NMRD profiles of metal complexes and his perspective in the field.

viii. I'd like to thank all members of the Pierre Group, in no particular order: Katie, Cutler, Eric, Sylvie, Kriti, Sarah, Sam, Thakshila, Jen, Adam, Elizabeth, and Che.

ix. Finally I'd like to thank my parents for supporting me through the course of graduate school.

x. This research would not be possible without funding sources, which include the Chemical Biology Graduate Training Grant and a Wayland E. Noland fellowship awarded to EAW and an NSF CAREER (CHE-1151665) grant and CTSI Pilot II grant, awarded to VCP.

Dedicated to Mom and Pop

ABSTRACT

Magnetic resonance imaging (MRI) is a vital tool in today's modern healthcare system. MRI is preferred over positron emission tomography (PET) and X-ray computed tomography (CT) because it is non-invasive, non-radioactive, and provides 3-D imaging directly *in vivo*.

Contrast agents are used in order to enhance the resolution of the images from MRI. All currently used contrast agents are based on gadolinium and image water protons in the human body. However, gadolinium-based contrast agents are principally unable to quantitatively image specific biomarkers of diseased states, lacking a ratiometric mechanism.

Fluorine-based MRI does not suffer from these limitations, but its low sensitivity, with a limit of detection (LOD) in the micromolar range first requires a contrast agent designed specifically to address this issue of sensitivity, which can be accomplished using contrast agents with an incorporated lanthanide center.

Fluorine MRI eliminates background signals and has a large chemical shift range which enables fluorines in different environments to each be imaged independently. This in turn allows for the development of ratiometric, responsive contrast agents whereby the total probe concentration and the concentration of the analyte can be independently determined.

In this thesis, the theory, practicality, utility, and potential for fluorine-based MRI contrast agents is described. Sensitivity is addressed, synthesis is described, and demonstrations of the potential for fluorine MRI are examined *in vitro* and *in vivo* in order to design highly-sensitive, responsive, and biocompatible fluorine contrast agents.

Table of Contents

Acknowledgements ..... **i**

ABSTRACT ..... **iii**

List of Figures: ..... **vii**

List of Schemes: ..... **xiv**

List of Tables: ..... **xvi**

List of Abbreviations: ..... **xix**

1 Introduction **1**

1.1 Basic Principles of MRI **1**
1.1.1 Magnetic Field, and Nuclear Precession, the Radio-Frequency Pulse 1
1.1.2 T_1 and T_2 Relaxation 2
1.1.3 The MRI Experiment 4
1.1.4 MRI Contrast Agents 4
1.2 Two Major Classes of Clinical MRI Contrast Agents **5**
1.2.1 Contrast Agents Based on Gadolinium 5
1.2.2 Contrast Agents Based on Magnetic Iron-Oxide Nanoparticles (MIONs) 8
1.3 Other MRI Contrast Agents **9**
1.3.1 Contrast Agents Based on Manganese 9
1.4 Fluorine MRI Contrast Agents **11**
1.4.1 Desirable MR Properties of ^{19}F 11
1.4.2 Considerations of ^{19}F Imaging 12
1.4.3 Current ^{19}F Contrast Agents 12
1.4.4 Limits to Degree of ^{19}F Labeling 18
1.4.5 How To Address These Issues 18
1.4.6 Metal-Based ^{19}F MRI Contrast Agents 19
1.5 Responsive or "Smart" Contrast Agents **22**
1.5.1 The Importance of a Ratiometric Response 22
1.5.2 Responsive Gd(III)-Based Contrast Agents 24
1.5.3 Responsive MION-Based Contrast Agents 24
1.5.4 Responsive ^{19}F-Based Contrast Agents 26
1.5.5 Current Responsive Metal-Based ^{19}F MRI Contrast Agents 29
1.6 Proposed ^{19}F Metal-Based Complexes and Project Aims **31**

2 Design of Metal-Based ^{19}F MRI Contrast Agents—Optimizing Magnetic Resonance Properties **31**

2.1 Introduction **31**
2.2 ^{19}F Signal Intensity **32**

2.3 Limitations of Reported ^{19}F Responsive Probes 33
2.4 DOTAm-F12 Metal Complexes 34
2.4.1 Synthesis of DOTAm-F12 Metal Complexes 36
2.4.2 Using Fe(II) as the Paramagnetic Metal 36
2.4.3 Characterization of [M-DOTAm-F12]$^{2+/3+}$ Complexes and Resultant MR Properties 37
2.4.4 Lanthanide-Induced Shift and Bleaney Theory 39
2.4.5 Determination of Coordinated Water Molecules (q) 41
2.4.6 X-Ray Crystallography 42
2.5 Paramagnetic Relaxation Enhancement in Water 51
2.5.1 Signal Enhancement in an MR Image 55
2.6 Conclusions and Future Directions 63
2.7 Experimental Materials and Methods 66

3 Optimization of ^{19}F Paramagnetic Relaxation Enhancement: Lanthanide-Induced Shift, Effective Magnetic Moment, and BRW Theory Minimizations 75

3.1 Introduction 75
3.2 To Determine Ideal ^{19}F Probes for MRI 76
3.3 Three Ligands, Six Lanthanides 77
3.3.1 Synthesis of Metal Complexes 78
3.4 Lanthanide-Induced Shift 80
3.4.1 ^{19}FLIS of DOTAm-F12 Complexes 81
3.4.2 ^{19}FLIS of DOTA-F6 Complexes 82
3.4.3 ^{19}FLIS of F-DOTPME Complexes 82
3.5 Electronic Relaxation Rates (T_{1e}) 83
3.5.1 Experimental Relaxation Data 83
3.5.2 Application of BRW Theory to Determine T_{1e} and μ_{eff} - Data Minimization 86
3.5.3 Analysis of Data Fitted to Classic BRW Theory 90
3.5.4 Approximation of τ_R and d from BRW Theory and Drawbacks of Global Minimization 91
3.6 Other Methods Used to Determine τ_R and d 92
3.6.1 Determination of τ_R Using NMRD and [Gd-DOTAm-F12]$^{3+}$ 92
***3.7* Minimization of Data Using Known Values of τ_R and d 94**
3.7.1 Results 94
3.7.2 Analysis of Each Approach 96
3.7.3 Additional Experiments to Determine μ_{eff} and d 97
3.8 Conclusions and Future Work 97
3.9 Experimental Materials and Methods 98

4 A Responsive ^{19}F MRI Contrast Agent for Detection of Cu(I) 107

4.1 Introduction 107
4.2 Challenges of Copper Detection 108
4.3 Tm-DOTA-Click 108
4.4 Synthesis of Tm-DOTA-Click 111
4.5 Analysis of MR Properties for Tm-DOTA-Click 112
4.5.1 ^{19}F Lanthanide-Induced Shift (^{19}FLIS) 112
4.5.2 ^{19}F Paramagnetic Relaxation Enhancement (^{19}FPRE) Response 116

4.5.3 Sensitivity 118
4.5.4 Demonstration of Effective and Sensitive Response to Cu(I) 119
4.5.5 Drawbacks of a Catalytic Response Mechanism 121
4.6 Conclusions 121
4.7 Experimental Materials and Methods 122
4.7.1 General Considerations 122
4.7.2 Chemical Synthesis of Tm-DOTA-Click 123

5 *In Vivo* Analysis of ^{19}F MRI Contrast Agents 132

5.1 Introduction 132
5.1.1 ^{19}F MRI Contrast Agents Used for *in vivo* Studies—Structure 132
5.1.2 Synthesis of Contrast Agents 136
5.1.3 ^{19}F Relaxation Times 137
5.1.4 ^{19}F Signal Intensity 139
5.2 Preliminary *In Vivo* Experiments 140
5.2.1 Acute Toxicity of DOTAm-F12 Complexes 141
5.2.2 Four New Contrast Agents with Reduced Charge 141
5.3 Biodistribution Properties 142
5.3.1 Blood Retention 142
5.3.2 Organ Distribution 145
5.4 Imaging ^{19}F Contrast Agents Directly *In Vivo* 147
5.5 Conclusions and Future Work 148
5.6 Experimental Materials and Methods 149
5.6.1 Synthesis of F-DOTPME (3-14), DOTAm-F12-PO_3 (5-13), and Metal Complexes 150
5.6.2 Testing For Free Metal Ions 156
5.6.3 *In Vivo* Procedures 157
5.6.4 Determination of Fluorine Concentration 158

List of Figures:

Figure 1-1: Schematic of MRI spin echo RF pulse sequence and relaxation recording. (Figure used with permission from Pierre, V. C.).....3

Figure 1-2: Structures of 1) Magnevist (Gd-DTPA), 2) Dotarem (Gd-DOTA), and 3) Vasovist (MS-325), each with one water molecule coordinated to the Gd(III) center.....6

Figure 1-3: Lab Labels provided by :http://commons.wikimedia.org/wiki/ File:Bluthirnschranke_nach_Infarkt_nativ_und_KM.png, provided by: http://commons.wikimedia.....7

Figure 1-4: Structure of Mn-DPDP.....10

Figure 1-5: Examples of perfluorocarbons used as MRI contrast agents: 1) Perfluorobenzene, 2) Perfluoro-Octylbromide (PFOB), and 3) Perfluoro-15-crown-5. 14

Figure 1-6: NMR Spectra and gradient-echo phantom images of perfluorooctylbromide (PFOB) and perfluoro-15-crown-5. Images reproduced from Srinivas et. al. and used with permission. Table design reproduced from Wolters et. al16

Figure 1-7: FSB, both Flaherty molecules (unnamed): Chemical structures of FSB, and their further derivatives as produced by Flaherty et al. 17

Figure 1-8: The responsive MION agent, selective for Cu(I), shows in green a non-linear response, while the 100 μM trace in blue doesn't follow any pattern related to the other four traces. Reproduced from Smolensky et al. (Dalton Trans., 2012, 41, 8039). 26

Figure 1-9: Mizukami Peptide Gd OCF_3 Complex: In this image of Mizukami's gadolinium probe, the metal is complexed with a DO3A ligand, connected to a short

peptide, and terminating with a para-trifluoromethyl group. The fluorine reporter group is highlighted in blue while the amide bond that is cleaved by the enzyme is highlighted in red. 30

Figure 2-1: Chemical structures of DOTAm-F12 (2-1) and [M-DOTAm-F12]$^{2+/3+}$ complexes. M = La (III) (2-2), Eu (III) (2-3), Gd (III) (2-4), Tb (III) (2-5), Dy (III) (2-6), Ho (III) (2-7), Er (III) (2-8), Tm (II)I (2-9), Yb (III) (2-10), and Fe (II) (2-11). 35

Figure 2-2: ^{19}F NMR of M-DOTAm-F12 complexes (282 MHz, D_2O). Note that in the spectra of FeII-DOTAm-F12 the peak at δ_F = -79.4 ppm corresponds to the trifluoromethanesulfonate counter ion. 38

Figure 2-3: Chemical shift of ^{17}O of H_2O as a function of dysprosium complex concentration for [Dy-DTPA]$_2$- (filled square) and [Dy-DOTAm-F12]$^{3+}$ (open circle). The hydration number, q, for [Dy-DOTAm-F12]3+ was determined from the ratio of the slopes assuming q = 1 42

Figure 2-4: X-ray crystal structure of Tm-DOTAm-F12, side view (ORTEP, 50% probability level). Hydrogen and chlorine atoms omitted for clarity 43

Figure 2-5: X-ray crystal structure of Tm-DOTAm-F12, top view showing left-handed (Λ) helicity of pendant arms (ORTEP, 50% probability level). Hydrogen and chlorine atoms omitted for clarity 43

Figure 2-6: DFT-optimized structure of Tm-DOTAm-F12. The angle θ is defined by the Ln (III) – ^{19}F vector and the principle magnetic dipolar axis, which extends through the lanthanide ion into the center of the plane formed by the nitrogen atoms (represented by the dark green dummy atom). 44

Figure 2-7: The SAP geometry of Tm-DOTAm-F12 provides room for a coordinating water molecule. 49

Figure 2-8: Longitudinal relaxation rate of ^{19}F nuclei of Tm-DOTAm-F12 as a function of the applied magnetic field, B_0, and the rotational correlation time, τ_R. The analysis is based on Equation (3) and is done at 37 °C using the mean Tm-19F distance determined from X-ray crystallography (6.26 Å), assuming a magnetic moment, μeff, of 7.6 BM and an electronic relaxation time, τ_e, of 0.20 ps, values typical of TmIII complexes.....53

Figure 2-9: Transverse relaxation rate of ^{19}F nuclei of Tm-DOTAm-F12 as a function of the applied magnetic field, B_0, and the rotational correlation time, τ_R. The analysis is based on Equation (4) and is done at 37 °C using the mean Tm-^{19}F distance determined from X-ray crystallography (6.26 Å), assuming a magnetic moment, μ_{eff}, of 7.6 BM and an electronic relaxation time, τ_e, of 0.20 ps, values typical of Tm^{III} complexes. 53

Figure 2-10: MRI phantom images of $[M\text{-}DOTAm\text{-}F12]^{2+/3+}$ in water at 5.0 mM. B_0 = 9.4 T, T = 33 °C. A) ^1H 3D gradient-echo images, T_R = 10 ms, T_E = 1.78 ms, 20°, FOV: 20 mm × 40 mm × 20 mm, matrix: 128 × 256 × 128, resolution: 0.156 mm isotropic. ^{19}F gradient-echo images, T_R = 5 ms, T_E = 1.34 ms, 90°, FOV: 32 mm × 32 mm, matrix: 64 × 64, slice thickness = 10 mm, na = 64. Images are shown with the same intensity scale after 2D zero-padding. Transmitter offset for 19F images: -120 ppm KF; -86 ppm Yb, Tm; -78 ppm Fe, La, Er, Eu; 73 ppm Tb, Gd,; -62 ppm Ho, Dy. SNR for ^{19}F images: Yb, 20, Tm, 18; Fe, 40; La, 5.2; Er, 13; Eu, 7.8; Tb, 31; Gd, 1; Ho, 31; Dy, 6.0.....56

Figure 2-11: ^{19}F gradient-echo images in water. A) [Fe-DOTAm-F12]$^{2+}$ samples at three concentrations (0.5 mM, 1 mM, 5 mM, left to right), -73 ppm, T_R = 10 ms, T_E = 1.34 ms, 90°, FOV: 32 mm × 32 mm, matrix: 64 × 64, slice thickness = 10 mm, na = 512. SNR for Fe: 0.5 mM, 5.2; 1 mM, 9.9; 5 mM, 49. B) [Tm-DOTAm-F12]$^{3+}$ samples at three concentrations (0.5 mM, 1 mM, 5 mM, left to right), -86 ppm, T_R = 20 ms, T_E = 1.34 ms, 90°, FOV: 32 mm × 32 mm, matrix: 64 × 64, slice thickness = 10 mm, na = 256. Images are shown with the same intensity scale after two dimensional zero-padding. B_0 = 9.4 T, T = 33°C. SNR for Tm: 0.5 mM, 3.3; 1 mM, 6.6; 5 mM, 31.58

Figure 2-12: MRI phantom images of M-DOTAm-F12 in rat blood at 5.0 mM. B0 = 9.4 T, T = 33 °C. A) ^{1}H 3D gradient-echo images, T_R = 10 ms, T_E = 1.78 ms, 20°, FOV: 20 mm × 40 mm × 20 mm, matrix: 128 × 256 × 128, resolution: 0.156 mm isotropic. B) ^{19}F gradient-echo images, TR = 5 ms, TE = 1.34 ms, 90°, FOV: 32 mm × 32 mm, matrix: 64 × 64, slice thickness = 10 mm, na = 64. Images are shown with the same intensity scale after 2D zero-padding. Transmitter offset for ^{19}F images: -86 ppm Yb, Tm; -78 ppm Fe; -62 ppm Ho. SNR for 19F images: Yb, 4.6, Tm, 7.2; Fe, 34; Ho, ~1. 61

Figure 2-13: ^{19}F gradient-echo images of Ho-DOTAm-F12 in water (right) and rat blood (left). B_0 = 9.4 T, T = 33°C, T_R = 5 ms, T_E = 1.23 ms, 90°, FOV: 32 mm × 32 mm, matrix: 64 × 64, slice thickness = 10 mm, na = 512, 2D zero-padding.....61

Figure 2-14: ^{19}F gradient-echo images of A) Fe(II)-DOTAm-F12 and B) Tm DOTAm-F12 in rat blood at three concentrations (5 mM, 1 mM, 0.5 mM from left to right). B_0 = 9.4 T, T = 33°C, T_R = 10 ms, T_E = 1.34 ms, 90°, FOV: 32 mm × 32 mm, matrix: 64 × 64, slice thickness = 10 mm, na = 64. 2D zero-padding. Tm images are shown with

two times higher intensity than Fe images. SNR for Fe: 5 mM, 40; 1 mM, 8.8; 0.5 mM, 4.3. SNR for Tm: 5 mM, 8.2; 1 mM, 5.3; 0.5 mM, 2.3. 62

Figure 2-15: Three-dimensional ^{19}F MRI phantom images of M-DOTAm-F12 at 5.0 mM in rat blood. Samples are positioned as in Figure 2-14. B_0 = 9.4 T, T = 33 °C, TR = 15 ms, TE = 0.99 ms, 90°, FOV: 32 mm × 32 mm × 32 mm, matrix: 64 × 64 × 32, na = 64, acquisition time = 33 min. 63

Figure 3-1: Metal complexes used in this study: $[M\text{-}DOTAm\text{-}F12]^{3+}$ (2-2 to 2-10), $[M\text{-}DOTA\text{-}F6]^{-}$ (3-5 to 3-13), and $[M\text{-}F\text{-}DOTPME]^{-}$ (3-16 to 3-24).....78

Figure 3-2: Global minimization of μ_{eff}, T_{1e}, d, and τ_R based on R_1 data at six field strengths for DOTAm-F12 complexes.....87

Figure 3-3: Global minimization of μ_{eff}, T_{1e}, d, and τ_R based on R_1 data at five field strengths for DOTA-F6 complexes.....89

Figure 3-4: Global minimization of μ_{eff}, T_{1e}, d, and τ_R based on R_1 data at five field strengths for F-DOTPME complexes. 90

Figure 3-5: ^1H NMRD profiles (pH = 6.9) at different temperatures (298, 310 and 318 K). The curves are calculated with the parameters of table 3-8.....93

Figure 3-6: Minimization of $[Tm\text{-}DOTAm\text{-}F12]^{3+}$ using fixed d = 6.26 Å and τ_R = 89 ps. Minimization results in μ_{ef}f = 8.31 and T_{1e} = 0.19 ps. 94

Figure 3-7: Minimization of Tb(III), Dy(III), Ho(III), Er(III), Tb(III), and Yb(III) using fixed d = 6.26 Å and τ_R = 89 ps.....96

Figure 4-1: NMR spectra of a) the free ligand DOTA-click (3-11), b) Tm-DOTA-click (3-1) in the absence of Cu(I), and c) Tm-DOTA-click (1) after addition of 0.10 eq.

Cu(I)Asc. Note that it is necessary to maintain a long delay time in order to fully observe the aromatic ^{19}F nuclei of the probe in the absence of Cu(I). Experimental conditions: [Tm-DOTA-click] = 1 mM, water pH 7, B_0 = 11.7 T, pulse-acquire, T_R = 20 m. 113

Figure 4-2: MR spectra of Tm-DOTA-click in water a) in the absence of Cu(I) and b) after addition of 0.10 eq. Cu(I)Asc obtained with the 19FLIRE sequence. The aromatic ^{19}Fs of the probe in the absence of Cu(I) disappear due to the addition of an inversion time equal to $ln(2)\times T_{1\ (\text{aromatic F})}$ in the pulse sequence. Without this inversion time, the NMR spectrum in a would be identical to that of Figure 3b. The signal of the aromatic fluorines only reappear after reaction with Cu(I) due to a change in the conformation of the probe that shortens their T_1. Experimental conditions: [Tm-DOTA-click] = 1 mM, B_0 = 11.7 T 115

Figure 4-3: Ratiometric response of Tm-DOTA-click to Cu(I). I) water, II) Tm-DOTA-click (1) in water, III) Tm-DOTA-click (1) + 0.10 eq. Cu(I)Asc in water. a) T1-weighted 1H gradient echo image; 19F gradient echo images at b) -95 ppm and d) -145 ppm indicate indicate location of unreacted probe in the absence of Cu(I); ^{19}F gradient echo images at c) -60 ppm and e) -127 ppm indicate location of reacted probe in the presence of Cu(I). Experimental conditions: [Tm-DOTA-click] = 1 mM, B_0 = 16.4 T, na = (c) 512, (b, d, e) = 2048. 116

Figure 4-4: Pulse sequence used for ^{19}FLIRE-based signal silencing. Recycle delay (d1) = 1.2 s, 180˚ pulse (p180) = 32 ns, T_1(long) delay time (d2) = 340 ms, 90˚ pulse (pw) = 10 ns, acquisition time (at) = 64 ms. 117

Figure 5-1: ^{19}F MRI contrast agents for in vivo studies. Chemical structures of Three ligands used, six complexes 3-23 and 5-1, 2-9 and 2-11, and 5-2 to 5-3 explored as potential fluorine-based MRI contrast agents in this project. Each of three ligands was complexed with either Fe(II) or Tm(III). While the structures are similar, the six contrast agents each possess a different net charge (ranging from -2 to +3) and a slightly varied chemical structure, giving each compound unique pharmacological and magnetic properties. 133

Figure 5-2: Mean concentration of contrast agents in rat blood over 4 hours post-injection. Mean concentrations of ^{19}F in blood samples from rats injected with contrast agent indicated. Concentrations are given in units of parts per million (ppm), error bars represent standard deviation (n = 3). 145

Figure 5-3: Concentration of contrast agents within vital organs. This figure shows the mean percentage (n = 3) of total contrast agent injected that accumulated in each of the six vital organs examined in the experiment. The concentration of 19F in each organ was first determined in parts per million. Then, the mass of each organ and the total mass of fluorine contained in each 1 mL injection volume were used to determine the percentages shown. Error bars represent the standard error of the mean 147

List of Schemes:

Scheme 2-1 Synthesis of DOTAm-F12: aReagents and conditions: (a) K_2CO_3, H_2O/CH_2Cl_2, 1 h, 80.7%; (b) cyclen, K_2CO_3, CH_3CN, reflux, 8 h, 85.9%; (c) LnX_3, NaOH, $CH_3CN/CH_3OH/H_2O$, 75°C, 77-104 h, 98.0%-99.9%; (d) $Fe(OSO_2CF_3)_2$, CH_3CN/CH_3OH, 70°C, 30 h, quant. 36

Scheme 3-1: Reagents and conditions: (a) K_2CO_3, CH_3CN, reflux, 18 h, 60.0 %; (b) tBu bromoacetate, K_2CO_3, 45 ˚C, 16 h, 96.0 %; (c) NaOH (aq.), 1 h; (d) HCl (aq.), 1 h, 93.9 % over two steps; (e) LnX_3, H_2O, reflux, 3 days, quant.; (f) paraformaldehyde, acetic acid, benzene, rt, 3 d; (g) NaOH, H_2O, 100 ˚C, 30 min; 22 ˚C, 2 d, 29% over 2 steps; (h) LnX3, H2O, reflux, 3 days, quant. 79

Scheme 4-1: Chemical structure and proposed mode of action of the ratiometric fluorine responsive contrast agent for Cu(I), Tm-DOTA-click (4-1). Copper(I)-catalyzed cycloaddition clicks the terminal azide and acetylene groups together, inducing a conformational change that affects the chemical shift and longitudinal relaxation times of both the aliphatic (blue) and the aromatic (green) fluorines. The reactive functionality pair are indicated in purple 110

Scheme 4-2: Synthesis of Tm-DOTA-click (4-1); Reagents & conditions are as indicated. 111

Scheme 5-1: Synthesis of f-DOTPME and DOTAm-F9-PO_3. Experimental conditions: (a) hydrazine, EtOH, 22 ºC, 18 h -> reflux, 3 h, 45%; (b) bromoacetyl bromide, NaOH, CH_2Cl_2/H_2O, 0 ºC -> 22 ºC, 1 h, 60%; (c) cyclen, triethylamine, $CHCl_3$, 60 ºC, 18 h,

57%; (d) 2-bromo-*N*-(2,2,2-trifluoroethyl)acetamide, K_2CO_3, CH_3CN, 60 ºC, 18 h, 54%; (e) TMS-Br, DMF, 0 ºC -> rt, 18 h, 55%. 136

List of Tables:

Table 2-1: ^{19}F Chemical shift (δ), lanthanide induced shift (LIS, ΔδF), T_1 and T_2 relaxation times and MRI SNR of M-DOTAm-F12 complexes in water.....40

Table 2-2: Ln-F distances, d, and the angle, θ, between the lanthanide-fluorine vector and the principle magnetic dipolar axis of the Tm(III) center of Tm-DOTAm-F12 from X-ray structure and DFT calculation. 44

Table 2-3:Crystal data and structure refinement for [Tm-DOTAm-F12]$^{3+}$.....45

Table 2-4: Atomic coordinates (×104) and equivalent isotropic displacement parameters (Å2 × 103) for [Tm-DOTAm-F12]$^{3+}$. Ueq is defined as one third of the trace of the orthogonalized Uij tensor.....46

Table 2-5: Anisotropic displacement parameters (Å2 × 103) for [Tm-DOTAm-F12]$^{3+}$. The anisotropic displacement factor exponent takes the form: -2π2 [h2 a* 2U11 + ... + 2 h k a* b* U12].....47

Table 2-6: Hydrogen coordinates (× 104) and isotropic displacement parameters (Å2 × 103) for [Tm-DOTAm-F12]$^{3+}$. 48

Table 2-7: Calculated (DFT) total energy change for [Tm-DOTAm-F12]$^{3+}$ and [Tm DOTAm F12]$^{3+}$ • H2O forms of the complex. 50

Table 2-8: ^{19}F T_1 and T_2 relaxation times, T_2/T_1 ratio, and MRI SNR of M-DOTAm-F12 complexes in rat veinous blood at 37°C. 60

Table 3-1: Chemical shifts (δ, ppm) of DOTAm-F12, DOTA-F6, and F-DOTPME metal complexes, and change in chemical shift (Δδ, ^{19}FLIS) relative to the free ligand. aAverage chemical shifts from data acquired at 4.7, 9.4, 11.7, 14.1, and 16.5 T, 298 K.81

Table 3-2: T_1 values reported are averages of three measurements obtained within 5% difference or less for each value. 84

Table 3-3: T_1 values reported are averages of three measurements obtained within 5% difference or less for each value 85

Table 3-4: T_1 values reported are averages of three measurements obtained within 5% difference or less for each value. 85

Table 3-5: Global minimizations of μ_{eff}f, T_{1e} as a function of relaxation rates for DOTAm-F12 complexes. Subsequent iterations yielded the reported values for τ_R and *d*. 87

Table 3-6: Global minimizations of μ_{eff}, T_{1e} as a function of relaxation rates for DOTA-F6 complexes. Subsequent iterations yielded the reported values for τ_R and *d*..88

Table 3-7: Global minimizations of μ_{eff}, T_{1e} as a function of relaxation rates for F-DOTPME complexes. Subsequent iterations yielded the reported values for τ_R and [d]. .89

Table 3-8: Parameters obtained from the analysis of ^{17}O NMR and NMRD data[a] of $[Gd\text{-}DOTAm\text{-}F12]^{3+}$ 93

Table 3-9: Global minimizations of μ_{eff} and T_{1e} as a function of relaxation rates for DOTAm-F12 complexes, using an all-vary global fit, and then using fixed values of τ_R = 89 ps and *d* = 6.26 Å in a global fit. 95

Table 4-1: Chemical shift, δ, and longitudinal, T_1, and transverse, T_2, relaxation times of the signals of the aliphatic and aryl fluorine nuclei of Tm-DOTA-click (1) before and after reaction with Cu(I). Numbers in parentheses represent standard deviations, *n* = 3 113

Table 4-2: Percentage of Tm-DOTA-Click catalyzed by Cu(I) when incubated in D_2O for 2 h. The concentration of Cu(I) relative to the concentration of Tm-DOTA-Click is presented, as well as its net concentration. Mixtures of 0.1% Cu(I) or higher effectively catalyze all of the probe in the sample after 2 h incubation period. 120

Table 5-1: T_1 and T_2 relaxation values for ^{19}F nuclei. T_1 and T_2 values of the ^{19}F nuclei in the three precursor ligands and in their Tm(III) and Fe(II) complexes, measured in aqueous solution at neutral pH at 282 MHz. [a]Value found by Kim et al.[84] [b]Spectrum for 5-1 displayed multiple resonances corresponding to stereoisomers. axial and equatorial over a wide frequency range, each with distinct T_1 and T_2 values. [c]For compounds with spectra displaying two signals over a narrow frequency range (i.e. both could be imaged in a single MRI scan), individual relaxation time values are given for each signal. 138

Table 5-2: Summary of *in vivo* contrast agent injections. The blood half-life is the amount of time after injection at which half of the injected contrast agent was present in the blood, and the primary organs are those in which the highest concentrations of contrast agent were found four hours post-injection (p.i.).....143

List of Abbreviations:

^{19}FLIS	fluorine lanthanide-induced shift
^{19}FPRE	fluorine paramagnetic relaxation enhancement
5FU	5-fluorouracil
AD	Alzheimer's disease
Aβ	amyloid-beta
B. M.	Bohr magnetons
BRW	Block-Redfield-Wangsness
CPMG	Cargill-Purcell-Meiboom-Gill
CT	computed tomography
d1	recycle delay time
DFT	density functional theory
DOPA	1,4,7,10-tetraazacyclododecane triacetic acid phosphate
DOTA	1,4,7,10-tetraazacyclododecane
DOTA-F6	2,2'-(4,10-bis(carboxymethyl)-1,4,7,10-tetraazacyclododecane-1,7-diyl)bis(4,4,4-trifluorobutanoic acid)
DOTAm-F12	2,2',2",2'"-(1,4,7,10-tetraazacyclododecane-1,4,7,10-tetrayl)tetrakis(*N*-(2,2,2-trifluoroethyl)acetamide)
DOTAm/DOTAM	1,4,7,10-tetraazacyclododecane tetraamide
DPDP	dipyridoxal diphosphate
DTPA	diethylene triamine pentaacetic acid

F-DOTPME	tetrakis(2,2,2-trifluoroethyl) ((1,4,7,10-tetraazacyclododecane-1,4,7,10-tetrayl)tetrakis(methylene))tetrakis(hydrogen phosphonate)
FDA	Food and Drug Administration
FSB	(*E*,*E*)-1-fluoro-2,5-bis(3-hydroxycarbonyl-4-FSB hydroxy)styryl- benzene
GBCA	gadolinium-based contrast agent
GRASE	gradient-echo and spin-echo
GSH	glutathione
HP-DO3A	hydroxypropyl 1,4,7,10-tetraazacyclododecane triacetic acid
LIS	lanthanide-induced shift
MION	magnetic iron-oxide nanoparticles
MR	magnetic resonance
MRI	magnetic resonance imaging
MRS	magnetic resonance spectroscopy
NMR	nuclear magnetic resonance
NMRD	nuclear magnetic relaxation dispersion
NSF	nephrogeniy systemic fibrosis
PARACEST	paramagnetic chemical exchange saturation transfer
PCS	pseudocontact shift

PET	positron emission tomography
PFC	perfluorocarbon
PFOB	perfluoro-octylbromide
ppm	parts per million
PRE	paramagnetic relaxation enhancement
RF	radio frequency
SAP	square-antiprismatic
SNR	signal to noise
SPECT	single-photon emission computed tomography
SQUID	superconducting quantum interference device
SWIFT	sweep imaging with Fourier transform
TACN	1,4,7-triazonane
TGE	turbo gradient-echo
TSAP	twisted square-antiprismatic

1 Introduction

1.1 Basic Principles of MRI

Clinical diagnostics and biomedical research rely heavily on the ability to image the human body. Of particular interest to the medical community is magnetic resonance imaging (MRI), an imaging procedure that is non-invasive and does not expose the patient to high-power ionizing radiation in the case of X-ray or computed tomography (CT) scanning, radioactive isotopes in the case of positron emission tomography (PET), and offers better resolution than single-photon emission computed tomography (SPECT). MRI only minimally perturbs the subject, and offers full spatial and temporal imaging with higher resolution when compared to CT, PET, or SPECT. As a result, among imaging techniques that are clinically available, MRI stands as being especially promising and safe. The prognoses of many diseased states can be detected by MRI, and these results can allow medical analysis and subsequent treatment options to patients prior to advanced stages of diseases such as cancer, stroke, spina bifida, and multiple sclerosis, among others. In 2013, over 45 million MRI scans were performed in in the United States alone.[1]

1.1.1 Magnetic Field, and Nuclear Precession, the Radio-Frequency Pulse

In theory, any nucleus having an intrinsic magnetic moment and angular momentum resulting in a non-zero spin. can be imaged by MR. The most common nuclei are ^{1}H, ^{13}C, ^{19}F, and ^{31}P for nuclear magnetic resonance (NMR), but within the scope of MRI, imaging of ^{1}H is by far the most common and most widely used.

When MRI-active nuclei are placed in a powerful magnetic field, their nuclear spins align with the vector of the magnetic field, defined in 3-D space as the Z-axis. As the nuclear alignment along the Z-axis is established, the nuclei then precess about the Z-axis due to their intrinsic angular momentum but in summation retain alignment with the Z-axis. As shown in Figure 1-1, following magnetic alignment, a low-energy radio-frequency (RF) pulse on the order of microseconds distorts the precessing nuclei out of the Z-axis and in to the XY plane using an RF pulse, commonly 90˚. A 90˚ pulse deflects the precessing nuclei fully into the XY plane and depleting magnitude along the Z-axis, after the magnetic moments of the nuclei decay their magnitude in the XY plane and restore their magnitude along the Z-axis as the nuclei realign with the magnetic field. The times required for nuclei to relax are relaxation times.

1.1.2 T_1 and T_2 Relaxation

The longitudinal (spin-lattice) time, known as T_1, is a time constant measuring the time required for nuclei to restore their magnitude along the Z-axis following a 90˚ pulse. The transverse (spin-spin) time, T_2, is a second time constant measuring the time required for nuclei to deplete their magnitude in the XY plane following a 90˚ pulse. T_1 is measured by and inversion-recovery sequence while T_2 is measured by the Cargill-Purcell-Meiboom-Gill (CPMG) pulse sequence. The relaxation times are described as T_1 and T_2 are first order. The differences between the two are illustrated in Figure 1-1, where T_1 is represented as the restoring magnitude of the red arrow along the Z-axis, and T_2 is represented as the depleting magnitude of the red arrow in the XY-plane. Differences in chemical environments affect the relaxation times, which can be analyzed and processed in order to form an image.

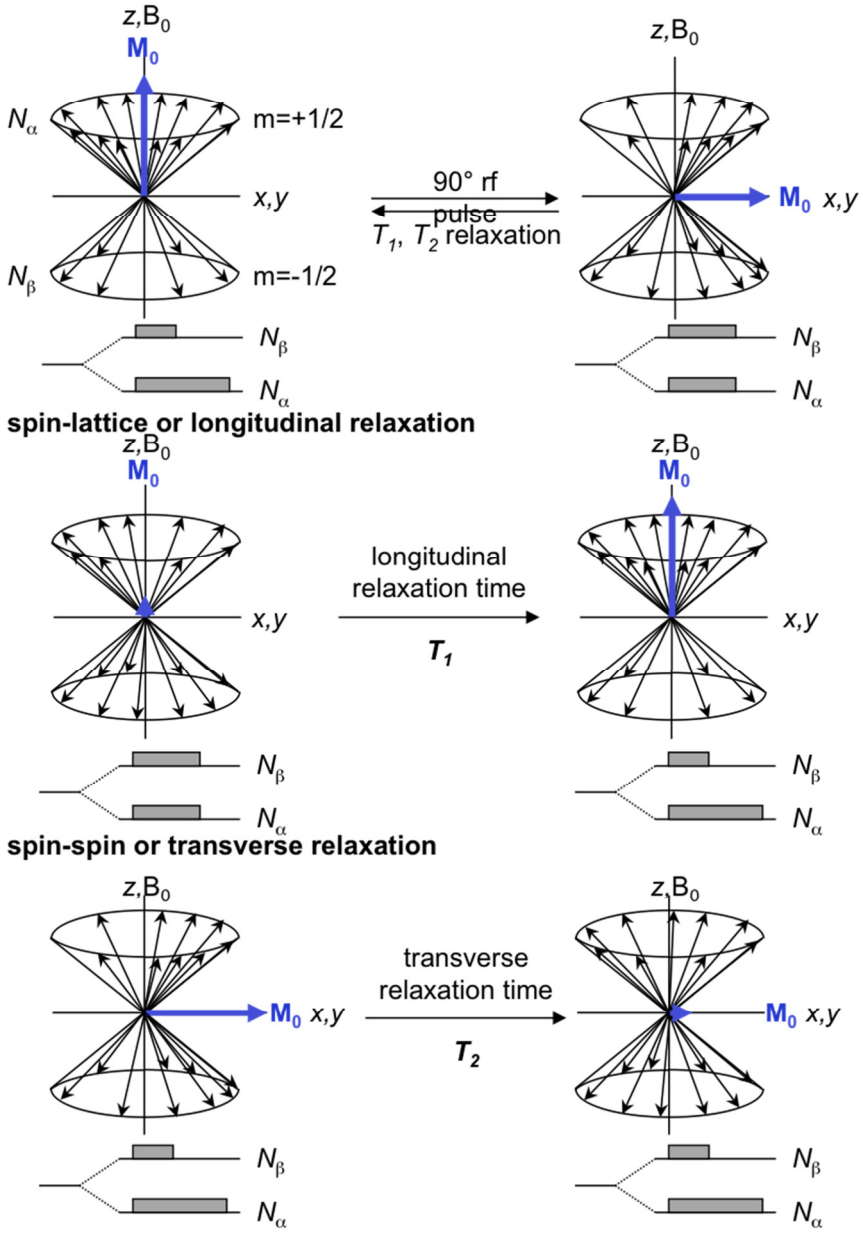

Figure 1-1: Schematic of MRI spin echo RF pulse sequence and relaxation recording. (Figure used with permission from Pierre, V. C.).

Work by Damadian *et al.* established that a sharp difference in T_1 relaxation is observed between normal and malignant tissues, with the greatest T_1 changes observed in breast, skin, intestine, stomach, and adipose tissues (Table 1.1).[2,3] Similar results

were observed by Hollis et al.[4] and Hazlewood et al.,[5] and it was presumed the shorter relaxation times of healthy tissues were a function of more rapid exchange of the coordinated water molecules in healthy tissues. Other explanations have been suggested over time but this initial conclusion is still the most accepted mechanism for longer T_1 times in cancer cells.

1.1.3 The MRI Experiment

Current clinical MRI procedures detect endogenous water protons in human patients. Three-dimensional images of patients are obtained by imaging slices that are then stacked in layers and are rendered with a computer to assemble a three-dimensional image.

The MRI pulse sequence defines a set of RF pulses, magnetic gradients, and delay times such as time to echo (T_E, the time between the RF pulse until the maximum signal returned from the gradient echos) and time to repetition (T_R, the time between each scan event). The gradient-echo pulse sequence is most commonly used in clinical MRI, and can be T_1-, T_2-, and/or T_2*-weighted, depending on what is being imaged and the type of image desired. It can also depend on whether MRI contrast agents are used.

1.1.4 MRI Contrast Agents

Contrast agents may also be used in the MRI procedure. Contrast agents are small magnetic compounds or are based on nanoparticles. that decrease the relaxation times (T_1 and T_2) of water protons and all other nearby nuclei, increasing contrast between regions where the contrast agent accumulates versus the background tissue signal. There are several mechanisms by which this can happen. First, in most cases

the contrast agent passively diffuses throughout the body, to different tissues and at different rates due to different associations between the interactions of the contrast agent with the organ it comes in contact with. These differences increase the contrast difference observed between various biological features. The magnetic effect of most contrast agents are provided by gadolinium(III)-based contrast agents (GBCA's) or magnetic iron-oxide nanoparticles (MION's), which enhance proton relaxation through diffusion or proton exchange with the bulk water solvent.

1.2 Two Major Classes of Clinical MRI Contrast Agents

1.2.1 Contrast Agents Based on Gadolinium

All FDA-approved and currently available contrast agents are based on gadolinium(III). Gadolinium(III) is a paramagnetic lanthanide metal that enhances the relaxation times of water protons in the body. In a typical Gd(III) contrast agent, the otherwise toxic Gd(III) ion is ligated with an organic molecule that occupies, in most cases, eight out of nine available coordination sites, with the last open coordination site filled by a water molecule. Several examples of such systems are illustrated in Figure 1-2.

The most pronounced relaxation enhancement involves the exchange of water molecules coordinated to the gadolinium center and their transfer to the bulk water solvent, decreasing relaxation times. This is known as "inner-sphere" relaxivity and accounts for over 60% of the relaxation enhancement.[6] The remaining relaxation enhancement is due to the "outer-sphere" contribution, which is the result of interactions between paramagnetic complexes and nearby water molecules.

Gadolinium(III) is the lanthanide of choice since Gd(III)'s electronic relaxation time is close to that of the ^{1}H oscillation frequency.[7]

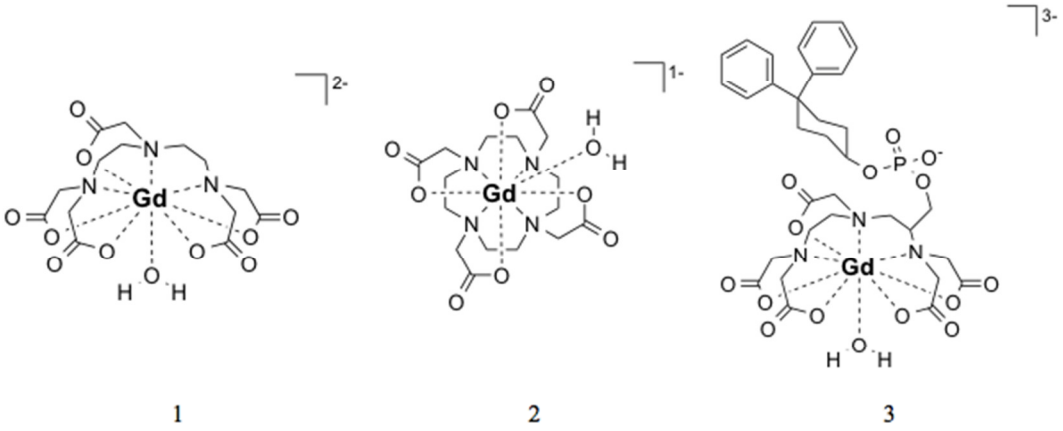

Figure 1-2: Structures of 1) Magnevist (Gd-DTPA), 2) Dotarem (Gd-DOTA), and 3) Vasovist (MS-325), each with one water molecule coordinated to the Gd(III) center.

In 1988, the first gadolinium-based contrast agent, Magnevist Figure 1-2, was approved for clinical use as an MRI contrast agent, and eight others have followed since then. These agents are not visualized directly nor do they have responsive elements. Though MS-325 targets liver and Eovist targets liver, they are still considered unresponsive. Regardless, these contrast agents enhance MR image resolution of differences between different tissues can often be more accurately resolved using a contrast agent. Their use is sometimes critically important. One example is depicted in Figure 1-3, where brain tissue that had undergone a stroke is only clearly observed after the use of a contrast agent, and this symptom of stroke might not otherwise be seen by MRI.

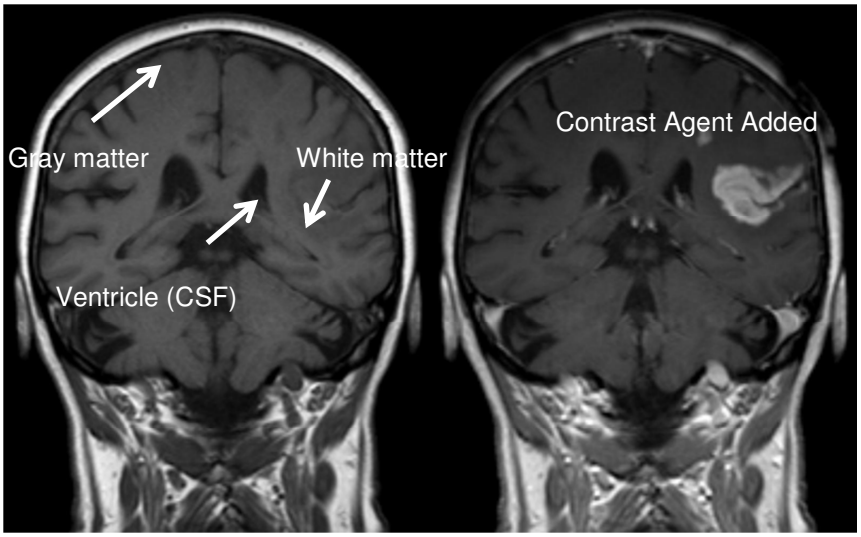

Figure 1-3: Lab Labels provided by :http://commons.wikimedia.org/wiki/File:Bluthirnschranke_nach_Infarkt_nativ_und_KM.png, provided by: http://commons.wikimedia.

1.2.1.1 Drawbacks of Gadolinium-Based Contrast Agents

The use of Gd(III) contrast agents raises toxicity concerns in those with kidney disease, specifically nephrogenic system fibrosis (NSF), wherein the contrast agent is not cleared from the body fast enough to eliminate any risks associated with the release or transmetallation of Gd(III) from the chelate. NSF is a serious illness that often is not detected.

And while Gd(III) has proven to be the most useful lanthanide metal to use for decreasing relaxation times in water protons in the bulk solvent, it's not necessarily the best paramagnetic metal used in the design of other types of contrast agents. Relaxation times of water protons also suffer a loss in relaxation time before further enhancement at about 1.0 T.[8]

1.2.2 Contrast Agents Based on Magnetic Iron-Oxide Nanoparticles (MIONs)

Another class of MRI contrast agents is based on magnetic, iron-oxide nanoparticles (MIONs). Several types of MIONs exist, consisting of magnetite (Fe_3O_4) or maghemite (Υ-Fe_2O_3) iron oxide particles, with many different sizes and surface functionalizations. These superparamagnetic nanoparticles are particularly effective at reducing the T_2 (spin-spin) relaxation times of water protons. Their use requires high concentrations comparable to GBCA's to allow for sufficient MRI contrast; typical administrative dosages of either type are 5-10 grams of contrast agent.[9-12] Most research on MIONs deals with tailoring the nanoparticles for use as blood-pool agents as well as surface functionalization to allow for improved cellular uptake and lower administrative concentrations.[10,13]

Concomitant with surface functionalization of MION's, other chemical reporters must be introduced in order to afford a viable, responsive contrast agent. The functionality and response of these agents is caused by the aggregation of the monomeric particles, causing decreases in both T_1 and T_2, and producing contrast in the MR image. While these agents have been widely documented in the literature, they remain experimental in that only one has been FDA-approved, and it is no longer manufactured for medical use.[14]

1.2.2.1 Drawbacks of MION's

Concomitant with surface functionalization of MION's, other chemical reporters must be introduced in order to afford a viable contrast agent for imaging a specific target. The functionality and response of these agents is caused by the aggregation of the monomeric particles, causing decreases in both T_1 and T_2, and

producing contrast in the MR image. While these agents have been widely documented in the literature, they remain experimental in that only one has been FDA-approved, and it is no longer manufactured for medical use.[14]

The aggregation states necessary for enhancing the MR image obtained are very desirable in order to differentiate between the observed contrast resolution. The aggregates desired are not readily formed in a system where the MION's would normally just passively diffuse throughout the biological system. While their distribution can be predicted, they are severely limited as unresponsive MR contrast agents, and for an unresponsive system, are demonstrated to be more challenging than the previously described Gd(III) agents in MR imaging. Their responsive derivatives, discussed later in chapter 1.5.3, are what have maintained interest in MION's as MRI contrast agents.

1.3 Other MRI Contrast Agents

1.3.1 Contrast Agents Based on Manganese

Multiple contrast agents have also been reported based on manganese. Two manganese-based contrast agents have been commercially available but are no longer marketed:

manganese(II) dipyridoxal diphosphate (Mn-DPDP, Teslascan), shown in

, is FDA-approved as an injection for liver imaging,[15] as well as orallyadministered manganese(II) chloride (LumenHance),[16] for general imaging purposes as well as imaging certain calcium efflux events.[17] While gadolinium agents have continually attracted more attention than manganese agents, the same reported toxicity issues such a nephrogenic systemic fibrosis (NSF) was reported in 2006 for

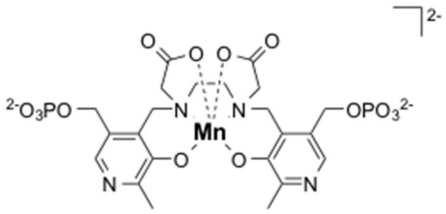

manganese agents.[18,19] This has decreased the interest of manganese, and further development of contrast agents based on manganese has been decreased.

Figure 1-4: **Structure of Mn-DPDP.**

Both free manganese(II) ion and chelated manganese(II or III) have severe safety concerns.[20-23] Free manganese(II) ion administered as buffered $MgCl_2$ for oral administration is nearly as toxic as gadolinium(III) with a toxicity of 0.5 mm/kg in rats.[24] Additionally, manganese(II) ions interfere and/or compete with endogenous calcium(II) ions in numerous biological processes, which are not fully understood. Chelated manganese(II) in most cases releases manganese(II) ions through displacement of the metal in the ligand by calcium(II) ions,[20] and the increased membrane permeability of manganese chelates results in undesirable and unpredictable biodistribution. Combined with excessively long clearance times, the safety of manganese-based contrast agents remains of issue.

Porphyrin derivatives have been commonly used as ligands for manganese-enhanced contrast.[25,26] Most recently Cheng *et. al.* have reported a manganese porphyrin dimer that binds to HSA with successful imaging in vivo at 3 T, however little change was observed at higher field strengths.[27] Qazi *et. al.* reported successful loading of a manganese porphyrin into a bacteriophage for targeted tumor delivery,[28] but found that the high resultant concentration of manganese resulted unexpectedly in only marginally-reduced relaxation rates over the same total concentration of contrast agent in a homogenous solution.

Both of these examples suggest that the contrast enhancement from manganese is fundamentally limited by concentration. While manganese agents have been used in non-targeted imaging, they are no longer commercially available, and the new developments with manganese are still in experimental stages. Safety issues such as instability in the presence of endogenous

Ca(II) ions and its deposition in fatty tissue represent severe limitations to their future development for clinical use as responsive contrast agents as well.

1.4 Fluorine MRI Contrast Agents

1.4.1 Desirable MR Properties of ^{19}F

Imaging ^{19}F by MRI has drawn considerable interest due in part to fluorine's MR properties. The ^{19}F nucleus is 100% naturally abundant, has high MR sensitivity (0.834 relative to ^{1}H),[29] and an extremely large chemical shift range (>350 ppm), making signal overlap from different ^{19}F nuclei extremely unlikely. Furthermore, the ^{19}F nucleus is virtually non-existent in biological systems, effectively eliminating background signals and producing greater contrast in the MR image. Small amounts of solid fluorides are found at various concentrations in teeth and bone, but are below MRI detection limits due to their low concentrations and extremely short T_2 relaxation times.[30] As a result, multiple fluorine labels can be detected individually, whether different labels are used in one contrast agent, or during simultaneous use of multiple ^{19}F contrast agents.

Fluorine also has a high gyromagnetic ratio of approximately 40 MHz per tesla, only 6% lower than ^{1}H. This is a critical advantage for ^{19}F MRI since clinical

magnets already in use today, could be adjusted to image ^{19}F. This requires only adjustments in tuning and experiment design and does not require a different probe.

1.4.2 Considerations of ^{19}F Imaging

The predominant issue in all classes of ^{19}F contrast agents is fluorine's low sensitivity in MRI. While the lack of background signals is advantageous in one regard, it is also a challenge to introduce ^{19}F contrast agents in sufficiently high concentrations for *in vivo* imaging. The concentrations required for ^{19}F MRI are in the millimolar range (ca. 10-50 mM), whereas ^{1}H MRI agents image endogenous water molecules up to 55 M.[31]

Fluorine also has considerably long relaxation times, with T_1 values of 0.5-3 seconds. This requires recycle delay times (**d1**'s) in MR pulse sequences to be 3-5 times T_1, resulting in scan repetition times of 3-6 s.[32] Such long repetition times, combined with the time limits for clinical imaging procedures (60 minutes or less), ultimately reduces sensitivity, and often prevents many proposed ^{19}F contrast agents from being clinically viable for MRI.[33,34]

1.4.3 Current ^{19}F Contrast Agents

1.4.3.1 Organic, Diamagnetic Fluorinated Molecules

The MRI contrast agents discussed thus far all detect the ^{1}H nuclei of endogenous water molecules, but MRI is not restricted to ^{1}H. MRI-active nuclei include ^{13}C, ^{15}N, ^{31}P, and of particular interest, ^{19}F. The concept of fluorine-based MRI was reported in 1977 by Holland et al.,[35] only four years after Lauterbur's demonstration of ^{1}H MRI in 1973.[36] Initially, the presence of ^{19}F nuclei in many drugs

prompted exploration in to ^{19}F MRI imaging. The anti-cancer medication 5-fluorouracil (5FU) was quickly identified as a molecule to image, with Wolf et al., performing the first experiment with that drug ten years later in 1987.[37] Further improvements for imaging 5FU have been made include superior spatial resolution[38] and further enhanced chemical shift changes of 5FU in different biological environments.[39]

Other fluorinated drugs are being continuously examined as potential ^{19}F imaging agents. The anti-depressant fluoxetine, the anesthetic haloperidol, and the benzodiazepine fluphenazine have drawn particular attention, having particularly short ^{19}F T_1 values compared to other fluorinated agents. The immediate advantage of imaging fluorinated drugs is that they have already proven to be safe and are approved in most countries, eliminating any synthetic work and essentially eliminating pharmacokinetic studies.

However, imaging fluorinated pharmaceuticals has not resulted in their conversion to also serve as MRI contrast agents, but have shown to be useful imaging agents in some cases. The most promising agents however still are met with imaging difficulty due to fluorine's low sensitivity, and they lack any design considerations that are otherwise used strictly to improve sensitivity and contrast. These design considerations are discussed further in section 1.4.2.

1.4.3.2 Perfluorocarbons

Another class of contrast agents have been developed, which are highly-fluorinated or perfluorinated small organic molecules (perfluorocarbons or PFC's), developed specifically for MR imaging. The structures of these molecules are simple

hydrocarbons that have been converted to their respective fluorocarbons. Several examples include perfluorobenzene, perfluoro-octylbromide (PFOB), and perfluoro-15-crown-5, which are depicted in Figure 1-5. Larger PFC's exist, but as the size of PFC's increase, obtaining MR contrast can decrease as well due to their decreased tumbling rates and thusly their decreased T_1, and in particular, their T_2 values.

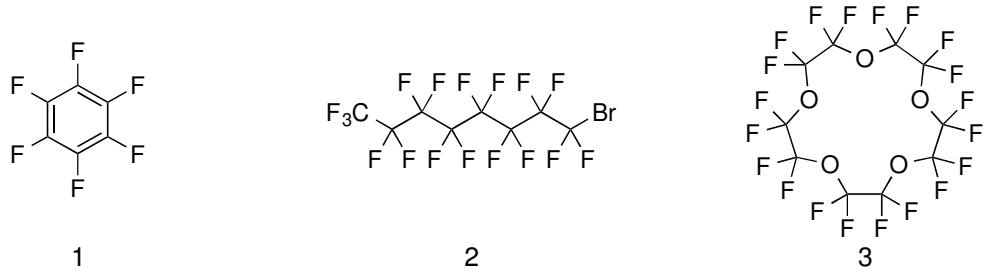

Figure 1-5: Examples of perfluorocarbons used as MRI contrast agents: 1) Perfluorobenzene, 2) Perfluoro-Octylbromide (PFOB), and 3) Perfluoro-15-crown-5.

With several exceptions, and while having an extremely low solubility in water or buffer, these compounds are biocompatible when used as an emulsion for intravenous injection.[40] Practical considerations however, in particular from multiple fluorine resonances due to inequivalent ^{19}F nuclei as in the case of agents such as PFOB, create complications in an MR experiment as their multiple resonances cause the appearance of fragments in MRI, which can clearly be seen in Figure 1-6, looking at the MRI phantom image for PFOB.

The MRI phantom image produced from multiple fluorine resonances is resolved to two images at different positions with only slight overlap, whereas perfluoro 15-crown-5 shows only one resonance and one image in the phantom image: Nonetheless, they both demonstrate low signal-to-noise (SNR) ratios.[41]

Perfluorobenzene has shown particular promise due to its single ^{19}F resonance, faster relaxation times than its non-aromatic counterparts, and lack of biological toxicity. However, its low molecular weight relative to other perfluorinated compounds results in high volatility, which alone prevents its safe use for human study.[42] Additionally, the high lipophilicity and membrane permeability of perfluorocarbons designed as MRI contrast agents present safety concerns in their toxicity due to extremely long clearance times, for example, up to 250 days for perfluoro-15-crown-5.[43]

Higuchi et al. reported in 2005 that amyloid-beta (Aβ) plaques, the hallmark of Alzheimer's disease pathology, could be detected by MRI using a molecule called FSB (or (*E*,*E*)-1-**f**luoro-2,5-bis(3-hydroxycarbonyl-4-hydroxy)**s**tyryl-**b**enzene).[33] The structure of FSB was based on the organic dye Congo Red and can penetrate the blood-brain barrier.

The authors cite their previous work where an analogous compound BSB (having a bromine in place of the fluorine in FSB) was found to label amyloid-beta plaques. They reasoned that FSB should label plaques as BSB does and allow for plaque detection by ^{19}F MRI. The greatest contrast was observed using a T_2-weighted gradient-echo experiment, and the authors concluded that cross-linking and protein interactions in the plaques are responsible for the decreased T_2 values observed. However, having a single fluorine atom per molecule of FSB, the sensitivity was also very low.

Compound	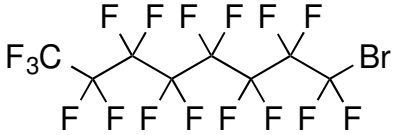	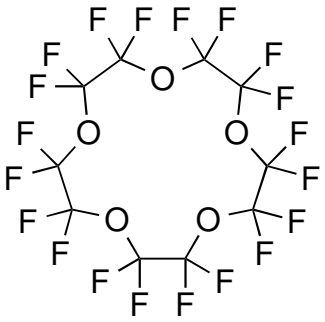
NMR Spectrum	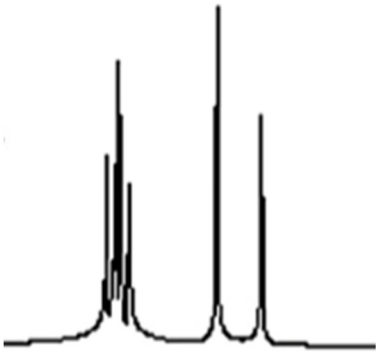	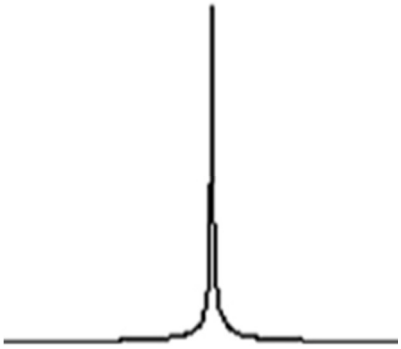
MRI Gradient Encoding	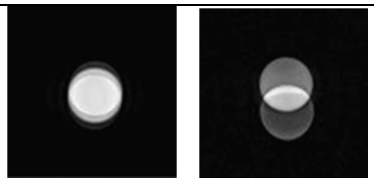	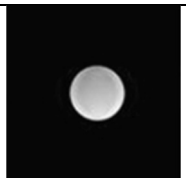

Figure 1-6: NMR Spectra and gradient-echo phantom images of perfluorooctylbromide (PFOB) and perfluoro-15-crown-5. Images reproduced from Srinivas et. al. and used with permission. Table design reproduced from Wolters et. al

Work by Flaherty [44]et al. consisted of adding more ^{19}F nuclei to the structure of FSB, in on example by saturating the benzene core, and in another example where trifluoromethyl groups were placed on the peripheral phenyl rings.[44] (Figure 1-7) The sensitivity was increased, and these compounds were found to be preferentially more specific for Aβ plaques than FSB, but a mechanism behind these observations wasn't

concluded. Furthermore, these three agents could not be used in high amounts to increase sensitivity, showing nephrotoxicity at 40 mg/kg.

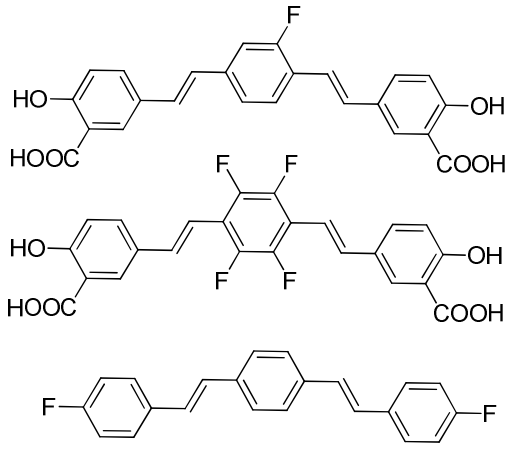

Figure 1-7: FSB, both Flaherty molecules (unnamed): Chemical structures of FSB, and their further derivatives as produced by Flaherty et al.

Perfluoro-15-crown-5 was examined in 2008 by Flogel et al. for imaging inflammation and ischemia, symptoms that are related to trauma and cardiac disorders, among others.[45] The compound was emulsified and injected intravenously to mice models and imaged by MRI. The compound was found to primarily locate areas with ischemia. This was done by taking a standard ^{1}H MRI scan to show where the trauma occurred, then comparing it to the ^{19}F MRI scan. It was found that the crown ether preferentially deposited in border regions between healthy tissue and inflamed or ischemic tissue. Repeat trials were done over several days and the distribution of ^{19}F MR signals seemed not to change. However, as noted before, the extremely long elimination time of perfluoro-15-crown-5 renders it unsafe for clinical use.

Hexafluorosulfane (SF_6), combined with other inert gases as an inhalant, has been shown to localize in the lungs and other airways and used partially to measure pO_2 or to visualize abnormalities.[46] This compound benefits from having a desirable safety profile with clearance times in hours rather than in days, and what's most

noteworthy about this compound is that it has an extremely short T_1 value of 5.9 ms. The short T_1 time is unique to this compound, and has been suggested that this is due to the sulfer-fluorine bond, which is one of the strongest single bonds ever measured. As the literature has presented, however, is that the different instrumentation is required to successfully image this compound, which is likely due to the unreported value of the concomitant shortening of T_2 along with the reduction in T_1.[47]

1.4.4 Limits to Degree of ^{19}F Labeling

One approach to increase the sensitivity of fluorine contrast agents is to incorporate as many chemically-equivalent ^{19}F nuclei as possible within the contrast agent. Perfluorinated compounds (PFC's; discussed in section 1.3.3) have very high degrees of fluorine labeling, but they also suffer from extremely low solubility in water or buffer due to the hydrophobic nature of fluorine. Low solubility in water also increases clearance times that raise their safety concerns.

The pharmacokinetics, especially clearance times, of a contrast agent should be part of its design. An ideal contrast agent would have both high ^{19}F labeling while retaining high water solubility.

1.4.5 How To Address These Issues

The design of a viable ^{19}F MRI contrast agent for biological use would be most efficient using chemically equivalent fluorine labeling. The extent of fluorine labeling should be as high as possible while maintaining high water solubility, and high water solubility should also result in clearance times of at most, 24 h.

1.4.6 Metal-Based ^{19}F MRI Contrast Agents

1.4.6.1 Use of Paramagnetic Metals

The incorporation of a paramagnetic metal center within the contrast agent, spaced within ca. 6.0-7.5 Å from the detected nuclei and the metal center can significantly decrease relaxation times, often by over two orders of magnitude.[32,48] This effect is known as paramagnetic relaxation enhancement (PRE), and allows for more scans to be taken per unit time, providing greater contrast in the MR image. Lanthanide(III) ions are commonly used, especially Gd(III) for imaging ^{1}H.

Without the use of a paramagnetic metal center, local concentrations of fluorinated compounds require up to and in excess of 100 mM in biological systems to obtain useful MR images.[34,49] Such high concentrations of fluorinated agents are difficult to achieve in vivo and also pose safety concerns even if they are chemically inert.

1.4.6.2 Design Considerations of Metal-Based ^{19}F Contrast Agents

The metal ions themselves are inherently toxic and require the use of ligands that form kinetically and thermodynamically stable complexes with the 9-coordinate Ln(III) ions. Concomitant with 1988's introduction of $[Gd\text{-}DTPA]^{2-}$ (Magnevist) there has been extensive study of different ligand systems to bind Ln(III) ions. Most are modifications of DTPA or of DOTA frameworks. In ^{1}H MRI, Gd(III) has proven to be superior to the other Ln(III)'s. However, the PRE of ^{19}F nuclei provided by Gd(III) often shortens their T_2 times to the extent where there is virtually no signal resolved in ^{19}F MRI/MRS.

Other Ln(III) metals must then be used to afford viable ^{19}F contrast agents. The clinical success and demonstrated safety profiles of Gd(III)-based contrast agents can be applied to other Ln(III) ions, as all are nine-coordinate and approximately the same size (although the ionic radius does become smaller through the series).

Nitrogenous macrocyclic frameworks, such as 1,4,7-triazonane (TACN), 1,4,7,10-tetraazacyclododecane (cyclen) or 1,4,8,11-tetraazacyclotetradecane (cyclam) are popular starting points in contrast agent design. The secondary amines are easily substituted with organic groups (informally known as pendant "arms"), completing the coordination environment for the metal, and imparting other functionalities such as ^{19}F labels.

Enhanced signal intensities in ^{19}F MRI/MRS can be obtained with high ^{19}F labeling provided that 1) each ^{19}F label is chemically equivalent for optimal sensitivity, and 2) the resultant complex remains highly soluble in water.

1.4.6.3 Sensitivity, Water Solubility, and Biocompatibility

The predominant issue in all classes of ^{19}F contrast agents is fluorine's low sensitivity in MRI. This is due to their extremely long T_1 times. The recycle delay period (**d1**) of ^{19}F nuclei can range from 2.2-5 seconds between scans in order to allow full relaxation decay before the next scan begins. Gradient-echo imaging benefits from scan repetition prior to full relaxation,[50] and other techniques including turbo gradient-echo (TGE),[51] gradient-echo and spin-echo (GRASE),[52] and sweep imaging with Fourier transform (SWIFT)[53,54] can all be used and can help increase the SNR of contrast agents, but offer only modest improvements in sensitivity.

The greater impact on ^{19}F sensitivity is obtained by decreasing relaxation times of ^{19}F nuclei which is best accomplished by incorporating a paramagnetic metal center within the contrast agent. Different metals can reduce relaxation times to various extents, and also can reduce T_1 and T_2 by different ratios. Since the repetition time between MRI scans is limited by T_1, metals that provide the shortest T_1 values are desired. However, concomitant with a reduced T_1 value is also a reduced T_2 value, which can result in line broadening and decreased SNR's. Therefore metals providing T_2/T_1 ratios closest to 1 are actually the most effective for increasing sensitivity.

Additional parameters such as tumbling rate (τ_R) in solution, the distance between the paramagnetic center and the ^{19}F nuclei (d), and field strength of the MRI instrument also affect the sensitivity. These parameters will be discussed in further detail in Chapter 2.

Another critical limitation in ^{19}F MRI is fluorine's hydrophobicity. A viable MRI contrast agent must be soluble in water and at appreciable concentrations, but a molecule's water solubility decreases as more and more ^{19}F nuclei are installed on the molecule. But as discussed in 1.4.4 and 1.5.2, fluorine's low sensitivity issue benefits from high fluorine labeling, presenting the need of balancing ligand design to maximize the fluorine loading while retaining sufficient water solubility.

Sensitivity is also dependent on local concentrations *in vivo*. The administration therefore of as high doses as possible of a ^{19}F contrast agent produces the greatest contrast. However, use of high concentrations of a metal-based ^{19}F contrast agent, even when the metal is chelated with the strongest of ligands (e.g.

DTPA and DOTA derivatives), raises the same risks for patients with kidney impairment or NSF as do Gd(III) agents.

One way to address this problem of course would be reducing the amount of contrast agent used, but since improving sensitivity is critical for ^{19}F contrast agents, lower doses are not an ideal solution. Instead, another solution is concerned with ensuring that the *in vivo* clearance of the contrast agent occurs quickly enough so that appreciable amounts of transmetallation do not occur. Thus, while ^{19}F-based contrast agents might require high dosage, the potential safety risks can be reduced if the contrast agent is rapidly cleared from the biological system.

1.5 Responsive or "Smart" Contrast Agents

Contrast agents can also be designed to produce a change in the MR image in response to their interaction(s) with biomarkers. These contrast agents are known as responsive or "smart" probes, which are unrelated to targeted probes such as MS-325 (Vasovist) or Eovist, which have a predictable biodistribution but do not have a response mechanism.

1.5.1 The Importance of a Ratiometric Response

All of the above examples also suffer from an inability to quantitatively measure any desired target. Stated another way, they are not ratiometric. In 2009 Gianolio *et al.* reported a ^{19}F-based probe that responds to pH with changes observable both in the ^{1}H and ^{19}F MR images.[55] The signal that directly indicates pH levels of the local environment responds to manipulation of a sulfonamide group, changing the relaxation times of ^{1}H nuclei, where other contrast agents usually lack a ratiometric response due mostly to overlap of the resonances that are observed between unreacted

and reacted states. A single MR image cannot be used to determine the exact concentration of the contrast agent, this probe can be independently imaged by ^{1}H MRI as well as ^{19}F MRI as it contains ^{19}F reporter nuclei that do not undergo this change in relaxation rates upon response to the analyte while the ^{1}H nuclei that are imaged do. Thus, combing the results from the ^{1}H image and the ^{19}F image allows for a ratiometric response. However, while tuning a standard ^{1}H MRI device to ^{19}F is a reasonable endeavor for longer-term studies, it is not reasonable to continuously re-tune an MR device back and forth between ^{1}H and ^{19}F in order to assemble a diagnostic scan, so for clinical use, unless two separate magnets are available, this probe's ratiometric response cannot be used easily since both a ^{1}H and ^{19}F experiment must be conducted within a short period of time, which is much shorter than the time required for ^{1}H and ^{19}F tuning of a single MR instrument.

A solution then for designing a ratiometric probe for MRI purposes would require that two or more independent signals from the same nuclei, be imaged in one combined procedure. Current Gd(III) agents image water protons, as is the case with other traditional MRI contrast agents. One of the most important advantages then of ^{19}F MRI involves its ability to differentiate between two signals, both provided by a single ^{19}F MRI contrast agent.

Responsive MRI contrast agents contain functional groups that, in presence of a particular biomarker, alter the MR and/or chemical properties of the probe. This produces a change in the observed contrast between the probe in absence of the biomarker and the probe in presence of the biomarker, which can be resolved by MRI/MRS. The chemical groups used to target specific biomarkers commonly are not

selective for a single biomarker alone, leading to false positives in the MR image. Ideal contrast agents are therefore those that are selective for a single analyte.

When a contrast agent is in the presence of its targeted biomarker, there must be a change in the MR properties of the probe that is significant enough to be resolved by MRI/MRS. Multiple response mechanisms can be detected by MRI/MRS, depending on the nature of the responsive contrast agent.

1.5.2 Responsive Gd(III)-Based Contrast Agents

Responsive Gd(III)-based contrast agents are limited to a single mechanism—change in the hydration number (q) of the Gd(III) center.[7,56] As q is increased, more water molecules can interact with the inner sphere of the metal center, enhancing relaxivity, and brighten the MR image.

Several issues are encountered with this response mechanism. By increasing the q value, the Gd(III) center can also interact with endogenous anions such carbonate and phosphate.[57,58] These interactions negate the enhanced relaxivity to various degrees, producing a nebulous response. Increasing q also increases the lability of the Gd(III) ion, resulting in greater safety concerns. Finally, it is impossible to determine whether any contrast enhancement observed by MRI is a result of either higher concentrations of the biomarker, higher concentrations of the contrast agent, or a combination of both, since accurate quantification of these contrast agents has remained elusive.

1.5.3 Responsive MION-Based Contrast Agents

Responsive contrast agents based on MION's function through the formation of aggregates in response to a biomarker. These aggregated states alter the observed

relaxation times—most often with an increase in T_1 and decrease in T_2—which can be resolved by MRI/MRS.[14] Unlike Gd(III)-based agents, these systems are not affected by endogenous ions, but still suffer from several issues limiting their practical use. Their response by MRI is observed as darkening which is more difficult to detect, the observed change in relaxation times is less than two-fold limiting their practicality, and they exhibit a non-linear response to different concentrations of analyte.[59]

It has been reported that the aggregate size of MION's must be limited to approximately 200 nm, and as aggregation occurs, the T_2 times increase as the aggregate grows in size. What this means is that the contrast effect of the agent changes gradually as the aggregates become larger and larger, producing a grayscale image much like what a Gd(III) agent would create. Likewise, differences in chemical environments also affect the relaxation times, which can be analyzed and processed in order to form an image.

More importantly, these agents have demonstrated that their response to an analyte can occur from two different states of aggregation, following the bell-shaped curve in Figure 1-8[59] which is the report of a MION-based contrast agent used for the detection of Cu(I).

As seen in Figure 1-8 the green trace enhances r_2 to a point with increasing concentrations of Cu(I), but then r_2 decreases following that point. Also, the blue trace with the highest amount of Cu(I) follows no pattern relating to the other three traces or the control. This results in that the recorded relaxation times might not correlate to one single value of analyte concentration, in this case Cu(I), leading to an ambiguous response.

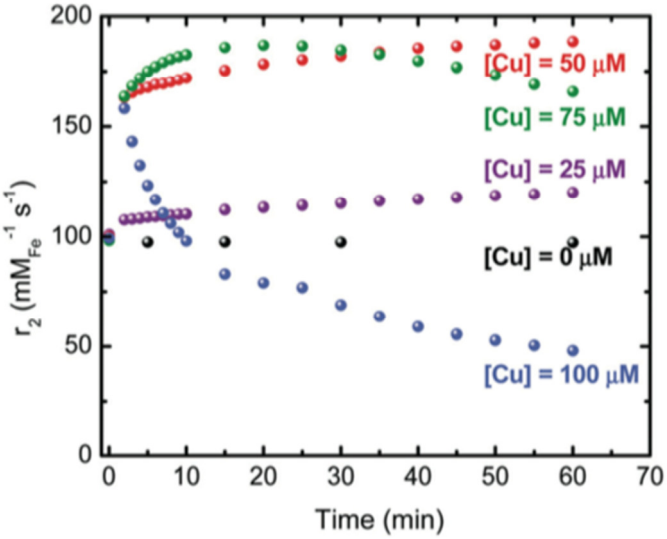

Figure 1-8: The responsive MION agent, selective for Cu(I), shows in green a non-linear response, while the 100 μM trace in blue doesn't follow any pattern related to the other four traces. Reproduced from Smolensky et al. (Dalton Trans., 2012, 41, 8039).

Furthermore, their response is dependent on aggregation, and does not change linearly.[59] Some MION systems are ratiometric while others are not—which is a property necessary to quantify (as opposed to strictly visualize differences in) analyte concentrations in target tissue by MRI.[59] While MION-based contrast agents have proven to be safer than other contrast agents, these factors represent strict limitations within the scope of MION-based contrast agents for clinical use.

1.5.4 Responsive ^{19}F-Based Contrast Agents

The response mechanisms available for imaging fluorine-based contrast agents are unrelated to those of Gd(III)- and MION-based responsive contrast agents, a result provided by using fluorine as the detected nuclei rather than endogenous water protons. Three independent mechanisms can be used to detect the response of ^{19}F-

based probes: changes in the chemical shift of the ^{19}F signal, changes in the relaxation rates of ^{19}F nuclei, and changes in the signal intensity observed by MRI/MRS.

1.5.4.1 Change in Chemical Shift

Known as the lanthanide-induced shift (LIS), but also can be applied to other paramagnetic metals such as Fe(II) (which is explored in this work) is dictated by the McConnel-Robertson equation, which predicts that the magnitude of the LIS carries an d^3 dependence, where d is the distance from the nuclei being imaged and the paramagnetic center. The response mechanism of a fluorine probe should then result in a conformational change of the molecule that changes the distance between the paramagnetic center and the ^{19}F nuclei.

The change in chemical shift ($\Delta\delta$) when applied to MRI (as long as the chemical shift change is of an appreciable value, ca. 8-10 ppm or greater) provides that one MR image at a particular chemical shift could detect the probe in absence of a biomarker while a second image at a different chemical shift could detect the probe in presence of the biomarker. Either image alone can be used directly to detect either the appearance or disappearance of the original or the shifted resonance, creating an "on/off" type of probe.

1.5.4.2 Change in Relaxation Times

A second response mechanism for ^{19}F-based probes that can be imaged by MRI is a change in the relaxation times of the ^{19}F-nuclei on the contrast agent. This response mechanism also is generated by a conformational change in the contrast agent in response to an analyte. According to Bloch-Redfield-Wangsness (BRW) theory, the enhancements in relaxation rates, in a similar fashion to the McConnel-

Robertson equation (d^3 dependency), carry an d^6 dependency, where d again is the distance between the ^{19}F nuclei and the paramagnetic center. A change in d produces a change in the relaxation times.

1.5.4.3 Change in Signal Intensity

A third response mechanism is reliant only on the intensity of the observed signal, which is provided as the T_2 relaxation time is changed. Changes in T_2 result in either increased or decreased line broadening. This immediately presents a possible complication in that the observed signal intensity of any ^{19}F contrast agent is also determined by its local concentration, which remains an issue for Gd(III)-based agents which have a single ^{1}H chemical shift. Fluorine-based contrast agents however can be designed with different fluorine labels with different chemical shifts, and can be independently imaged by MRI/MRS.

If a ^{19}F-based contrast agent's response mechanism results in a change of signal intensity, the local concentration must be determined as well. Installing an additional fluorine label that does not respond to the presence of the biomarker, and having a different chemical shift from the reporter ^{19}F nuclei, can allow separate imaging separately to determine local concentrations of the contrast agent. Incorporating such a fluorine label would likely be challenging, and may also reduce water solubility.

Another approach to determine local concentrations would be to image a prominent ^{1}H resonance on the probe. This approach might be difficult as well, since conformational changes in the contrast agent would likely affect most if not all ^{1}H nuclei in a similar fashion as ^{19}F nuclei are affected.

The possible complications with resolving these issues in a contrast agent, whose response mechanism results in a change in the signal intensity, are the most difficult to address when compared to the other two response mechanisms described.

1.5.5 Current Responsive Metal-Based ^{19}F MRI Contrast Agents

Despite fluorine's low sensitivity, there are many reports of fluorinated chemical probes that have been resolved by MRI/MRS, using all three response mechanisms (a change in chemical shift, a change in relaxation times, and/or a change in signal intensity).

An example Figure 1-9 of a chemical shift-changing ^{19}F probe was reported by Deutsch et al. in 1989.[60] A number of fluorinated anilines were synthesized and chemical shift changes as a function of pH were recorded. Different substitution patterns of ^{19}F nuclei on the aromatic ring changed the pKa values of the anilines, and their transition from protonated and deprotonated states resulted in chemical shift changes of 5-12 ppm, and the fluoroanilines reported showed responses from pH = 2 to pH = 8. These results were confirmed by MR imaging of rats in vivo by Vervoort *et al.*[61]

Changes in either the T_1 and/or the T_2 relaxation times of the ^{19}F nuclei can also be used for imaging. In 2008, Mizukami *et al.* reported real-time *in vitro* imaging with a Gd(III) complex was used to monitor enzymatic activity using the cleavage of a portion of the fluorinated molecule by caspace-3.[62]

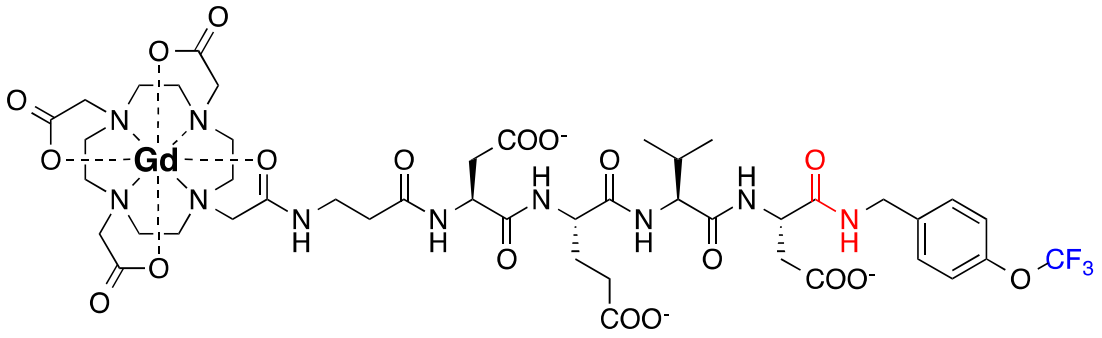

Figure 1-9: Mizukami Peptide Gd OCF_3 Complex: In this image of Mizukami's gadolinium probe, the metal is complexed with a DO3A ligand, connected to a short peptide, and terminating with a para-trifluoromethyl group. The fluorine reporter group is highlighted in blue while the amide bond that is cleaved by the enzyme is highlighted in red.

The molecule Figure 1-9 contains a ligated Gd(III) center, a peptide linker that also serves as the substrate for the enzyme, and a *para*-trifluoromethoxy reporter group. The activity of the enzyme cleaves the reporter group and the relaxation times are then increased. However, the change in the relaxation times were trivial, and while the proof-of-concept study was successful, this system would not be feasible for in vivo use due to nebulous responses and merging of the resonances prior to and after the enzymatic cleavage of the CF_3 reporting group. Additionally, the sensitivity is very low, meaning a system such as this would not provide the required contrast for a clinical MRI procedure *in vivo* demonstrating the same response characteristics.

An example of a probe imaged by change in signal intensity was reported by Takaoka *et al.* in 2011.[63] A series of ^{19}F-labeled compounds were attached to several protein substrates. These molecules would self-assembled in to aggregates, where little to no signal was observed from the aggregates alone (despite high ^{19}F labeling) due to decreased T_2 values of the ^{19}F nuclei. When exposed to the target proteins, the aggregates disassemble back to their monomeric states and T_2 times are restored, and the ^{19}F signal can be seen by MRS. The greatest signal enhancement was observed

using biotin and methotrexate as substrates. They concluded that this system is an "on/off" system, in that in absence of protein no signal is observed, while the addition of the protein resulted in a strong signal observed by MRS.

1.6 Proposed ^{19}F Metal-Based Complexes and Project Aims

The primary goal of the work carried out and described in this thesis is to synthesize and analyze responsive ^{19}F metal-based contrast agents that improve upon currently reported probes in their performance by MRI/MRS, and to provide important information of their in vivo biocompatibility, biodistribution, clearance times, and their pharmacokinetics. This study requires the synthesis and analysis of prototypical ^{19}F contrast agents, their behavior in response to different paramagnetic metals used, ^{19}F MRI imaging, compatibility in blood, optimization of ligand field environment, in vivo studies to determine biocompatibility, and finally to synthesize a ratiometric and responsive ^{19}F contrast agent that provides sufficient sensitivity to be resolved in MRI imaging procedures of 30 minutes or less.

The results of each of these specific aims will be discussed in detail in the following chapters.

2 Design of Metal-Based ^{19}F MRI Contrast Agents—Optimizing Magnetic Resonance Properties

2.1 Introduction

As discussed in Chapter 1, a clinically viable ^{19}F contrast agent requires hi-gh sensitivity and biocompatibility. Sensitivity can be increased by increasing the number

of chemically equivalent fluorine nuclei in a contrast agent and by reducing their relaxation times. The biocompatibility of such probes can benefit from high water solubility, low toxicity, and rapid clearance of the contrast agent. These properties can be evaluated and adjusted in the design of a contrast agent for optimal performance in MRI. The most appropriate design for a safe and clinically viable ^{19}F contrast agent would consist of a strongly chelated, paramagnetic metal center with a high degree of equivalent ^{19}F nuclei and high water solubility. Chapter 1 briefly described how certain structural properties can be manipulated in a probe's design both to optimize sensitivity and to establish desirable pharmacokinetics.

The focal point of this chapter will be optimizing sensitivity. Many of the MR properties of paramagnetic ^{19}F contrast agents (T_1, T_2, ^{19}FLIS) can be derived theoretically and measured experimentally. This chapter will discuss development and analysis of MR theory applied to the prototypical ligand DOTAm-F12 and its corresponding metal complexes. The work reported in this chapter was carried out first in order to optimize the sensitivity of ^{19}F-based MRI contrast agents.

2.2 ^{19}F Signal Intensity

The signal intensity for spin-echo MRI is dependent on the number of nuclei in the volume being imaged and their longitudinal and transverse relaxation times (T_1 and T_2) according to the following equation:[64,65]

$$I \approx N(F) \exp\left(\frac{T_E}{T_2}\right)\left[1 - 2\exp\left(\frac{-\left(T_R - \frac{T_E}{2}\right)}{T_1}\right) + \exp\left(\frac{-T_E}{T_1}\right)\right] \qquad (2\text{-}1)$$

where I is the intensity of the image, $N(F)$ is the ^{19}F nuclei density detectable by NMR, and T_R and T_E are the repetition time and echo times of the pulse sequence,

respectively. Image intensity can be augmented by incorporating additional chemically equivalent ^{19}F nuclei and by increasing ^{19}F relaxation rates. Linear polymers,[66-69] dendrimers,[70-74] hyperbranched or star polymers,[64,75-77] and nanoparticle-based[78-80] probes have been reported that maximize local ^{19}F spin density and facilitate reduced fluorine relaxation times *via* the slow molecular tumbling of the structures. However, when relaxation is modulated by decreasing the rotational correlation time (τ_R), the concomitant decrease in T_2 negatively affects signal intensity. Optimizing signal intensity, thus, requires decreasing T_1 as much as possible while minimizing the effect on T_2 so as to achieve a T_2/T_1 value near one. Paramagnetic metals are well known to decrease relaxation times of nearby nucleus by up to two orders of magnitude, with the relative decrease in T_2 *versus* T_1 being influenced by the nature of the metal and its complex.[31,81,82] We postulated that this approach, with careful consideration of the complexes' structure, can afford highly water soluble fluorine contrast agents; which can, in principle, further be exploited in the design of responsive imaging agents.

2.3 Limitations of Reported ^{19}F Responsive Probes

Recent progress in the field of molecular paramagnetic ^{19}F imaging agents has hinted at the possibility of exploiting this approach for biological imaging. A Dy^{III} triphosphonate complex with a trifluroaryl substituted amide arm ([Dy-DOPA-arCF_3]) is soluble in water and increases SNR 13-fold compared to diamagnetic analogs.[83] Unfortunately, efforts to increase the number of ^{19}F nuclei *via* tetra-substitution of the chelate with the trifluoroaryl moiety provided complexes with insufficient water

solubility for biological MRI.[82] Despite the C_4 symmetry of *tetra*-trifluoroethyl substituted Ln-DOTMP complexes ([Ln-F-DOTPME]$^-$), the fluorine signal intensity was reduced due the existence of multi stereoisomers in solution.[84] Stereoisomers arising from different configurations of the macrocyclic ring or arrangement of the pendant arms have also been observed with other fluorinated DOTA- or DOPA-based metal complexes designed for ^{19}F MRI.[85,86] For MRI applications, complexes that exist as multiple isomers in solution diminish the overall signal intensity at the imaging frequency and negatively affect the observed SNR. It is apparent from these studies that the symmetry of the complex as well as the rate of interconversion between isomers are important considerations in the design of paramagnetic fluorine probes.

2.4 DOTAm-F12 Metal Complexes

Here, the synthesis and physical characterization of a water-soluble, paramagnetic ^{19}F MRI contrast agent featuring a highly fluorinated chelate is presented. The structures of the ligand and its metal complexes are shown in Figure 2-1.

Additionally, the potential of these imaging agents for use in ^{19}F MRI is evaluated in water and rat blood. The ligand, DOTAm-F12 (**2-1**), consists of a 2,2,2-trifluoroethyl acetamide substituted macrocycle that features twelve chemically equivalent fluorine nuclei The corresponding M-DOTAm-F12 complexes containing La(III), Eu(III), Gd(III), Tb(III), Dy(III), Ho(III), Er(III), Tm(III), Yb(III), and Fe(II) are highly water-soluble and produce one fluorine resonance peak.

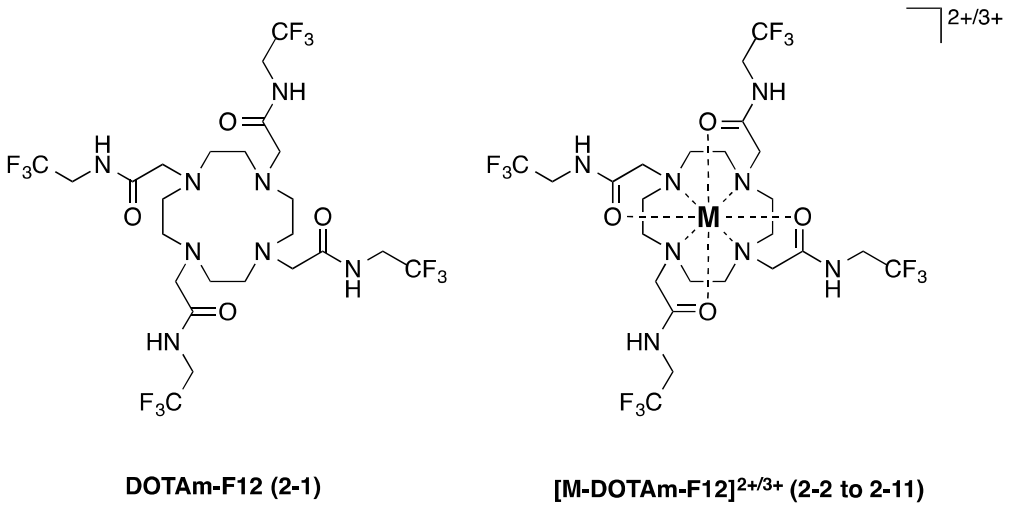

Figure 2-1: Chemical structures of DOTAm-F12 (2-1) and [M-DOTAm-F12]$^{2+/3+}$ complexes. M = La (III) (2-2), Eu (III) (2-3), Gd (III) (2-4), Tb (III) (2-5), Dy (III) (2-6), Ho (III) (2-7), Er (III) (2-8), Tm (II)I (2-9), Yb (III) (2-10), and Fe (II) (2-11).

Although prior studies on paramagnetic fluorine probes have focused entirely on lanthanide ions,[31,81,82] it was postulated that the high-spin, paramagnetic Fe(II) and its high magnetic moment, could also yield sensitive fluorine probes with a short T_1 time and high T_2/T_1 ratio.

The ligand DOTAm-F12 was synthesized in two steps and readily forms lanthanide complexes from their respective halide salts as shown in Scheme 2-1 In a first step, 2,2,2-trifluoroethylamine is coupled to bromoacetyl bromide in mixture of CH_2Cl_2 and aqueous K_2CO_3 to form the pendant arm 2. This arm is then coupled to the cyclen backbone under standard conditions yielding the ligand DOTAm-F12 in high yield. The synthesis of this ligand can be readily scaled up to 10 g. The lanthanide complexes Ln-DOTAm-F12 are generated from equimolar amounts of the ligand and the respective lanthanide halide salt in aqueous solution at neutral pH after 3 days at 75°C.

2.4.1 Synthesis of DOTAm-F12 Metal Complexes

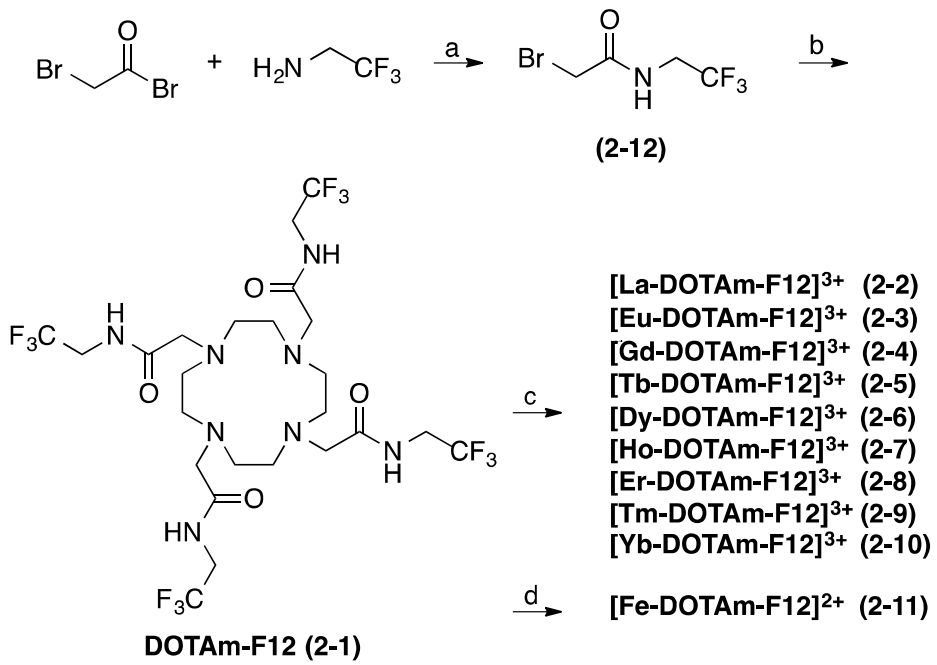

Scheme 2-1 Synthesis of DOTAm-F12: aReagents and conditions: (a) K_2CO_3, H_2O/CH_2Cl_2, 1 h, 80.7%; (b) cyclen, K_2CO_3, CH_3CN, reflux, 8 h, 85.9%; (c) LnX_3, NaOH, $CH_3CN/CH_3OH/H_2O$, 75°C, 77-104 h, 98.0%-99.9%; (d) $Fe(OSO_2CF_3)_2$, CH_3CN/CH_3OH, 70°C, 30 h, quant.

The Fe(II) complex was formed under argon from irron(II)trifluoromethanesulfonate according to a procedure reported by Morrow.[87] Notably, all the complexes demonstrate high water solubility (>100 mM) despite their high fluorine content (> 25% by mass).

2.4.2 Using Fe(II) as the Paramagnetic Metal

Iron-based fluorine contrast agents have not yet been evaluated as MRI contrast agents. However, the properties of Fe(II) complex previously studied as paramagnetic chemical exchange saturation transfer (PARACEST) MRI agents[87-89] and reported NMR studies of fluorinated iron complexes[90-93] encouraged us to also evaluate Fe(II)-DOTAm-F12. In addition, iron complexes are anticipated to be less toxic to patients suffering from chronic and acute renal insufficiencies due to intrinsic

iron homeostatic mechanisms and iron-bind proteins, such as transferrin, that can regulate the concentration of iron in the blood. Work by Morrow has illustrated that Fe^{II} macrocyclic complexes are air stable for days and inert to Fe dissociation,[87,89] supporting the use of such complexes for *in vivo* MRI applications.

2.4.3 Characterization of $[M\text{-}DOTAm\text{-}F12]^{2+/3+}$ Complexes and Resultant MR Properties

The structures of the M-DOTAm-F12 complexes were evaluated by ^{1}H and ^{19}F NMR; the Tm complex was further investigated by X-ray crystallography and by DFT calculations.

The ^{1}H NMR spectra of each but two complexes demonstrated paramagnetic behavior with highly shifted resonances and reduced relaxation rates relative to the ligand alone. The ^{1}H spectrum of the diamagnetic La(III) complex lacked any shifted resonances, and the spectrum of the Gd(III) complex displayed no detectable resonances from the compound. Gd(III) complexes are known to behave this way due to their extremely short T_2 values leading to line broadening. Finally, the ^{1}H spectrum of the Fe(II) complex reveals significantly shifted resonances that verify the presence of a paramagnetic, high-spin Fe (Figure 2-2). This is in agreement with the literature, which reports stabilization of the +2 oxidation state of iron by amide pendant groups.[94]

By ^{19}F NMR, each complex displays a single resonance as shown in Figure 2-3. The sharper, secondary feature in the Gd(III) spectrum (δ_F = -72.9 ppm) is from the presence of uncomplexed ligand, and the signal at δ_F = -79.4 ppm in the Fe(II) spectrum is from the triflate counterion. Lanthanide complexes formed from DOTA-tetraamide ligands are known to adopt a C_4-symmetric geometry when each amide

pendant arm is the same. The Fe (II) complex also displays a single ^{19}F resonance at δ_F = -70.9 ppm, indicating a C_4 symmetric complex. Morrow also observed C_4 symmetry and one diastereomeric form of Fe(II)-DOTA-tetraamide complexes by ^1H NMR, which suggests coordination of all four of the carbonyls.[87,88] Compared to the lanthanide complexes (with the exception of Eu, Gd, and La), Fe(II)-DOTAm-F12 yields a smaller ^{19}F paramagnetic-induced pseudocontact shift (+2.0 ppm). Unfortunately, detailed crystallographic structural analysis of Fe(II)-DOTAm complexes is not yet represented in the literature.[88]

They demonstrate paramagnetic character with each complex except the diamagnetic La(III) control (Figure 2-2). Importantly, ^{19}F NMR of each complex in D_2O revealed one single fluorine resonance (Figure 2-2).

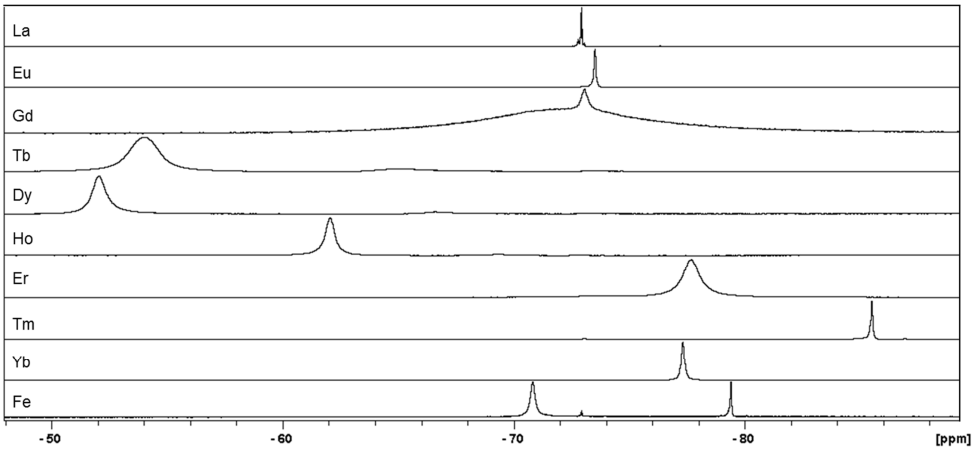

Figure 2-2: ^{19}F NMR of M-DOTAm-F12 complexes (282 MHz, D_2O). Note that in the spectra of FeII-DOTAm-F12 the peak at δ_F = -79.4 ppm corresponds to the trifluoromethanesulfonate counter ion.

The presence of a single peak illustrates that any rotation of the trifluoromethyl arm occurs faster than the NMR time scale. This represents a major advantage over the isomeric mixtures of other ^{19}F contrast agents, such as $[Ln\text{-}F\text{-}DOTPME]^-$ [31,84] and

DOTA-based complexes with aryl trifluoromethyl groups, [81,82,86] which were characterized by up to twelve ^{19}F peaks at different relative intensities.

Indeed, fluorine probes with unequivalent ^{19}F nuclei that have small frequency differences between the ^{19}F resonances can overlap in an MR scan, resulting in poorly resolved images.

2.4.4 Lanthanide-Induced Shift and Bleaney Theory

The NMR spectra give further information with regard to the solution structures of the complexes. In the case of lanthanide ions, the shift in a nuclei's resonance caused by the paramagnetic metal is defined as the lanthanide-induced shift. The lanthanide-induced shift of the fluorine nuclei, ^{19}FLIS, can be defined as $\Delta\delta_F = \delta_{F\ paramagnetic} - \delta_{F\ diamagnetic}$. Since the ^{19}F – M distances (d) in our complexes are greater than 5 Å, the contact shift, δ_c, is assumed to be negligible and the observed LIS results from the pseudocontact component, δ_{pc}. Under these conditions, the ^{19}FLIS is described by the McConnell-Robertson equation (Equation 2):[31]

$$^{19}\text{FLIS} = C_D \frac{\beta^2}{60(kT)^2} \frac{(3\cos^2\theta - 1)}{d^3} B_2^0 \qquad (2\text{-}2)$$

where, d is the ^{19}F – Ln(III) distance, θ is the angle between the principal magnetic dipolar axis of the Ln(III) ion and ^{19}F nuclei, B_2^0 is the second order crystal field coefficient that is dependent on Ln(III) coordination environment, and C_D is the Bleaney constant for the specific lanthanide. Both the direction and magnitude of the shift are dependent on the identity of the lanthanide ion, allowing lanthanides to be ranked by their relative pseudocontact shift (PCS) strength according to their Bleaney constants .[31]

For every lanthanide complex of DOTAm-F12, the direction of the shift matches the sign of the Bleaney constant: Tb(III), Dy(III), and Ho(III) have a negative C_D and the ^{19}F resonance is shifted downfield, while the coefficients for Eu(III), Er(III), Tm(III), and Yb(III) are positive and their resonances are shifted upfield (Table 2-1). This provides insights to the location of the fluorine atoms around the metal center, and thus the solution structures of the lanthanide complexes. ^{19}F nuclei positioned equatorially, within a cone aligned with the principle magnetic axis, would shift downfield if the Bleaney coefficient is negative and upfield if it is positive.

Table 2-1: **^{19}F Chemical shift (δ), lanthanide induced shift (LIS, ΔδF), T_1 and T_2 relaxation times and MRI SNR of M-DOTAm-F12 complexes in water.**

	μ_{eff}/μ_B [a]	Bleaney Constant [c]	δ (ppm)	$\Delta\delta_F$	T_1 [d] (ms)	T_2 [d] (ms)	T_2/T_1 [d]	SNR [f, g]
DOTAm-F12 [e]	-	-	-72.9	0	880	680	0.77	n.d.
La-DOTAm-F12	-	-	-72.9	n/a	570	400	0.70	5.2
Eu-DOTAm-F12	3.40-3.51	4.0	-73.5	-0.6	360	41	0.11	7.8
Gd-DOTAm-F12	7.94	0	-72.9	0	12	<0.1	n/d	~1
Tb-DOTAm-F12	9.7	-87	-54.0	+18.9	6.3	1.3	0.21	31
Dy-DOTAm-F12	10.6	-100	-52.2	+20.7	5.9	2.2	0.37	6.0
Ho-DOTAm-F12	10.6	-39	-62.0	+10.9	7.6	5.4	0.71	31
Er-DOTAm-F12	9.6	32	-77.5	-4.6	14	8.8	0.63	13
Tm-DOTAm-F12	7.6	53	-85.6	-12.7	26	16	0.61	18
Yb-DOTAm-F12	4.5	22	-77.3	-4.4	130	55	0.42	20
Fe^{II}-DOTAm-F12	~ 5.2 [b]	-	-70.9	+2.0	5.7	5.6	0.98	40

Conditions: [a]Ref.[31] [b]μ_{eff} for Fe^{II}-DOTAm complex of 1,4,7,10-Tetrakis(carbamoylmethyl)-1,4,7,10-tetraazacyclododecane from Ref.[88] [c]Ref.[31,95] [d]B_0: 7.0 T, T = 20°C, D_2O. [e]NMR in deuterated methanol. [f]M-DOTAm-F12 = 5 mM, B_0: 9.4 T, T = 33°C, T_R = 5 ms. [g]SNR were obtained at the optimum chemical shift for each complex using images shown in Figure 2-10: La, -78 ppm; Eu, -78 ppm; Gd, -73 ppm; Tb, -73 ppm; Dy, -62; Ho, -62; Er, -78 ppm; Tm, -86 ppm; Yb, -86 ppm; Fe, -78 ppm.

Conversely, axially positioned nuclei, that are perpendicular to the principle magnetic axis, would be shifted in the opposite direction. Indeed, opposing directions of ^{19}FLIS are observed by Kim *et al.* for axial and equatorial positioned ^{19}F nuclei.[84] The fact that the ^{19}FLIS observed matches the sign of the Bleaney constant indicates (1) that all of the lanthanide complexes share a common structure in solution, and (2) that in each case the ^{19}F nuclei are located equatorially to the principle magnetic axis. It can thus be inferred that the fluorines do not aggregate as a hydrophobic cap on top of the macrocycle, but rather remain independently solvated on the equator of the complex

2.4.5 Determination of Coordinated Water Molecules (*q*)

This conclusion is further backed by ^{17}O NMR of the Dy(III) complex. According to the method of Peters,[96] evaluation of the chemical shift of the ^{1}H resonance of water in aqueous solution of Dy-DOTAm-F12 verified the presence of one inner sphere water molecule, *q*, on the Dy(III) complex, as shown in Figure 2-3 This agrees with previous reports of one bound water molecule in DOTA-tetramide complexes containing pendant amine, *N*-methyl, *N*-dimethyl, and *N*-aryl substituted arms.[82,97,98] Occupation of the ninth coordination site of Dy-DOTAm-F12 with a water molecule is also consistent with the outward positioned pendant arms that place the fluorines equatorially and provide solvent access to the lanthanide metal.

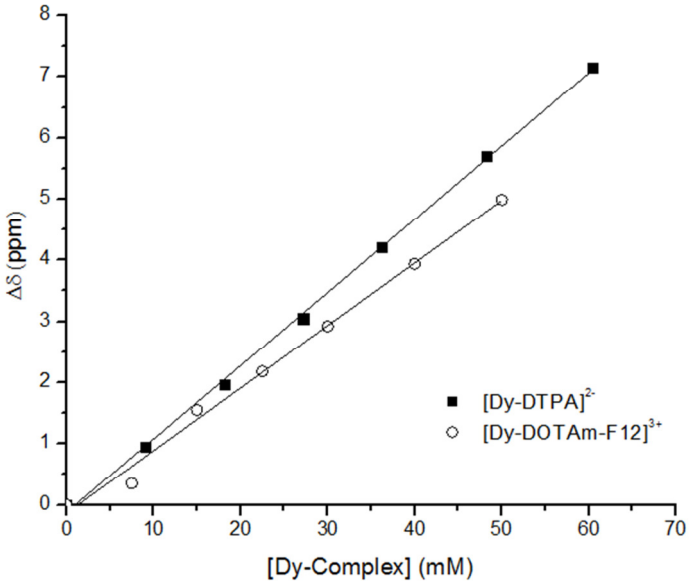

.

Figure 2-3: Chemical shift of ^{17}O of H_2O as a function of dysprosium complex concentration for $[Dy\text{-}DTPA]_2$- (filled square) and $[Dy\text{-}DOTAm\text{-}F12]^{3+}$ (open circle). The hydration number, *q*, for [Dy-DOTAm-F12]3+ was determined from the ratio of the slopes assuming $q = 1$

2.4.6 X-Ray Crystallography

The structure of Tm-DOTAm-F12 was also investigated by X-ray crystallography. In the crystalline state, Tm-DOTAm-F12 adopts a slightly distorted square-antiprismatic (SAP) geometry[99,100] consistent with an observed interplanar angle between the oxygen and nitrogen planes of 41.6˚, shown Figure 2-4, in Figure 2-5.

Based on the average N-C-C-N and N-C-C-O torsion angles of 54.1˚ and -23.4˚, respectively, the absolute configuration of the macrocycle is (δδδδ) in the crystal, while the pendant arms exhibit left-handed (Λ) helicity, which can be seen in Figure 2-6. The related $[Dy\text{-}DTMA]^{3+}$ with pendant *N*-methyl amide arms is also

SAP, but exists in the diastereomeric form with a left-handed (λλλλ) ring conformation and right-handed (Δ) helicity in the pendant arms.[97]

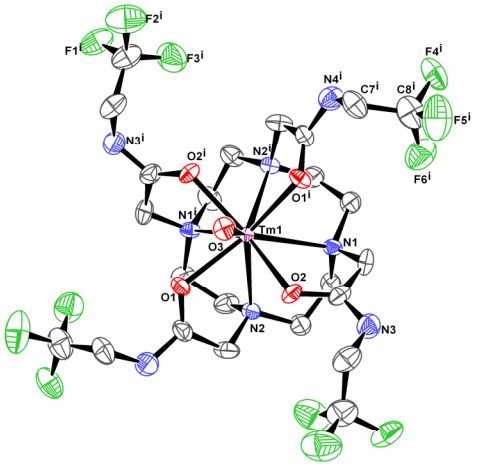

Figure 2-4: X-ray crystal structure of Tm-DOTAm-F12, side view (ORTEP, 50% probability level). Hydrogen and chlorine atoms omitted for clarity

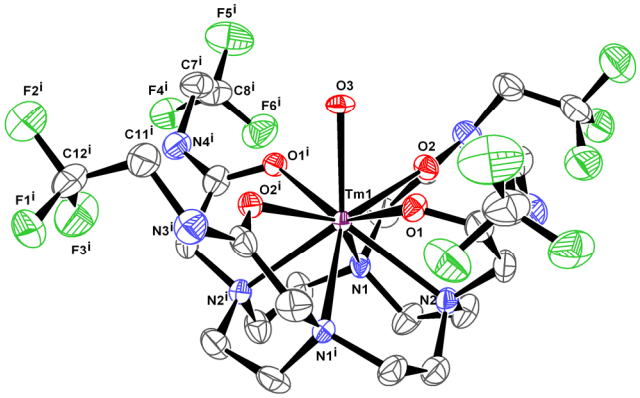

Figure 2-5: X-ray crystal structure of Tm-DOTAm-F12, top view showing left-handed (Λ) helicity of pendant arms (ORTEP, 50% probability level). Hydrogen and chlorine atoms omitted for clarity

The C_2 symmetric structure of Tm-DOTAm-F12 contains two pairs of six chemically equivalent fluorine nuclei that are positioned between 5.28 – 6.76 Å from the Tm(III) center, with an average ^{19}F – Tm(III) distance of 6.26 Å, shown Table 2-2. The angle θ is defined by the ^{19}F – Tm(III) vector and the principle magnetic axis of the metal that extends through the center of the plane formed by the four nitrogen atoms of the cyclen backbone. This is shown in **Error! Reference source not found.**, with the angle θ generated by use of the dark green dummy atom. The average θ value for

Tm-DOTAm-F12 is 77° (ranging from 67° to 83°) and is consistent with equatorial trifluoromethyl groups. Full X-ray refinement calculations are provided in the following

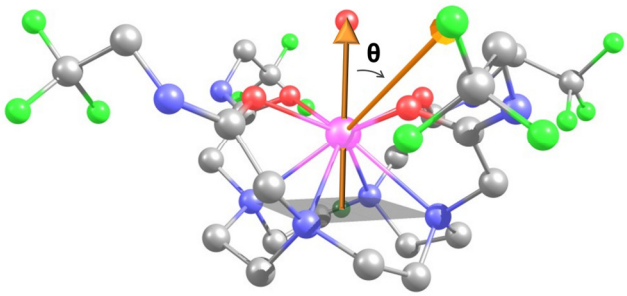

,

Figure 2-6: DFT-optimized structure of Tm-DOTAm-F12. The angle θ is defined by the Ln (III) – ^{19}F vector and the principle magnetic dipolar axis, which extends through the lanthanide ion into the center of the plane formed by the nitrogen atoms (represented by the dark green dummy atom).

Table 2-2: Ln-F distances, d, and the angle, θ, between the lanthanide-fluorine vector and the principle magnetic dipolar axis of the Tm(III) center of Tm-DOTAm-F12 from X-ray structure and DFT calculation.

	d (Å)		θ^b (°)	
	X-ray structure[a]	DFT calculations	X-ray structure[a]	DFT calculations
F1	6.75	6.74	82	85
F2	6.69	6.71	67	70
F3	5.28	5.18	83	85
F4	6.76	6.72	82	86
F5	6.74	6.74	67	71
F6	5.33	5.16	83	86
F7		6.76		87
F8		6.76		73
F9		5.21		87
F10		6.72		86
F11		6.74		71
F12		5.18		86
average	6.26	6.22	77	81

[a] The X-ray crystal structure of Tm-DOTAm-F12 is centrosymmetric and contains two pairs of six chemically equivalent fluorines. [b] The angle, θ, was calculated from the ^{19}F – Tm^{3+} vector and the principle magnetic axis of the Tm^{3+} metal that extends through the center of the plane formed by the four nitrogen atoms (N1-N2-N1#-N2#) of the chelate (detail of θ is shown **Error! Reference source not found.**)

Table 2-3: Crystal data and structure refinement for $[Tm\text{-}DOTAm\text{-}F12]^{3+}$.

Identification code	13251sqz	
Empirical formula	$C_{24}\ H_{38}\ Cl_4\ F_{12}\ N_8\ O_5\ Tm$	
Formula weight	1057.35	
Temperature	123(2) K	
Wavelength	1.54178 Å	
Crystal system	Orthorhombic	
Space group	Cmca	
Unit cell dimensions	a = 25.5559(18) Å	α = 90°
	b = 18.5893(13) Å	β = 90°
	c = 18.6003(14) Å	γ = 90°
Volume	8836.4(11) $Å^3$	
Z	8	
Density (calculated)	1.590 Mg/m^3	
Absorption coefficient	6.819 mm^{-1}	
F(000)	4184	
Crystal color, morphology	white, block	
Crystal size	0.1 x 0.1 x 0.1 mm^3	
Theta range for data collection		3.46 to 68.30°
Index ranges	$-30 \le h \le 30$, $-22 \le k \le 22$, $-22 \le l \le 17$	
Reflections collected	46172	
Independent reflections	4109 [R(int) = 0.0378]	
Observed reflections	3496	
Completeness to theta = 68.30°		98.8%
Absorption correction	Multi-scan	
Max. and min. transmission	0.7531 and 0.5364	
Refinement method	Full-matrix least-squares on F^2	
Data / restraints / parameters	4109 / 0 / 254	
Goodness-of-fit on F^2	1.0^{83}	
Final R indices [I>2sigma(I)]		$R1$ = 0.0635, $wR2$ = 0.1853
R indices (all data)	$R1$ = 0.0711, $wR2$ = 0.1928	
Largest diff. peak and hole	3.791 and -1.558 e.$Å^{-3}$	

Table 2-4: Atomic coordinates (×104) and equivalent isotropic displacement parameters (Å2 × 103) for [Tm-DOTAm-F12]$^{3+}$. Ueq is defined as one third of the trace of the orthogonalized Uij tensor.

	x	y	z	U_{eq}
Tm1	3435(1)	5000	0	17(1)
Cl1	5000	3872(2)	1008(2)	58(1)
Cl2	3268(1)	3070(1)	3074(1)	46(1)
Cl3	5000	6018(2)	1136(2)	65(1)
O1	3720(2)	6175(2)	74(2)	25(1)
O2	3718(2)	4921(2)	1172(2)	26(1)
O3	4353(2)	5000	0	25(1)
N1	2826(2)	4200(2)	790(3)	24(1)
N2	2827(2)	5786(2)	796(3)	25(1)
N3	3785(2)	4304(3)	2227(3)	37(1)
N4	3795(2)	7239(3)	692(3)	38(1)
F1	3825(2)	5002(2)	3587(3)	54(1)
F2	4459(2)	5676(3)	3239(3)	73(2)
F3	3703(2)	5735(3)	2719(3)	66(1)
F4	3826(2)	8595(3)	21(2)	53(1)
F5	4459(2)	8275(3)	-662(3)	77(2)
F6	3701(2)	7748(3)	-728(3)	62(1)
C1	2576(3)	3613(4)	360(3)	38(2)
C2	2406(3)	3859(4)	-365(3)	39(2)
C3	2406(3)	4638(3)	1127(4)	39(2)
C4	2576(3)	5359(3)	1375(4)	38(2)
C5	3164(3)	6344(3)	1113(3)	36(1)
C6	3584(2)	6583(3)	580(3)	31(1)
C7	4232(3)	7489(4)	265(4)	40(2)
C8	4057(3)	8023(4)	-267(5)	51(2)
C9	3161(3)	3883(3)	1345(3)	36(1)
C10	3576(2)	4411(3)	1584(3)	33(1)
C11	4226(3)	4734(4)	2478(4)	42(2)
C12	4056(3)	5277(5)	3000(4)	49(2)

Table 2-5: Anisotropic displacement parameters (Å2 × 103) for $[Tm\text{-}DOTAm\text{-}F12]^{3+}$. The anisotropic displacement factor exponent takes the form: $-2\pi 2$ [h2 a* 2U11 + ... + 2 h k a* b* U12]

_U_{11}	U_{22}	U_{33}	U_{23}	U_{13}	U_{12}	
Tm1	18(1)	17(1)	17(1)	-2(1)	0	0
Cl1	38(1)	69(2)	67(2)	16(2)	0	0
Cl2	63(1)	38(1)	38(1)	14(1)	-2(1)	0(1)
Cl3	46(2)	76(2)	74(2)	-14(2)	0	0
O125(2)	18(2)	33(2)	-4(2)	5(2)	-3(2)	
O225(2)	36(2)	16(2)	2(2)	0(2)	-3(2)	
O313(3)	29(3)	33(3)	1(2)	0	0	
N124(2)	24(2)	24(2)	-5(2)	2(2)	-6(2)	
N225(2)	24(2)	26(2)	-5(2)	1(2)	-1(2)	
N339(3)	38(3)	34(3)	3(2)	-3(2)	0(2)	
N436(3)	41(3)	36(3)	-1(3)	-2(2)	-7(2)	
F150(3)	84(4)	29(2)	-5(2)	9(2)	-7(2)	
F258(3)	89(4)	73(3)	-24(3)	-2(2)	-16(3)	
F361(3)	55(3)	83(4)	-10(3)	-17(3)	11(2)	
F448(3)	28(2)	82(4)	3(2)	-3(2)	7(2)	
F561(3)	80(3)	89(4)	36(3)	17(3)	-6(3)	
F658(3)	77(3)	51(3)	6(2)	-13(2)	-10(2)	
C144(4)	37(3)	33(4)	-2(3)	2(3)	-19(3)	
C242(4)	41(3)	34(4)	-5(3)	2(3)	-14(3)	
C336(4)	33(3)	47(4)	1(3)	21(3)	-2(3)	
C444(4)	31(3)	39(4)	-3(3)	16(3)	-1(3)	
C538(3)	37(3)	34(3)	-16(3)	4(3)	-3(3)	
C639(3)	20(3)	36(3)	1(2)	-5(3)	2(2)	
C733(3)	29(3)	58(4)	0(3)	4(3)	-5(3)	
C836(4)	45(4)	74(5)	5(4)	5(4)	-6(3)	
C941(3)	35(3)	31(3)	16(3)	3(3)	-4(3)	
C10	36(3)	40(3)	21(3)	0(3)	4(3)	4(3)
C11	35(3)	62(4)	30(3)	1(4)	-7(3)	-1(4)
C12	37(4)	66(5)	44(4)	-6(4)	-12(3)	-10(4)

Table 2-6: Hydrogen coordinates (× 104) and isotropic displacement parameters (Å2 × 103) for [Tm-DOTAm-F12]$^{3+}$.

___	x	y	z	U(eq)
H10A	4463	5320	281	30
H10B	4430	4575	131	30
H3N	3690(30)	4270(40)	2810(40)	45
H4N	3680(30)	7740(50)	720(40)	46
H1A	2828	3212	304	46
H1B	2268	3427	625	46
H2A	2112	4202	-307	47
H2B	2273	3439	-637	47
H3A	2119	4698	774	46
H3B	2264	4370	1543	46
H4A	2826	5302	1777	46
H4B	2268	5625	1558	46
H5A	3333	6153	1552	44
H5B	2948	6763	1252	44
H7A	4395	7076	14	48
H7B	4499	7707	583	48
H9A	3331	3444	1152	43
H9B	2944	3741	1762	43
H11A	4393	4976	2063	51
H11B	4489	4415	2704	51

The crystal structure of Tm-DOTAm-F12 together with the solution NMR data enabled testing the predicted structure of the macrocyclic lanthanide complexes by gas-phase DFT calculations. Gas-phase calculations were performed using Gaussian09[101] with a B3LYP functional and the 6-31G(d) basis set and RECP of Dolg *et al.* for the light elements, and a related valence basis set, [5s4p3d]-GTO, for the Tm(III) that separately accommodates both the core and valence electrons.[102-104] The optimized geometry of [Tm-DOTAm-F12]$^{3+}$ obtained by DFT calculations is congruent with the crystal structure (Figure 2-7) [100].

The average ^{19}F – Tm(III) distance (6.22 Å) and angle θ (81°) are in agreement with the orientation of the ^{19}F nuclei observed in the crystal structure (Figure 2-5, Figure 2-4, and Table 2-2). Furthermore, the SAP geometry is confirmed with an interplanar angle of 36.8° between the N_4 and O_4 planes. Relative energies of Tm-DOTAm-F12 with and without a coordinated water molecule indicate that the hydrated form is favored by -11.5 kcal/mol (Table 2-7). Overall, NMR spectroscopy, X-ray crystallography, and DFT calculations are in agreement; they confirm the SAP conformation of the complexes, the equatorial position of the trifluoromethyl groups, and the presence of one bound water molecule.

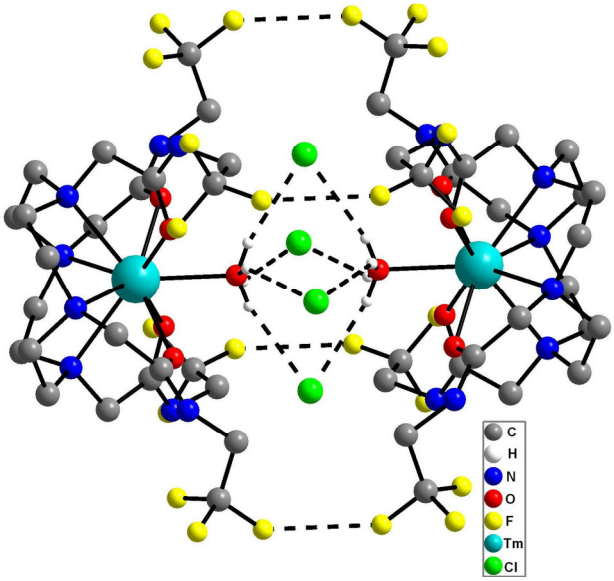

Figure 2-7: The SAP geometry of Tm-DOTAm-F12 provides room for a coordinating water molecule.

The SAP geometry of Tm-DOTAm-F12 provides room for a coordinating water molecule.[100] Nine-coordinate structures, with one bound water molecule, have been reported for similar tetraamide complexes such as [Dy-DTMA]$^{3+}$,[97] [Eu-DOTAM]$^{-}$,[105] and chiral Ln-DOTAm complexes with arms possessing stereogenic centers.[106] In the crystal structure, this water molecule at the ninth coordination site forms hydrogen bonds with the bridging Cl^- anions (Figure 2-7).

Table 2-7: Calculated (DFT) total energy change for $[Tm\text{-}DOTAm\text{-}F12]^{3+}$ and $[Tm\ DOTAm\ F12]^{3+}$ • H2O forms of the complex.

$[Tm\text{-}DOTAm\text{-}F12]^{3+} + H_2O \rightarrow [Tm\text{-}DOTAm\text{-}F12]^{3+} \bullet H_2O$ (Equation 1)

Compounds	**Sum of electronic and zero-point Energies (a.u.)**	**Sum of electronic and thermal Enthalpies (a.u.)**	**Sum of electronic and thermal Free Energies (a.u.)**
$[Tm\text{-}DOTAm\text{-}F12]^{3+} \bullet H_2O$	-2987.720819	-2987.669499	-2987.807808
$[Tm\text{-}DOTAm\text{-}F12]^{3+}$	-2911.309796	-2911.261081	-2911.396634
sH_2O	-76.395168	-76.391390	-76.412841
Reaction (Equation 1)	**Change in Energy (ΔE, kcal/mol)[a]**	**Change in Enthalpy (ΔH, kcal/mol)[a]**	**Change in Free Energy (ΔG, kcal/mol)[a,b]**
	-9.95	-10.68	1.05

[a] 1 a.u. = 627.509 kcal/mol.

[b] Gibbs free energy change (ΔG) was calculated at 298 K/ 1atm.

Hydrogen bonds between coordinated water molecules and counter ions (PF_6 or trifluoromethanesulfonate) have been previously observed in macrocyclic tetraamide crystal structures,[97,105,106] but are not expected to be present in solution. Interestingly, the solid-state packing structure of $[Tm\text{-}DOTAm\text{-}F12]^{3+}$ reveals two intramolecular hydrophobic F-F interactions by the adjacent trifluoromethyl groups (Figure 2-8). The short F-F distance of 2.76 Å is less than the sum of the van der Waals-radii (2.94 Å); contacts of this type are rare and, in most cases, a consequence of dense packing.[107] These interactions (H-Cl and F-F) link the molecules together in a dimeric, "top-to-top" fashion (Table 2-7). Full crystal structure data, atomic coordinates, and displacement parameters are provided in Table 2-4, Table 2-5, and Table 2-6.

2.5 Paramagnetic Relaxation Enhancement in Water

The sensitivity of M-DOTAm-F12 complexes is higher than that of all previously reported fluorine probes, including the only other ^{19}F – Ln complex that has been evaluated as an MRI contrast agent.[83] Part of this higher sensitivity is due to the presence of twelve ^{19}F nuclei which are chemically equivalent by NMR and MRS. While the X-ray crystal structure demonstrated two nonequivalent pairs of six ^{19}F nuclei, the single ^{19}F resonance observed by NMR/MRS suggests their exchange in solution occurs at a rate faster than the NMR timescale. The higher number of chemically equivalent fluorines per probe is necessary to increase the sensitivity of the probe. The presence of nonequivalent fluorines complicates MR image acquisition, and can lead to artifacts and decreased SNR.[108]

A greater component to the increased sensitivity of M-DOTAm-F12 complexes comes from the paramagnetic nature of the metals. Paramagnetic relaxation enhancement (PRE) can decrease T_1 by two orders of magnitude (from 1 s to <10 ms) offering up to 10-fold higher SNR with a reduction in acquisition time.[109] The enhanced relaxation mechanisms at high magnetic fields are described by the Bloch-Redfield-Wangsness (BRW) theory in terms of the electron-nucleus dipole-dipole and Curie relaxation processes.[82,109-112] As a result, the longitudinal (R_1) and transverse (R_2) relaxation rates are defined by the following relationships (Equations 2-3 to 2-7):[82]

$$R_1 = \frac{2}{15}\left(\frac{\mu_0}{4\pi}\right)^2 \frac{\gamma_F^2 \mu_{\text{eff}}^2}{d^6}\left(\frac{7\tau_{R+e}}{1+\omega_e^2\tau_{R+e}^2} + \frac{3\tau_{R+e}}{1+\omega_F^2\tau_{R+e}^2}\right) + \frac{2}{5}\left(\frac{\mu_0}{4\pi}\right)^2 \frac{\omega_F^2 \mu_{\text{eff}}^4}{(3kT)^2 d^6} \frac{3\tau_R}{1+\omega_F^2\tau_R^2} \quad (2\text{-}3)$$

$$R_2 = \frac{1}{15}\left(\frac{\mu_0}{4\pi}\right)^2 \frac{\gamma_F^2 \mu_{\text{eff}}^2}{d^6}\left(4\tau_{R+e} + \frac{3\tau_{R+e}}{1+\omega_e^2\tau_{R+e}^2} + \frac{13\tau_{R+e}}{1+\omega_F^2\tau_{R+e}^2}\right)$$

$$+ \frac{1}{5}\left(\frac{\mu_0}{4\pi}\right)^2 \frac{\omega_F^2 \mu_{\text{eff}}^4}{(3kT)^2 d^6}\left(4\tau_R + \frac{3\tau_R}{1+\omega_F^2\tau_R^2}\right) \quad (2\text{-}4)$$

$$\mu_{\text{eff}}^2 = g_J^2 \mu_B^2 J(J+1) \quad (2\text{-}5)$$

$$\omega_e = \left(\frac{g_J \mu_B}{\hbar}\right) B_0 \quad (2\text{-}6)$$

$$\tau_{\text{R+e}} = (\tau_{\text{R}}^{-1} + T_{1e}^{-1}) \quad (2\text{-}7)$$

Where d is the $^{19}\text{F} - \text{M}^{(\text{II})/(\text{III})}$ distance, μ_0 is the vacuum permeability, γ_F is the gyromagnetic ratio of ^{19}F nuclei, T is the absolute temperature, and k is the Boltzmann constant. The effective magnetic moment, μ_{eff}, is proportional to the effective electron g-factor (g_J), the Bohr magneton (μ_B), and the electron angular momentum, $J(J+1)$ (Equation 2-5). The Zeeman frequency of fluorine, ω_f, and the electron frequency, ω_e, are both functions of the magnetic field strength, B_0 (Equation 2-6). The τ_{R+e} term is dependent on the rotational correlation time (τ_R) and the electron spin longitudinal relaxation time (T_{1e}) (Equation 2-7). Together these equations define the relationship of R_1 and R_2 to the effective magnetic moment (μ_{eff}) of the metal, the $^{19}\text{F} - \text{M}^{\text{II/III}}$ distance (d), rotational correlation time (τ_R), field strength (B_0), and temperature (T). Plotting these parameters and their effect on R_1 and R_2 is shown in Figure 2-8, Figure 2-9. These figures show that while R_1 has a target area for magnetic field strength as well as for τ_R, R_2 continues to increase with either value. Since R_2 ultimately controls

the SNR obtained, a medium of optimal R_1 and R_2 values that result in effective imaging characteristics do potentially have limitations if high τ_R values are concomitantly with higher field strengths. Keeping τ_R values at 1000 ps or less suggests that there is virtually no limit to higher field strengths. Such high τ_R values correspond to supramolecular chemical structures. The τ_R values reported for probes similar to M-DOTAm-F12 are generally no higher than 200 ps.

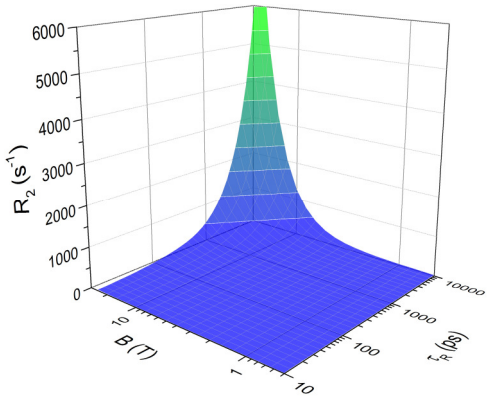

Figure 2-8: Longitudinal relaxation rate of ^{19}F nuclei of Tm-DOTAm-F12 as a function of the applied magnetic field, B_0, and the rotational correlation time, τ_R. The analysis is based on Equation (3) and is done at 37 °C using the mean Tm-19F distance determined from X-ray crystallography (6.26 Å), assuming a magnetic moment, μeff, of 7.6 BM and an electronic relaxation time, τ_e, of 0.20 ps, values typical of TmIII complexes.

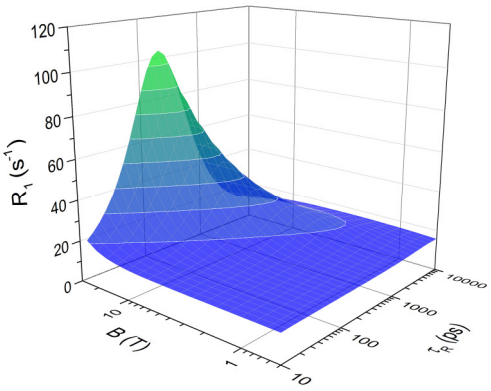

Figure 2-9: Transverse relaxation rate of ^{19}F nuclei of Tm-DOTAm-F12 as a function of the applied magnetic field, B_0, and the rotational correlation time, τ_R. The analysis is based on Equation (4) and is done at 37 °C using the mean Tm-^{19}F distance determined from X-ray crystallography (6.26 Å), assuming a magnetic moment, μ_{eff}, of 7.6 BM and an electronic relaxation time, τ_e, of 0.20 ps, values typical of Tm^{III} complexes.

Optimizing the sensitivity of ^{19}F MRI contrast agents requires understanding of each of these relationships. In this work, the effect of the metal on the longitudinal (R_1) and transverse (R_2) relaxation rates of the ^{19}F nuclei of M-DOTAm-F12 complexes is investigated. Their T_1 and T_2 relaxation times ($R_1 = 1/T_1$ and $R_2 = 1/T_2$) are reported in Table 2-1. Since each complex shares the same ligand, the values of d and τ_R are

mostly constant across the family of complexes. The differences in relaxation times are thus primarily a consequence of the effective magnetic moment (μ_{eff}) of the metal. Each lanthanide metal has a characteristic μ_{eff}/μ_B value that is relatively invariant with ligand structure (Figure 2-1).

The BRW theory correctly predicts how each lanthanide ion affects the relaxation rates of ^{19}F nuclei. The shorter T_1 relaxations times near 6 ms are observed for those lanthanide ions that have the higher effective magnetic moments (μ_{eff} of ~ 10), namely Tb(III), Dy(III), and Ho(III).[109] The ^{19}F nuclei of the Fe(II) complex of DOTAm-F12 display the shortest longitudinal relaxation time (5.7 ms), suggesting that the iron complex also has a high μ_{eff}. In comparison, the fluorine nuclei of the diamagnetic La(III) complex and the free ligand display characteristically long longitudinal relaxation times (570 ms and 880 ms, respectively). Incorporation of any of these four paramagnetic metal ions with high magnetic moments reduces the ^{19}F T_1 time by over two orders of magnitude. Interestingly, Er(III) also displays a high effective magnetic moment (9.6), comparable to that of Tb(III), Dy(III), and Ho(III) and higher than that of Gd^{III} (7.9). Yet the T_1 of the fluorine nuclei of the Er(III) and Gd(III) complexes are comparable. At the other end of the spectrum, Eu(III) and Yb(III) which have lower effective magnetic moments, decrease ^{19}F T_1 values to a much lesser extent.

The effect of the paramagnetic metal on the transverse relaxation times of the fluorine nuclei is more pronounced but follows a similar trend, with the notable exception of Gd(III). Tb(III), Dy(III), and Ho(III), which have the higher μ_{eff}, shorten the T_2 of the fluorines to a greater extent, up to 500 fold compared to the diamagnetic

analog. In contrast, Eu(III) and Yb(III) which have lower μ_{eff}, decrease the T_2's of the ^{19}F barely 10 fold. Gd(III), predictably, has a substantially greater effect on the transverse relaxation time of the fluorines than on their longitudinal ones, and a greater effect on T_2 than any other lanthanide. The T_2 of the ^{19}F nuclei of the Gd(III) complex is estimated to be <0.1 ms, but could not be accurately determined using the CPMG pulse sequence due to extensive broadening of the ^{19}F resonance. The relaxation data for M-DOTAm-F12 align with reported T_1 and T_2 values for previously reported ^{19}F – Ln(III) complexes.[83] In the current study, the T_1 and T_2 relaxation times are roughly double when moving from Ho(III) to Er(III) and again from Er(III) to Tm(III); this trend more closely follows the decreasing μ_{eff} of the metals than that previously reported.[83] The Fe(II) complex presents interesting, and promising, properties: this is the only case where the effect of the paramagnetic metal ion on the T_2 of the fluorines is comparable to its effect on T_1. T_1:T_2 relaxation times decrease to 5.7 : 5.6 ms.

2.5.1 Signal Enhancement in an MR Image

Increasing the sensitivity of fluorine probes by decreasing the relaxation times of the fluorine nuclei is a balancing act. On one hand, decreasing T_1 allows for a greater number of scans to be acquired in a same amount of time, thereby increasing the SNR of an image. On the other hand, when T_2 values are very short, it is very hard to acquire images that are only T_1-weighted. Too short a T_2 and any benefit from decreasing T_1 is lost. At first estimate, the most sensitive probes will have the shortest T_1, maintain a T_2/T_1 ratio as close to 1 as possible, and have a T_2 no less than 2 ms. This is where Fe(II) and the different lanthanide ions differentiate themselves.

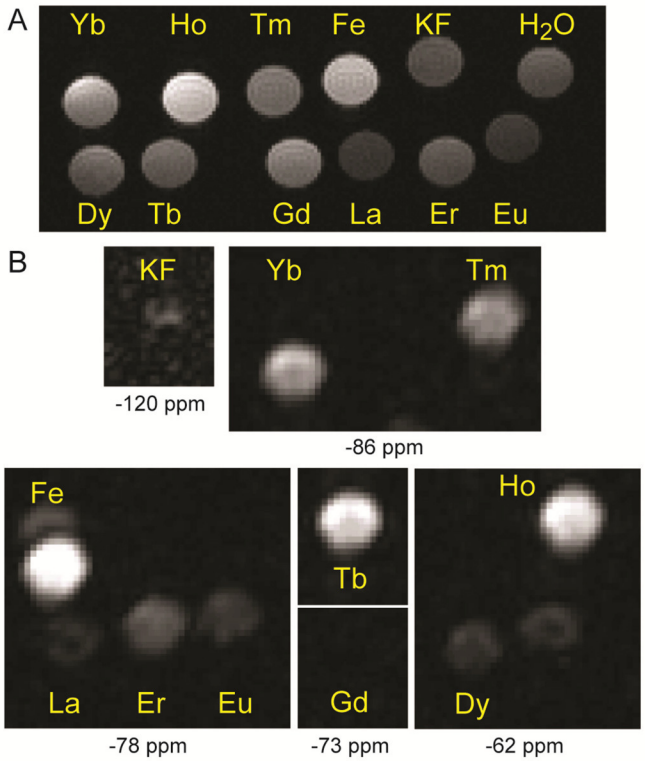

Figure 2-10: MRI phantom images of [M-DOTAm-F12]$^{2+/3+}$ in water at 5.0 mM. B_0 = 9.4 T, T = 33 °C. A) ^{1}H 3D gradient-echo images, T_R = 10 ms, T_E = 1.78 ms, 20°, FOV: 20 mm × 40 mm × 20 mm, matrix: 128 × 256 × 128, resolution: 0.156 mm isotropic. ^{19}F gradient-echo images, T_R = 5 ms, T_E = 1.34 ms, 90°, FOV: 32 mm × 32 mm, matrix: 64 × 64, slice thickness = 10 mm, na = 64. Images are shown with the same intensity scale after 2D zero-padding. Transmitter offset for 19F images: -120 ppm KF; -86 ppm Yb, Tm; -78 ppm Fe, La, Er, Eu; 73 ppm Tb, Gd,; -62 ppm Ho, Dy. SNR for ^{19}F images: Yb, 20, Tm, 18; Fe, 40; La, 5.2; Er, 13; Eu, 7.8; Tb, 31; Gd, 1; Ho, 31; Dy, 6.0.

Figure 2-10 shows gradient echo images collected at 9.4 T with 5 mM samples of [M-DOTAm-F12]$^{2+/3+}$. For the fluorine images, the imaging frequency for each complex corresponds to the chemical shift of the ^{19}F resonance (Figure 2-2). A repetition time, T_R, of 5.0 ms was selected because the shortest T_R values result in the highest SNR providing that T_2 is sufficiently long.[83] In order to be able to compare SNR, each image was obtained with the same acquisition time (20.5 s) and the same resolution (in plane: 0.5 x 0.5 mm^2, and 10 mm slice thickness).

As is clearly apparent from these images, the SNR of solutions of these complexes is *not* directly proportional to T_1 of the fluorine nuclei, nor does the trend in

SNR follow the trend in effective magnetic moment of the metal ion. Instead, with the exception of Tb(III), SNR more closely follows the T_2/T_1 ratio. One extreme case is Gd(III) whose effect on the T_2 of ^{19}F is so pronounced (< 0.1 ms) that the highly broadened ^{19}F resonance of the complex results in negligible signal intensity both by NMR (Figure 2-2) and MRI (Figure 2-10). Dy(III) and Eu(III) have T_2/T_1 values higher than Gd(III) but that are still relatively poor, between 0.1 and 0.4. They yield SNR's between 6 and 8 ms that are comparable to that of the diamagnetic La(III) complex. Er(III), Tm(III), and Yb(III) have better T_2/T_1 values between 0.4 and 0.6, which lead to SNRs two to four times higher than La(III) (SNR of 10-20). Ho(III) is the best of the lanthanide ions, with a T_2/T_1 of 0.7 leading to a SNR of 30. Notably, none of the lanthanide ions are as efficient as Fe(II). Indeed, Fe(II) has the highest T_2/T_1 ratio of 0.98 and also the highest SNR of 40, eight times greater than the diamagnetic La^{III} complex.

Comparison of the SNR of the MR image of solutions of the diamagnetic La(III) complex with that obtained with the Ho(III) complex demonstrate the strength of using paramagnetic metal ion. Both of these complexes have similar T_2/T_1 value of 0.7. However, the T_1 of the fluorines of the paramagnetic Ho(III) complex is 75 times shorter than that of the diamagnetic La(III) complex. This enables the acquisition of 75 times more scans in a same amount of time with the Ho(III) complex than with the La(III) one. As a result, exchanging La(III) by Ho(III) results in a six fold increase in SNR.

A T_2/T_1 value near one signifies that the effect of T_1 is maximized compared to the negative effect of line broadening induced by short T_2. Comparison with other

published lanthanide-based ^{19}F complexes indicates that although the trend between T_2/T_1 and SNR holds, with some exception (Tb(III) in this study), the lanthanide ion which yields the most sensitive probe is not necessarily the same for all ligands. Er^{III} was reported to be a good metal for the previously reported DOTA and DOPA-based system. [81,83] In the case of DOTAm-F12, however, it yields a SNR three times lower than Ho(III) and Tb(III) in water. The extent to which a same lanthanide ion influences the sensitivity of a fluorine probe depends substantially on the ligand. With the aryl trifluoromethyl substituted Ln-DOTA complexes studied by Chalmers *et al.,* Ho(III) increases the sensitivity 2.4 times over the diamagnetic Y(III).[82] In this study, Ho(III) increases the sensitivity of the fluorine nuclei six times over its diamagnetic counterpart. Ligand and complex geometry, and especially Ln-^{19}F distances, must be taken into consideration when designing paramagnetic fluorine MR probes. In addition, Fe(II), which has not been previously studied in the design of fluorine MRI probes, yields higher sensitivity than any of the lanthanides. The resulting SNR with the Fe^{II} complex was eight times that of the diamagnetic analog.

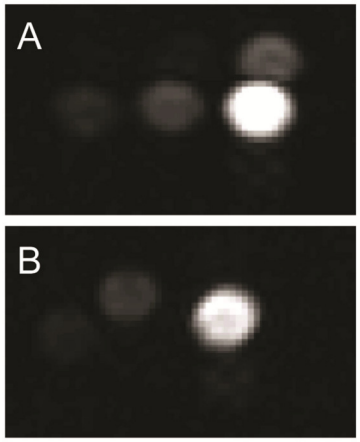

Figure 2-11: ^{19}F gradient-echo images in water. A) [Fe-DOTAm-F12]$^{2+}$ samples at three concentrations (0.5 mM, 1 mM, 5 mM, left to right), -73 ppm, T_R = 10 ms, T_E = 1.34 ms, 90°, FOV: 32 mm × 32 mm, matrix: 64 × 64, slice thickness = 10 mm, na = 512. SNR for Fe: 0.5 mM, 5.2; 1 mM, 9.9; 5 mM, 49. B) [Tm-DOTAm-F12]$^{3+}$ samples at three concentrations (0.5 mM, 1 mM, 5 mM, left to right), -86 ppm, T_R = 20 ms, T_E = 1.34 ms, 90°, FOV: 32 mm × 32 mm, matrix: 64 × 64, slice thickness = 10 mm, na = 256. Images are shown with the same intensity scale after two dimensional zero-padding. B_0 = 9.4 T, T = 33°C. SNR for Tm: 0.5 mM, 3.3; 1 mM, 6.6; 5 mM, 31.

Gradient echo ^{19}F images of Fe^{II} and Tm^{III} DOTAm-F12 at three different concentrations in water are given in Figure 2-11. For each metal the image collection

parameters (T_R, T_E, and number of acquisitions) were altered so to achieve the best SNR while maintaining a constant acquisition time of 5.5 min. This enables us to compare the two best complexes more accurately. With these parameters, a ^{19}F MR image of a 5 mM solution of Fe^{II}-DOTAm-F12 has a SNR of 49. With the same acquisition time and the same resolution, a 5 mM solution of the Tm(III) analog is 37% less sensitive (SNR = 31). The theoretical limit of detection (where SNR > 3)[113] is extrapolated as 280 μM for the Fe(II) complex and 430 μM for the Tm(III) derivative. The best paramagnetic ions—that is—the ones that yield the highest SNR, is highly dependent on the media. With the intent to produce a clinically viable contrast agent, the data obtained in water must be compared to data obtained in blood. It was anticipated that since the trifluoromethyl groups of the $[M\text{-DOTAm-F12}]^{2+/3+}$ complexes are hydrophobic, they would likely interact with the proteins present in blood and in particular with serum albumin, the most ubiquitous protein found in the mammalian bloodstream. Serum albumin has previously been reported to bind hydrophobic molecules such as perfluorocarbons.[114,115] Binding to large proteins such as albumins is anticipated to affect substantially the rotational correlation time, τ_R, of the complex. As is apparent from Equations 2-3, 2-4 and 2-7, and the BRW theoretical predictions of R_1 and R_2 as a function of varying field strength and τ_R time discussed earlier (plotted in Figure 2-8 and Figure 2-9), changes in rotational correlation times influence T_1 and T_2 differently, with longer τ_R (larger macromolecules) affecting T_2 noticeably more than T_1. The T_2/T_1 ratio of the fluorine nuclei for the different metal ions is thus expected to be different in blood than in water, and as such so would their sensitivity.

Table 2-8: ^{19}F T_1 and T_2 relaxation times, T_2/T_1 ratio, and MRI SNR of M-DOTAm-F12 complexes in rat veinous blood at 37°C.

	T_1 [a] (ms)	T_2 [a] (ms)	T_2/T_1 [a]	SNR[b,c]
La-DOTAm-F12	700	29	0.041	n.d.
Ho-DOTAm-F12	10	2.7	0.26	~1[d]
Tm-DOTAm-F12	36	6.4	0.18	7.2
Yb-DOTAm-F12	170	12	0.071	4.6
Fe^{II}-DOTAm-F12	7.7	4.4	0.57	34

Conditions: [a] B_0: 7.0 T, rat veinous blood. [b] M-DOTAm-F12 = 5 mM, B_0: 9.4 T. [c] SNR were obtained at the optimum frequency for each complex using images shown in Figure 8B: Ho, -62 ppm; Tm, -86 ppm; Yb, -86 ppm; Fe, -78 ppm. [d] ^{19}F MRI signal could not be observed.

Experimentally, fluorine T_1 values in blood were found to be comparable to those measured in water (Figure 2-8). As predicted, unfortunately, the fluorine transverse relaxation times, T_2, are substantially shorter in blood than in water. For the Ho(III) complex, the fluorine T_2 in blood was decreased two-fold to 2.7 ms, and was not able to imaged due to its T_2/T_1 ratio and thus significant signal loss. The T_2/T_1 ratio of the Tm(III) complex similarly decreases over three-fold to 0.18 as its T_2 decreases from 16 to 6.4 ms. Similar reduction of fluorine T_2 *in vivo* compared to *in vitro* was observed recently with a ^{19}F – Dy(III) chitosan polymer.[116] In the current study, the Fe(II) complex behaves substantially better in rat blood than any of its lanthanide counterparts. The fluorine T_1 relaxation time of the Fe(II)-DOTAm-F12 surprisingly became longer by 2 ms, whereas the T_2 relaxation time decreases by only 1 ms. As a result, the T_2/T_1 ratio dropped from 0.98 in water to only 0.57 in blood. It therefore appears, based on fluorine relaxation times alone, that the Fe^{II}-DOTAm-F12 complex would be more appropriate for *in vivo* ^{19}F MRI.

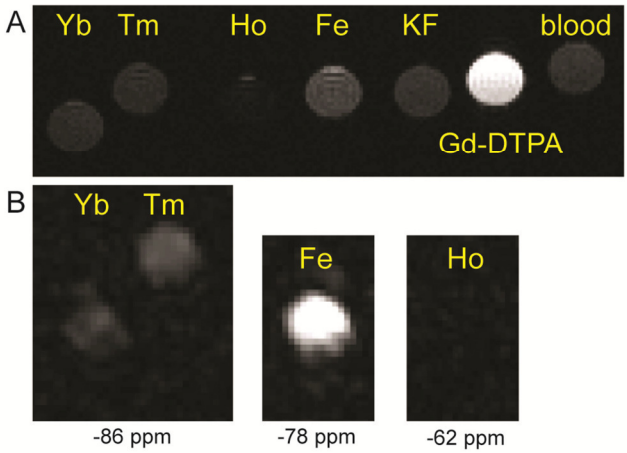

Figure 2-12: MRI phantom images of M-DOTAm-F12 in rat blood at 5.0 mM. B0 = 9.4 T, T = 33 °C. A) ^{1}H 3D gradient-echo images, T_R = 10 ms, T_E = 1.78 ms, 20°, FOV: 20 mm × 40 mm × 20 mm, matrix: 128 × 256 × 128, resolution: 0.156 mm isotropic. B) ^{19}F gradient-echo images, TR = 5 ms, TE = 1.34 ms, 90°, FOV: 32 mm × 32 mm, matrix: 64 × 64, slice thickness = 10 mm, na = 64. Images are shown with the same intensity scale after 2D zero-padding. Transmitter offset for ^{19}F images: -86 ppm Yb, Tm; -78 ppm Fe; -62 ppm Ho. SNR for 19F images: Yb, 4.6, Tm, 7.2; Fe, 34; Ho, ~1.

Gradient echo MR images obtained at 9.4 T illustrate the relative strength of the [M-DOTAm-F12]$^{2+/3+}$ complexes in rat blood (Figure 2-12 and Table 2-8 for SNR). As with the study in water, each image was collected with a T_R of 5.0 ms and with a center frequency corresponding to the chemical shift of each complex, shown in Figure 2-12. Under these conditions, and as a consequence of the short T_2, the SNR of the Tm(III) derivative drops by more than half in blood (7.2) *versus* water (18.1). Similarly, the SNR obtained with the Yb(III) in blood is 25% lower than that observed in water. The Ho(III) complex is affected the most by blood. Whereas in water it is one of the most sensitive complexes with an SNR of 31, in blood, the signal could not be detected, likely as a consequence of the too short T_2 depicted in Figure 2-13.

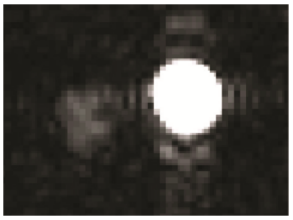

Figure 2-13: ^{19}F gradient-echo images of Ho-DOTAm-F12 in water (right) and rat blood (left). B_0 = 9.4 T, T = 33°C, T_R = 5 ms, T_E = 1.23 ms, 90°, FOV: 32 mm × 32 mm, matrix: 64 × 64, slice thickness = 10 mm, na = 512, 2D zero-padding.

Likewise, De Luca *et al.* could not detect a chitosan polymer substituted with fluorinated Ho(III) complexes in mice with an imaging time of 1 h.[116] It is possible that more recent imaging sequences, such as SWIFT,[117] which could alleviate the effects of a short T_2 if it is not too short, and could enable more sensitive ^{19}F MRI with the lanthanide complexes. Fe^{II}-DOTAm-F12, unlike its lanthanide counterparts, remained an efficient contrast agent in blood with a sensitivity that is barely affected by blood components. The SNR for the image obtained with the Fe(II) complex was 34, 85% of that obtained in water.

The limit of detection of the Fe(II) and Tm(III) complexes in blood was estimated from ^{19}F gradient echo images of blood samples containing increasing concentrations of either complex can be seen in Figure 2-14.

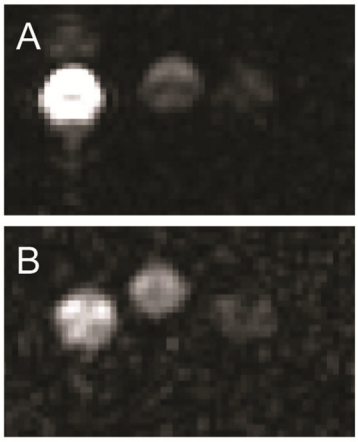

Figure 2-14: ^{19}F gradient-echo images of A) Fe(II)-DOTAm-F12 and B) Tm DOTAm-F12 in rat blood at three concentrations (5 mM, 1 mM, 0.5 mM from left to right). B_0 = 9.4 T, T = 33°C, T_R = 10 ms, T_E = 1.34 ms, 90°, FOV: 32 mm × 32 mm, matrix: 64 × 64, slice thickness = 10 mm, na = 64. 2D zero-padding. Tm images are shown with two times higher intensity than Fe images. SNR for Fe: 5 mM, 40; 1 mM, 8.8; 0.5 mM, 4.3. SNR for Tm: 5 mM, 8.2; 1 mM, 5.3; 0.5 mM, 2.3.

Note that in this figure the image intensity of the Tm(III) complex has been increased by a factor of two *versus* that of Fe(II). Using the linear relationship between the SNR and the complex concentration, Fe^{II}-DOTAm-F12 is estimated to have a limit of detection of 300 μM in blood. However, the SNR of the Tm complex

is not proportional to the concentration at concentration of 5 mM. Images in Figure 2-12 suggest unequal distribution of Tm complex in the blood for 5 mM sample.

Three-dimensional ^{19}F MRI of phantoms of M-DOTAm-F12 complexes at 5 mM were collected in blood with a resolution of 0.5 mm × 0.5 mm × 1 mm (Figure 2-15). Signal from three complexes was observed in number of slices in this 3D acquisition which took 33 min (Yb, Tm, and Fe). The signal of Fe complex has the highest signal intensity and was observed in largest number of slices. Together, the resolution and sensitivity obtained with Fe(II)-DOTAm-F12 are suitable for *in vivo* imaging of rat of mouse models in biomedical research applications.

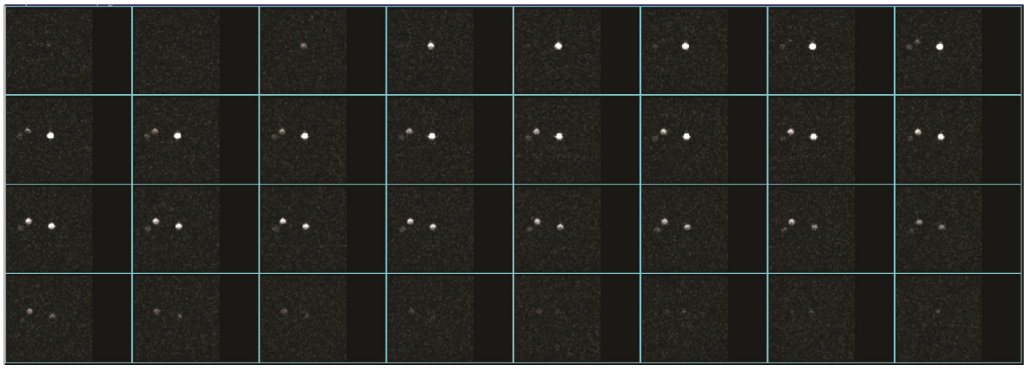

Figure 2-15: Three-dimensional ^{19}F MRI phantom images of M-DOTAm-F12 at 5.0 mM in rat blood. Samples are positioned as Figure 2-14. B_0 = 9.4 T, T = 33 °C, TR = 15 ms, TE = 0.99 ms, 90°, FOV: 32 mm × 32 mm × 32 mm, matrix: 64 × 64 × 32, na = 64, acquisition time = 33 min.

2.6 Conclusions and Future Directions

A series of metal complexes of the C4 symmetric ligand, DOTAm-F12 has been synthesized and its potential as ^{19}F MRI contrast agents has been evaluated. Nine paramagnetic lanthanide ions were studied, Eu(III), Gd(III), Tb(III), Dy(III), Ho(III), Er(III), Tm(III), and Yb(III), as well as the diamagnetic La(III) analog. Fe(II), which is known to form stable complexes with macrocyclic polyaminocarboxamides, was

also evaluated. As opposed to currently used organic polyfluorocarbons such as perfluoro 15-crown-5 and other reported paramagnetic fluorine probes, the complexes of DOTAm-F12 are all highly soluble in water. These complexes are more sensitive than other fluorinated MR probes, in part due to the twelve fluorine nuclei which are chemically equivalent and thus appear as a single resonance by ^{19}F NMR. Importantly, the sensitivity of these probes is further increased due to the paramagnetic nature of the metals which shorten T_1, thereby enabling more scans to be acquired in the same amount of time. Shorter longitudinal relaxation times were observed for those metals with the highest effective magnetic moment, μ_{eff}. SNR observed in MR images, however, are not proportional to T_1 but to a combination of T_1 and the T_2/T_1 ratio. Higher SNR were observed for complexes that were characterized with fluorine T_2/T_1 as close to unity as possible. In water, the Ho(III) and Fe(II) complexes were the most sensitive, followed by Tm(III) and Yb(III). In blood, however, presumed binding of the probe with proteins result in a decrease in the transverse relaxation times of the fluorines for all the metal complexes except Fe(II). As a result, the Ho(III) complex could no longer be observed by MRI. The Tm(III)-complex of DOTAm-F12 is the most sensitive lanthanide complex in blood. Fe(II)-DOTAm-F12, which as a T_2/T_1 closer to unity, is the most sensitive fluorine contrast agent in blood with a limit-of-detection of 0.30 mM.

Further studies will evaluate the effect of magnetic field strength, B_0, on the efficacy of the paramagnetic fluorine probes. Evaluation of the Bloch-Redfield-Wangsness (BRW) theory (equations 2-3 – 2-7) indicate that the longitudinal relaxation rates of the fluorine nuclei should be strongly dependent on B_0, with higher

relaxation rates observed at higher magnetic fields (Figure 6). This dependence suggest that, unlike gadolinium-based contrast agents whose longitudinal relaxivity sharply decrease at medium-to-high magnetic field, paramagnetic fluorine probes would be more sensitive, and perhaps more appropriate, for high field MRI.

Ligand design and the rotational correlation times are two other parameters that could also be exploited to further increase the sensitivity of this class of contrast agents. Figures 6 and 7 show the predicted effect of τ_R and B_0 on the longitudinal and transverse relaxivities, respectively, as calculated from the Bloch-Redfield-Wangsness equations using the Ln-^{19}F observed in the Tm-DOTAm-F12 crystal structure and assuming a magnetic moment, μeff, of 7.6 BM and an electronic relaxation time, τ_e, of 0.20 ps, values typical of Tm(III) complexes. Slow rotational correlation times, corresponding to rigid and large macromolecules, are expected to decrease T_2 substantially while having a minimal effect on T_1. As a result, the T_2/T_1 ratio of such macromolecules would be too small for the probes to be detectable by MRI. However, a small increase in the rotational correlation time (τ_R near 200 ps) would increase R_1 five-fold while having a moderate effect on R_2. Such medium-sized complexes could be more sensitive MR probes. Another possibility is to reduce the negative effect of short T_2 on SNR by using alternative MR pulse sequences.

Overall, the increased sensitivity of these highly water-soluble paramagnetic fluorine probes render them attractive alternatives to standard proton imaging by MRI. The ease by which MRI scanners can be re-tuned to the frequencies of fluorines further facilitates the promulgation of these probes. The ability to perform multi-color MR imaging with fluorine probes and the possibility to alter the transverse and

longitudinal relaxation rates of the fluorine nuclei as a function of the metal-^{19}F distance and rotational correlation times open interesting opportunities for the design of ratiometric responsive MRI contrast agents.

The next chapter will focus on how manipulation of the field strength and the ligand field environment affects the MR properties of [M-DOTAm-F12]$^{2+/3+}$. The studies that will be presented in Chapter 3 will look at different methods for increasing fluorine sensitivity rather than only looking at the effect of different metals.

2.7 Experimental Materials and Methods

General considerations. Starting materials were obtained from commercial suppliers and used without further purification. Water was distilled and further purified by a Millipore cartridge system (resistivity 1.8×10^7 Ω). All organic extracts were dried over anhydrous $MgSO_4$ and solvents were removed under reduced pressure with a rotary evaporator. All synthetic compounds were characterized at the LeClaire-Dow Chemical Instrumentation Facility at the Department of Chemistry at the University of Minnesota, Twin-Cities. ^{1}H NMR spectra were recorded on a Varian 500 at 500 MHz, ^{13}C NMR spectra on a Bruker AV-500 at 125 MHz, and ^{19}F NMR spectra were recorded on a Varian VXR-300 at 282 MHz. The residual solvent peak was used as an internal reference for ^{1}H and ^{13}C NMR; $CFCl_3$ was used as an internal reference for ^{19}F NMR of organic intermediates; and KF was used as an external standard for metal complexes. Data for ^{1}H NMR are reported as follows: chemical shift (δ, ppm), multiplicity (s, singlet; br s, broad singlet; d, doublet; t, triplet; q, quartet; m, multiplet), integration, coupling constant (Hz). Data for ^{13}C NMR and ^{19}F NMR are reported in terms of chemical shift (δ, ppm). Longitudinal (T_1) and transverse (T_2)

relaxation times of ^{19}F nuclei of metal complexes in D_2O were measured using the inversion recovery sequence and the Carr-Purcell-Meiboom-Gill sequence, respectively. A delay time of 30 ms and acquisition time of 64 ms were used for the collection of ^{1}H and ^{19}F NMR spectra of the paramagnetic M-DOTAm-F12 complexes. Mass spectra (HR, high resolution; ESI, electrospray ionization) were recorded on a Bruker BioTOF II at the Waters Center of Innovation for Mass Spectrometry at the Department of Chemistry at the University of Minnesota, Twin-Cities. X-ray data collection and structure solution were conducted at the X-Ray Crystallographic Laboratory of the Department of Chemistry at the University of Minnesota. All calculations were performed using Pentium computers using the current SHELXTL suite of programs.

2-Bromo-*N*-(2,2,2-trifluoroethyl)acetamide (2-12): 2,2,2trifluoroethyl amine (4.00 mL, 27.5 mmol) was dissolved in CH_2Cl_2 (50 mL) and magnetically stirred in an ice bath. A solution of K_2CO_3 (16.5 g, 120 mmol) in distilled H_2O (50 mL) and a solution of bromoacetyl bromide (2.40 mL, 27.7 mmol) in CH_2Cl_2 (50 mL) were simultaneously added dropwise over 30 min, after which the reaction was allowed to warm to ambient temperature and stirred for 1 h. The organic phase was separated and washed with distilled H_2O until the washes were at neutral pH (5 × 25 mL), washed with brine (1 × 20 mL), dried over $MgSO_4$ and concentrated under reduced pressure to yield product (**2-12**) as white crystals (4.88 g, 80.7 %). ^{1}H NMR (500 MHz, $CDCl_3$, δ): 3.88-3.97 (m, 4 H), 7.19 (br s, 1 H). ^{13}C NMR (75 MHz, $CDCl_3$, δ): 28.9, 41.9 (q, J = 34.8 Hz), 124.4, (q, J = 277 Hz), 167.4. ^{19}F NMR (282 MHz, $CDCl_3$, δ): -72.9 (t, J =

8.7 Hz). HRMS-ESI (*m/z*): $[M + H]^+$ calc for $C_4H_5BrF_3NO$: 219.9579; found: 219.9579. The observed isotopic distribution matched the calculated one.

2,2',2'',2'''-(1,4,7,10-Tetraazacyclododecane-1,4,7,10-tetrayl)tetrakis(*N*-(2,2,2- trifluoroethyl)acetamide) (DOTAm-F12, 2-1): Cyclen (500. mg, 2.91 mmol) was dissolved in dry CH_3CN (150 mL) and magnetically stirred. K_2CO_3 (7.06 g, 51.2 mmol) was then added, followed by the acetamide **2-12** (2.56 g, 11.6 mmol). The reaction was then heated to 60 °C for 8 h, cooled to ambient temperature, filtered, and concentrated under reduced pressure and further dried under high vacuum for 3 days yielding the free ligand as a white powder (1.82 g, 85.9%). ^{1}H NMR (500 MHz, CD_3OD, δ): 2.52 (q, *J* = 2.5 Hz, 4 H), 2.59 (q, *J* = 3.0 Hz, 4 H), 2.74 (t, *J* = 5.0 Hz, 4 H), 3.01 (t, *J* = 5.0 Hz, 4 H), 3.16 (s, 4 H), 3.25 (s, 4 H), 3.78 (q, *J* = 9 Hz, 8 H). ^{13}C NMR (125 MHz, CD_3OD, δ): 41.1 (q, *J* = 33.8 Hz), 58.7, 62.7, 126.1 (q, *J* = 276 Hz), 173.9. ^{19}F NMR (282 MHz, CD_3OD, δ): -72.9 (t, *J* = 8.7 Hz). HRMS-ESI (*m/z*): $[M + Na]^+$ calc for $C_{24}H_{36}F_{12}N_8O_4$: 751.2560; found: 751.2562.

Ln-DOTAm-F12 complexes: Representative procedure for **La-DOTAm-F12 (2-2):** Aqueous $LaCl_3$ (101 mg, 0.412 mmol) was added to a stock solution of DOTAm-F12 **(2-1)** (300. mg, stock solution of 10 mg/mL ligand dissolved in 1:1 CH_3OH and CH_3CN, 0.412 mmol) and magnetically stirred. The acidic mixture was basified with aqueous NaOH to pH 8 and heated at 75 °C for 90 h. Volatiles were removed under reduced pressure and further dried under high vacuum overnight yielding a white powder (**2-2**, 397 mg, 99.0%). ^{1}H NMR (500 MHz, D_2O, δ): see

Figure S1. ^{19}F NMR (282 MHz, D_2O, δ): -72.9 ppm. HRMS-ESI (*m/z*): $[M-H]^{2+}$ calc for $C_{24}H_{36}F_{12}LaN_8O_4$: 433.0827; found: 433.0809.

Eu-DOTAm-F12 (2-3): DOTAm-F12 (150. mg, 0.206 mmol), $EuCl_3$ (53.2 mg, 0.206 mmol), 87 h, white powder (**2-3**, 200. mg, 98.5%). ^1H NMR (500 MHz, D_2O, δ): see Figure S2. ^{19}F NMR (282 MHz, D_2O, δ): -73.5 ppm. HRMS-ESI (*m/z*): $[M-H]^{2+}$ calc for $C_{24}H_{36}EuF_{12}N_8O_4$: 439.5862; found: 439.5867. The observed isotopic distribution matched the calculated one.

Gd-DOTAm-F12 (2-4): DOTAm-F12 (150. mg, 0.206 mmol), $GdCl_3$ (54.3 mg, 0.206 mmol), 100 h, white powder (**2-3**, 201 mg, 98.6%). ^1H NMR (500 MHz, D_2O, δ): see Figure S3. ^{19}F NMR (282 MHz, D_2O, δ): -72.9 ppm. HRMS-ESI (*m/z*): $[M-H]^{2+}$ calc for $C_{24}H_{36}F_{12}GdN_8O_4$: 442.0876; found: 442.0858. The observed isotopic distribution matched the calculated one.

Tb-DOTAm-F12 (2-5): DOTAm-F12 (150. mg, 0.206 mmol), $TbCl_3$ (54.2 mg, 0.206 mmol), 85 h, white powder (**2-5**, 203 mg, >99.0%). ^1H NMR (500 MHz, D_2O, δ): see Figure S4. ^{19}F NMR (282 MHz, D_2O, δ): -54.0 ppm. HRMS-ESI (*m/z*): $[M-H]^{2+}$ calc for $C_{24}H_{36}F_{12}N_8O_4Tb$: 442.5883; found: 442.5902.

Dy-DOTAm-F12 (2-6): DOTAm-F12 (150. mg, 0.206 mmol), DyI_3 (112 mg, 0.206 mmol), 104 h, brown powder (**2-6**, 257 mg, 98.0%). ^1H NMR (500 MHz, D_2O, δ): see Figure S5. ^{19}F NMR (282 MHz, D_2O, δ): -52.2 ppm. HRMS-ESI (*m/z*): [M-

$H]^{2+}$ calc for $C_{24}H_{36}DyF_{12}N_8O_4$: 445.0902; found: 445.0899.The observed isotopic distribution matched the calculated one.

Ho-DOTAm-F12 (2-7): DOTAm-F12 (150. mg, 0.206 mmol), $HoBr_3$ (83.3 mg, 0.206 mmol), 99 h, pink powder (**2-7**, 231 mg, 98.4%). ^1H NMR (500 MHz, D_2O, δ): see Figure S6. ^{19}F NMR (282 MHz, D_2O, δ): -62.0 ppm. HRMS-ESI (*m/z*): $[M-H]^{2+}$ calc for $C_{24}H_{36}F_{12}HoN_8O_4$: 445.5908; found: 445.5911.

Er-DOTAm-F12 (2-8): DOTAm-F12 (150. mg, 0.206 mmol), $ErBr_3$ (83.6 mg, 0.206 mmol), 98 h, yellow powder (**2-8**, 231 mg, 99.1%). ^1H NMR (500 MHz, D_2O, δ): see Figure S7. ^{19}F NMR (282 MHz, D_2O, δ): -77.5 ppm. HRMS-ESI (*m/z*): $[M-H]^{2+}$ calc for $C_{24}H_{36}ErF_{12}N_8O_4$: 446.0907; found: 446.0922.The observed isotopic distribution matched the calculated one.

Tm-DOTAm-F12 (2-9): DOTAm-F12 (150. mg, 0.206 mmol), $TmCl_3$ (56.7 mg, 0.206 mmol), 98 h, white powder (**2-9**, 203 mg, 98.0%). ^1H NMR (500 MHz, D_2O, δ): see Figure S8. ^{19}F NMR (282 MHz, D_2O, δ): -85.6 ppm. HRMS-ESI (*m/z*): $[M-H]^{2+}$ calc for $C_{24}H_{36}F_{12}N_8O_4Tm$: 447.6927; found: 447.6923.

Yb-DOTAm-F12 (2-10): DOTAm-F12 (150. mg, 0.206 mmol), $YbCl_3$ (57.6 mg, 0.206 mmol), 77 h, white powder (**2-10**, 206 mg, >99.0%). ^1H NMR (500 MHz, D_2O, δ): see Figure S9. ^{19}F NMR (282 MHz, D_2O, δ): -77.3 ppm. HRMS-ESI (*m/z*):

$[M-H]^{2+}$ calc for $C_{24}H_{36}F_{12}N_8O_4Yb$: 450.0950; found: 450.0959.The observed isotopic distribution matched the calculated one.

Fe^{II}-DOTAm-F12 (2-11): DOTAm-F12 (50. mg, 69 μmol) was dissolved in CH_3OH and CH_3CN (1:1, 25 mL) and magnetically stirred. Iron(II)trifluoromethanesulfonate (24.3 mg, 68.7 μmol) was added and the reaction mixture was heated to 70 °C for 30 h under argon. The resultant mixture was then concentrated under reduced pressure to yield the complex Fe^{II}-DOTAm-F12 (**2-11**) as an orange solid in quantitative yield. ^1H NMR (500 MHz, D_2O, δ): see Figure S10. ^{19}F NMR (282 MHz, D_2O, δ): -70.9 ppm. HRMS-ESI (*m/z*): $[M]^{2+}$ calc for $C_{24}H_{36}F_{12}FeN_8O_4$: 392.1009; found: 392.1000.

Hydration number (*q*). The hydration number, *q*, of Dy-DOTAm-F12 was determined by ^{17}O NMR according to the procedure of Peters.[96] Standard solutions of $[Dy\text{-}DTPA]^{2-}$ (5% ligand excess) and Dy-DOTAm-F12 (5% ligand excess) were prepared at 60.4 mM and 50.0 mM, respectively, each with 10% D_2O in H_2O with 0.05% ^{17}O-labeled H_2O. ^{17}O resonances were recorded on a Bruker Avance-HD 500 at 67.7 MHz. The resultant chemical shifts of the ^{17}O resonances were plotted as a linear function of concentration; seven concentrations were used for each species. The hydration number of Dy-DOTAm-F12 relative to that of $[Dy\text{-}DTPA]^{2-}$ (q =1) was calculated by the ratio of the slopes (Figure 2-3).

Gas-phase DFT calculations.

Geometry optimizations were carried out using Gaussian09[101] with B3LYP functional by employing the 6-31G(d) basis set for the light elements (H, C, N, O and F) and the quasirelativistic effective core potential (RECP) of Dolg *et al.* and the related [5s4p3d]-GTO valence basis set for the Tm^{III}.[102,103] This RECP accommodates 46+4fn electrons in the core for the lanthanide and the outermost 11 electrons are treated explicitly. Such RECP has been earlier used in DFT studies to understand the structure and energetics of the lanthanide complexes.[104] The absence of imaginary frequency in the frequency calculation confirmed the optimized geometry as energy minima.

X-ray crystallography

Data collection. A crystal (approximate dimensions $0.1 \times 0.1 \times 0.1$ mm^3) was placed onto the tip of a 0.1 mm diameter glass capillary and mounted on a Bruker D8 Photon 100 CMOS diffractometer for a data collection at 123(2) K.[118] A preliminary set of cell constants was calculated from reflections harvested from three sets of 20 frames. These initial sets of frames were oriented such that orthogonal wedges of reciprocal space were surveyed. This produced initial orientation matrices determined from 620 reflections. The data collection was carried out using CuKα radiation (normal parabolic mirrors) with a frame time of 7.5/15 seconds and a detector distance of 4.0 cm. A randomly oriented region of reciprocal space was surveyed to the extent of one sphere and to a resolution of 0.83 Å. Twelve sets of frames with a sweep width of 0.5 were collected as determined by the data collection strategy in APEX II. The intensity data were corrected for absorption and decay (SADABS) using an empirical correction for absorption anisotropy.[119] Final cell constants were calculated from the

xyz centroids of 2823 strong reflections from the actual data collection after integration (SAINT).[120]

S**tructure solution and refinement.** The structure was solved using SHELXS-97 and refined using SHELXL-97.[121] The space group Cmca was determined based on systematic absences and intensity statistics. A direct-methods solution was calculated which provided most non-hydrogen atoms from the E-map. Full-matrix least squares / difference Fourier cycles were performed which located the remaining non-hydrogen atoms. All non-hydrogen atoms were refined with anisotropic displacement parameters. The protons on the nitrogen atoms were found from the difference map and refined with individual isotropic displacement parameters. All remaining hydrogen atoms were placed ideally and refined with relative isotropic displacement parameters. The final full matrix least squares refinement converged to $R1$ = 0.0635 and $wR2$ = 0.1928 (F^2, all data). Platon Squeeze[122,123] was used to remove the electron density that resulted from the disordered solvent. The Squeeze results were consistent in removing 40 water molecules in the unit cell.

MRI. Magnetic resonance images of samples in water and in blood were acquired at 33 °C in 3 mm NMR tubes using a 9.4-T, 31-cm horizontal bore magnet (Magnex Scientific, Oxford, UK) interfaced with a Varian Direct Drive console (Varian, Palo Alto, CA, USA). The magnet was equipped with a gradient insert capable of reaching 450 mT/m in 200 μs (Resonance Research, Inc., Billerica, MA). A linear radiofrequency (RF) surface coil (12 mm diameter) tunable to both ^{1}H (400.2 MHz) and ^{19}F (376.6 MHz) frequencies was used to transmit RF and receive the signal. ^{1}H 3D gradient echo images were acquired using following parameters:

repetition time (T_R) = 10 ms, echo time (T_E) = 1.78 ms, field-of-view (FOV) = 20 mm x 40 mm x 20 mm, matrix = 128 x 256 x 128, number of averages (na) = 1. ^{19}F gradient echo images were acquired at resonance frequencies of compounds using following parameters: T_E = 1.34 ms, FOV = 32 mm x 32 mm, matrix = 64 x 64, slice thickness = 10 mm, flip angle = 90°. T_R was varied from 5 to 100 ms and na from 64 to 512. 3D gradient-echo images were acquired at -78 ppm using following parameters: T_R = 15 ms, T_E = 0.99 ms, FOV = 32 mm x 32 mm x 32 mm, matrix = 64 x 64 x 32, flip angle = 90°, na = 64. SNR was calculated by taking the ratio of the mean intensity in the circular region of interest (ROI) containing whole sample over the mean intensity in an identically sized noise region of the image.

3 Optimization of ^{19}F Paramagnetic Relaxation Enhancement: Lanthanide-Induced Shift, Effective Magnetic Moment, and BRW Theory Minimizations

3.1 Introduction

The design principles required to produce a viable ^{19}F MRI contrast agent require that the paramagnetic metal induce both a change in chemical shift, and a change in relaxation rates. Both of these effects can be obtained by using paramagnetic metal ions, which affect the ^{19}F lanthanide-induced shift (^{19}FLIS) and the ^{19}F paramagnetic relaxation enhancement (^{19}FPRE) of the complex. Not all fluorine probes, however, produce both of these effects to an appreciable degree.[40]

Fluorine-based MRI contrast agents are also limited by sensitivity, which can be increased by optimizing the relaxation times of the ^{19}F nuclei. In Chapter 2, the importance of incorporating a paramagnetic metal center within a ^{19}F MRI contrast agent was examined using the same ligand, DOTAm-F12 (**2-1**), which decreased T_1 and T_2 values by over two orders of magnitude in some cases.

Classic BRW theory indicates that a number of variables dictate R_1 and R_2 values for a given probe, with the most pronounced effects dictated by (and typically measured in) the ^{19}F-Ln(III) distance d (Å), the effective magnetic moment of the lanthanide μ_{eff} (Bohr magnetons), the electronic relaxation time T_{1e} (ps), and the rotational correlation time τ_R (ps).[7,31,124,125] The first term in each equation is known as the dipolar term, and the second term is the Curie term. Both contribute to R_1 and R_2 but at higher fields the Curie term is dominant. Equation 2-3 & 2-4 are provide below.

$$R_1 = \frac{2}{15}\left(\frac{\mu_0}{4\pi}\right)^2 \frac{\gamma_F^2 \mu_{\text{eff}}^2}{d^6}\left(\frac{7\tau_{R+e}}{1+\omega_e^2\tau_{R+e}^2} + \frac{3\tau_{R+e}}{1+\omega_F^2\tau_{R+e}^2}\right) + \frac{2}{5}\left(\frac{\mu_0}{4\pi}\right)^2 \frac{\omega_F^2 \mu_{\text{eff}}^4}{(3kT)^2 d^6} \frac{3\tau_R}{1+\omega_F^2\tau_R^2} \quad (2\text{-}3)$$

$$R_2 = \frac{1}{15}\left(\frac{\mu_0}{4\pi}\right)^2 \frac{\gamma_F^2 \mu_{\text{eff}}^2}{d^6}\left(4\tau_{R+e} + \frac{3\tau_{R+e}}{1+\omega_e^2\tau_{R+e}^2} + \frac{13\tau_{R+e}}{1+\omega_F^2\tau_{R+e}^2}\right) + \frac{1}{5}\left(\frac{\mu_0}{4\pi}\right)^2 \frac{\omega_F^2 \mu_{\text{eff}}^4}{(3kT)^2 d^6}\left(4\tau_R + \frac{3\tau_R}{1+\omega_F^2\tau_R^2}\right) \quad (2\text{-}4)$$

McConnel-Robertson theory (equation 2-2) dictates the magnitude of ^{19}FLIS as dependent as well on *d*, as well as the angle θ between the ^{19}F nuclei and the principal dipolar axis of the Ln(III).

$$^{19}\text{FLIS} = C_{\text{D}} \frac{\beta^2}{60(\text{kT})^2} \frac{(3\cos^2\theta - 1)}{d^3} B_2^0 \quad (2\text{-}2)$$

Different ligand designs affect relaxation and chemical shift properties imparted by paramagnetic Ln(III) ions. Trends in the data can be identified and exactly how the values of θ, *d*, μ_{eff}, T_{1e}, and τ_R affect the observed trends can be determined, as well as how each ligand affects these properties of the coordination complex. Data obtained from these studies can provide valuable information about ^{19}F probe systems that can be used to further enhance ^{19}F sensitivity and functionality in future probe designs.

3.2 To Determine Ideal ^{19}F Probes for MRI

When considering the impact of fluorine's R_1 and R_2 value in a contrast agent, classic BRW theory indicates that these two relaxation rates are dependent on the gyromagnetic ratio of ^{19}F (γ_F) which is constant, the Zeeman frequency of fluorine (ω_F) and the electron frequency, ω_e, which are both functions of the magnetic field strength, B_0. Work by Chalmers et al. has demonstrated that the ^{19}F R_1 and R_2 values are enhanced with increasing field strength, up to 20 T as shown in their report.[82] Higher sensitivity is predicted at higher field strengths (B_0).[82,126] However, higher field strengths also enhance R_2 rates which can lead to line broadening and decreased SNR in

MRI. Additionally, at field strengths of ca. 10 T and above, the values of τ_R and d are more significant and must be taken into consideration.

Values for d, μ_{eff}, T_{1e}, and τ_R, incorporated in two equations (2-3 and 2-4) yields two single values for the ^{19}F relaxation rates of a metal-based probe. By altering a probe's structure, R_1 and R_2 can be predicted by changing d (ligand structure), T_{1e} (metal choice, ligand structure, or field strength), τ_R (ligand structure or solution state), and/or μ_{eff} of that probe (ligand structure, metal choice). This study is in effort to understand the parameters that yield an ideal ^{19}F MRI contrast agent.

Relaxation rates and subsequent ^{19}F sensitivity are dominated by the electronics of the paramagnetic metal center. Since that metal center when chelated imparts its electronic effects on the ^{19}F nuclei, different coordination functionalities ultimately determine how the paramagnetic behavior of the metal will influence the relaxation rates and ultimately the sensitivity of the probe. The electronic properties of lanthanides vary depending on their coordination complexes, and the electronic interactions between a lanthanide and a ligand produce a unique set of parameters that all factor in to classic BRW theory. The electronic behavior imparted by a ligand on a Ln(III) ion, and the Ln(III) ion's interaction with the ligand are impacted by the ligand field environment.[127-131] Thus, each Ln(III) ion and coordination complex has a unique MR profile.

3.3 Three Ligands, Six Lanthanides

For this project, three series of ^{19}F probes were synthesized, with structures shown in Figure 3-1. In addition to DOTAm-F12 and its respective metal complexes with Tb(III), Dy(III), Ho(III), Er(III), Tm(III) and Yb(III), two new ligands were

synthesized: DOTA-F6 (**3-1**) and F-DOTPME (**3-14**), and their complexes with the same six lanthanides. These six lanthanides were chosen because they have the highest μ_{eff} values of the lanthanides(Gd (III) not considered due to the line broadening). All three ligands were constructed with a macrocyclic cyclen backbone, but have different oxygen donor functionalities used in creating their respective 8-coordinate complexes with lanthanide(III) ions, changing the relative hardness/softness of the overall chelate. In DOTAm-F12 (**2-1**), the oxygen donor groups are from amides; in DOTA-F6 (**3-1**) they are from carboxylic acids, and in F-DOTPME (**3-14**) they are from phosphonate esters.

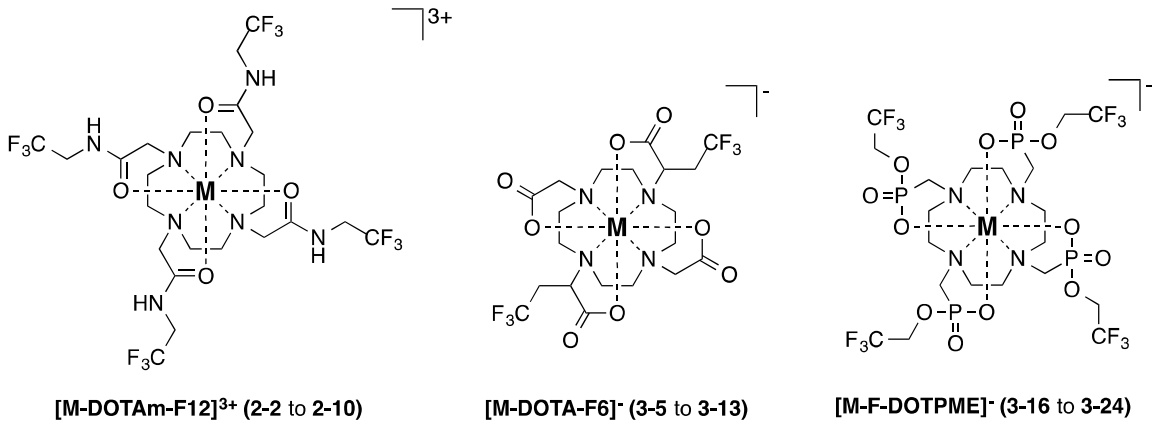

Figure 3-1: Metal complexes used in this study: $[M\text{-DOTAm-F12}]^{3+}$ (2-2 to 2-10), $[M\text{-DOTA-F6}]^{-}$ (3-5 to 3-13), and $[M\text{-F-DOTPME}]^{-}$ (3-16 to 3-24).

3.3.1 Synthesis of Metal Complexes

The detailed synthetic pathway for DOTAm-F12 (2-1) and its metal complexes is provided in Chapter 2. The synthetic pathways for the ligands DOTA-F6 (3-1) and F-DOTPME (3-14) and their metal complexes are provided in. DOTA-F6 (3-1) was synthesized by reacting the protected carboxylic acid pendant arm with cyclen under basic conditions to yield exclusively the 1,7-disubstituted product.

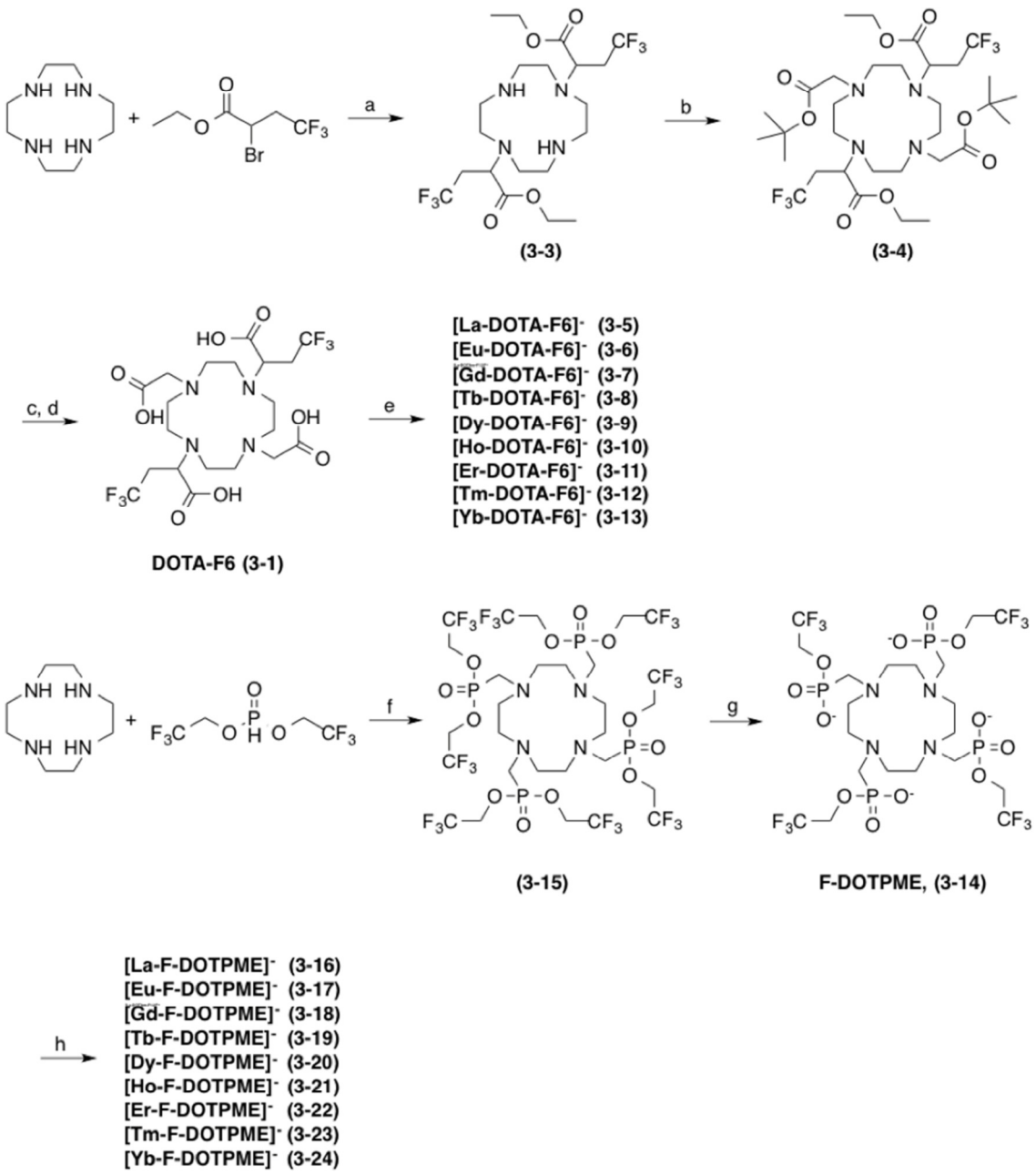

Scheme 3-1: Reagents and conditions: (a) K_2CO_3, CH_3CN, reflux, 18 h, 60.0 %; (b) tBu bromoacetate, K_2CO_3, 45 ˚C, 16 h, 96.0 %; (c) NaOH (aq.), 1 h; (d) HCl (aq.), 1 h, 93.9 % over two steps; (e) LnX_3, H_2O, reflux, 3 days, quant.; (f) paraformaldehyde, acetic acid, benzene, rt, 3 d; (g) NaOH, H_2O, 100 ˚C, 30 min; 22 ˚C, 2 d, 29% over 2 steps; (h) LnX3, H2O, reflux, 3 days, quant.

Substitution at all four 2˚ nitrogens on cyclen was desired, but only the disubstituted product was formed, most likely due to the steric bulk imparted by the protected pendant arm. The remaining two nitrogens on the macrocycle were

substituted with ^{t}Bu bromoacetate. Saponification of both ester groups yielded the free ligand as the tetrahydrochloride salt in quantitative yield. The ligand F-DOTPME **(3-14)** was synthesized by Cutler Lewandowsky over two steps according to scheme 3-1. In the first step, cyclen was reacted with bis(2,2,2-trifluoroethyl)phosphite and paraformaldehyde in benzene to form the perester **3-15**. Subsequent hydrolysis in basic water formed the ligand **3-14** as the tetrasodium salt. While this route was relatively low yielding for F-DOTPME (3-14), the syntheses of both DOTA-F6 (3-1) and F-DOTPME (3-14) are easily scalable. Their metal complexes with La(III), Eu(III), Gd(III), Tb(III), Dy(III), Ho(III), Er(III), Tm(III), and Yb(III) were each synthesized quantitatively from their respective lanthanide trihalide salts in aqueous conditions at neutral pH to form the metal complexes **3-5** to **3-13** and **3-16** to **3-24**, respectively.

3.4 Lanthanide-Induced Shift

As mentioned in Chapter 2 (section 2.4.4), the shift in a fluorine resonance caused by a paramagnetic metal is defined as the ^{19}F lanthanide-induced shift (^{19}FLIS). The ^{19}FLIS can be approximated using the McConnell-Robertson equation (equation 2-2), and is dependent on the sign and magnitude of the Bleaney coefficient (C_D), the ^{19}F-Ln(III) distance (d), and the angle between the principal magnetic dipolar axis of the Ln(III) ion (θ).

The ^{19}FLIS values for each series of complexes is reported in table 3-1. These values are averages of each ^{19}FLIS measured at five different field strengths (4.7, 9.4, 11.7, 14.1, and 16.5 T). ^{19}FLIS is independent of field strength, so the values obtained at five fields were averaged over 5 data points.

Table 3-1: Chemical shifts (δ, ppm) of DOTAm-F12, DOTA-F6, and F-DOTPME metal complexes, and change in chemical shift (Δδ, ^{19}FLIS) relative to the free ligand. aAverage chemical shifts from data acquired at 4.7, 9.4, 11.7, 14.1, and 16.5 T, 298 K.

Compound	Average δ (ppm)[a]	Δδ (ppm) (^{19}FLIS)
DOTAm-F12 (**2-1**)	-79.2	n/a
$[La\text{-}DOTAm\text{-}F12]^{3+}$	-72.9	0
$[Eu\text{-}DOTAm\text{-}F12]^{3+}$	-73.1	-0.2
$[Tb\text{-}DOTAm\text{-}F12]^{3+}$	-53.8	+19.1
$[Dy\text{-}DOTAm\text{-}F12]^{3+}$	-51.8	+21.1
$[Ho\text{-}DOTAm\text{-}F12]^{3+}$	-61.7	+11.2
$[Er\text{-}DOTAm\text{-}F12]^{3+}$	-76.9	-4.0
$[Tm\text{-}DOTAm\text{-}F12]^{3+}$	-86.8	-13.9
$[Yb\text{-}DOTAm\text{-}F12]^{3+}$	-77.0	-4.1
DOTA-F6 (**3-5**)	-75.7	n/a
$[La\text{-}DOTA\text{-}F6]^{-}$	-75.8	-0.1
$[Eu\text{-}DOTA\text{-}F6]^{-}$	-70.7	+5.0
$[Tb\text{-}DOTA\text{-}F6]^{-}$	-69.0	+6.7
$[Dy\text{-}DOTA\text{-}F6]^{-}$	-68.2	+7.5
$[Ho\text{-}DOTA\text{-}F6]^{-}$	-69.4	+6.3
$[Er\text{-}DOTA\text{-}F6]^{-}$	-70.4	+5.3
$[Tm\text{-}DOTA\text{-}F6]^{-}$	-70.1	+5.6
$[Yb\text{-}DOTA\text{-}F6]^{-}$	-70.7	+5.0
F-DOTPME (**3-14**)	-75.8	n/a
$[La\text{-}F\text{-}DOTPME]^{-}$	-75.6	+0.2
$[Eu\text{-}F\text{-}DOTPME]^{-}$	-75.7	+0.1
$[Tb\text{-}F\text{-}DOTPME]^{-}$	-32.4	+43.4
$[Dy\text{-}F\text{-}DOTPME]^{-}$	-33.6	+42.2
$[Ho\text{-}F\text{-}DOTPME]^{-}$	-56.8	+19.0
$[Er\text{-}F\text{-}DOTPME]^{-}$	-94.8	-19.0
$[Tm\text{-}F\text{-}DOTPME]^{-}$	-117.3	-41.5
$[Yb\text{-}F\text{-}DOTPME]^{-}$	-82.7	-6.9

3.4.1 ^{19}FLIS of DOTAm-F12 Complexes

The ^{19}FLIS of the DOTAm-F12 series of metal complexes was explored at 7 T in chapter 2. The values reported in table 3-1 show only slight deviations within acceptable experimental error. The sign of the Bleaney coefficient still matches these

data, none of the data points indicate a change in geometry, suggesting the entire DOTAm-F12 series of complexes adopts a similar geometry with a similar *d*.

3.4.2 ^{19}FLIS of DOTA-F6 Complexes

The ^{19}FLIS of the DOTA-F6 series of complexes displays very different behavior from DOTAm-F12. The ^{19}F chemical shift of the diamagnetic [La-DOTA-F6]$^{-}$ is in close agreement with the free ligand, and the remaining chemical shifts of the other metal complexes are all in very close agreement with each other, but not in agreement with the ligand.

This suggests that the resultant angle θ between the principal magnetic dipolar axis of the Ln(III) ions and the fluorines in DOTA-F6 complexes is ca. 45˚- 60˚. At this position, the ^{19}FLIS based on equation 2-2 approaches 0. However, the angle θ is not incorporated in the BRW equations, and significantly enhanced relaxation rates are still observed.

Why [La-DOTA-F6] shows negligible shift with respect to the ligand, while all other complexes were shifted downfield by 5-8 ppm, is possibly due to lanthanide contraction. A square-anti-prismatic (SAP) geometry for as the La(III) complex, combined with a more rigid twisted-square-anti-prismatic (TSAP) geometry for the other metals might account for this observation. X-ray crystallographic data and/or DFT calculations, however, would be required to determine if this speculation is true.

3.4.3 ^{19}FLIS of F-DOTPME Complexes

Like the DOTAm-F12 complexes, the ^{19}FLIS of the F-DOTPME series of complexes follow the signs of the Bleaney coefficients, but are much larger than those observed for DOTAm-F12. Shifts exceeding 40 ppm are observed for Tb(III), Dy(III),

and Tm(III) complexes, over twice the highest values obtained for DOTAm-F12. The Ho(III) and Er(III) F-DOTPME complexes have the same shift magnitude but of opposite sign, whereas in DOTAm-F12 these two metals produced inequivalent magnitude. This observation is not in agreement with the McConnell-Robertson theorem (equation 2-2), in that the Bleaney coefficients are not accurate when applied to various ligands. Indeed, this was a stipulation clearly indicated in the original 1972 report from Bleaney that is often overlooked.[132]

3.5 Electronic Relaxation Rates (T_{1e})

The electronic relaxation rates of Ln(III) ions have been measured by NMR in only a few cases. Looking at aqua Ln(III) cations and some Ln(III) complexes, Alsaadi et al. calculated T_{1e} values using estimated μ_{eff} and d values.[57,133] While these reports were preliminary, they did predict correctly that Tb(III) and Dy(III) most often have the highest electronic relaxation rates, and Ho(III) and Er(III) have lower values. These studies were done at low field strengths.

Aime et al. found the same trend by looking at R_1 at a single field and R_2 at multiple fields,[134] and Bertini et al. also investigated T_{1e} values by NMR but looked at higher field values (up to 14 T).[135] They assembled a nuclear magnetic relaxation dispersion (NMRD) profile for aqua-Ln(III) cations, and with the higher-field measurements were able to observe dominance of R_1 on the Curie term of BRW theory (the second term in equations 2-3 and 2-4).

3.5.1 Experimental Relaxation Data

The BRW theorems (equations 2-3 and 2-4) can be used to interpret observed relaxation rates as a function of field strength (B_0). This calculation, however, can only

be provided if the values of μ_{eff}, d, τ_R, and T_{1e} are also known (or at least can be approximated). Since the parameters μ_{eff}, d, and τ_R are independent of B_0, the relaxation rates measured at multiple field strengths can ultimately be applied to the BRW theory iteratively to determine T_{1e} as a function of field strength, and then subsequently to determine μ_{eff} for each complex.[31,82,136]

In collaboration with Prof. David Parker at Durham University, Durham, England, the relaxation rates R_1 for the ^{19}F nuclei in each series of metal complexes were measured at five different field strengths using a standard inversion-recovery pulse sequence. Measurements were taken of a 5 mM sample of each complex in D_2O on 4.7, 9.4, 11.7, 14.1, and 16.5 T instruments (188, 376, 470, 564, and 658 MHz respectively for the ^{19}F nucleus). Relaxation data for the diamagnetic La(III) complexes were used only as the control and are omitted, as well as for Gd(III) complexes which could not be determined due to extensive line broadening, even at lower field strengths.

Table 3-2: T_1 values reported are averages of three measurements obtained within 5% difference or less for each value.

DOTAm-F12: Metal	T_1 (ms), 4.7 T	T_1 (ms), 9.4 T	T_1 (ms), 11.7 T	T_1 (ms), 14.1 T	T_1 (ms), 16.5 T
Eu(III)	554	272	218	177	146
Tb (III)	8.94	5.27	4.21	3.75	3.32
Dy(III)	9.04	4.62	3.65	3.07	2.59
Ho(III)	12.4	5.54	4.62	3.58	3.42
Er(III)	12.9	10.4	7.62	5.71	4.82
Tm(III)	41.6	20.5	15.9	12.8	12.1
Yb(III)	173	112	86.1	72.0	59.1

Table 3-3: T_1 values reported are averages of three measurements obtained within 5% difference or less for each value

DOTA-F6: Metal	T_1 (ms), 4.7 T	T_1 (ms), 9.4 T	T_1 (ms), 11.7 T	T_1 (ms), 14.1 T	T_1 (ms), 16.5 T
Eu(III)	855	743	533	340	279
Tb (III)	17.1	11.9	9.18	8.35	7.18
Dy(III)	24.5	16.2	10.5	8.57	7.95
Ho(III)	17.3	9.95	7.71	6.37	6.17
Er(III)	15.9	8.89	7.52	6.76	6.19
Tm(III)	55.1	46.6	39.3	24.9	21.6
Yb(III)	172	111	99.1	83.8	77.9

Table 3-4: T_1 values reported are averages of three measurements obtained within 5% difference or less for each value.

F-DOTPME: Metal	T_1 (ms), 4.7 T	T_1 (ms), 9.4 T	T_1 (ms), 11.7 T	T_1 (ms), 14.1 T	T_1 (ms), 16.5 T
Eu(III)	899	429	348	268	245
Tb (III)	19.0	11.1	8.29	7.62	7.32
Dy(III)	13.5	7.86	6.55	5.81	4.99
Ho(III)	17.8	9.53	8.19	6.51	5.95
Er(III)	25.0	15.2	13.3	12.4	11.5
Tm(III)	49.9	39.9	34.9	22.7	21.3
Yb(III)	277	182	163	146	136

The T_1 values of the remaining complexes for DOTAm-F12, DOTA-F6, and F-DOTPME are provided in Table 3-2, Table 3-3, Table 3-4, respectively. T_1 values reported are averages of three measurements obtained within 5% difference or less for each value.

Upon initial analysis these data illustrate that the DOTAm-F12 family of complexes (Table 3-2) possess the greatest decreases in T_1, with $[Dy\text{-}DOTAm\text{-}F12]^{3+}$ showing the lowest T_1 value measured of 2.59 ms at 16.5 T. The DOTAm-F12 series also produce only one resonance in the ^{19}F NMR spectrum as previously mentioned.

The DOTA-F6 series (Table 3-3) show the longest T_1 values, and the T_1 values for the F-DOTPME series (Table 3-4) reside in between the other two systems.

These data obtained contradicts the well documented trend that a reduced Ln(III)-F distance enhances relaxation rates, as the ^{19}F nuclei of DOTA-F6 are in much closer proximity to the Ln(III) metal than they are in the case of F-DOTPME.

3.5.2 Application of BRW Theory to Determine T_{1e} and μ_{eff} - Data Minimization

The variation of experimental relaxation rate data as a function of field strength can be used to estimate values of T_{1e} and μ_{eff}. The values for μ_{eff} commonplace in the literature are 9.8, 10.3, 10.4, 9.4, 7.6, and 4.5 for Tb(III), Dy(III), Ho(III), Er(III), Tm(III), and Yb(III), respectively.[82,137-139] The data obtained are the T_1 times of each complex as a function of field strength, B_0. T_1 values are inversely proportional to R_1 values, and assuming classic behavior adherent to BRW theory, the R_1 values obtained can be used to iteratively determine the approximate values of T_{1e} and μ_{eff}. Data coding was performed in MatLab using a series of minimization scripts written by Prof. Ilya Kuprov, and modified by Alexander M. Funk of the Parker group. Singular fittings for each metal ion are first performed, followed by global fitting of the entire ligand system data. Fitting the relaxation rate data for the DOTAm-F12 complexes yields minimization values shown in Table 3-5.

The fitting algorithm subsequently generates a minimized value for d and τ_R that adhere to the initial singular fittings of μ_{eff} and T_{1e}. The adherence of relaxation rates to the BRW theory, using the values in Table 3-6, is provided in Figure 3-2. The trend lines plotted are the actual predictions of R_1 from the minimalized values of μ_{eff}, T_{1e}, d, and τ_R applied to the BRW equation (equation 2-3).

Table 3-5: Global minimizations of μ_{eff}f, T_{1e} as a function of relaxation rates for DOTAm-F12 complexes. Subsequent iterations yielded the reported values for τ_R and d.

DOTAm-F12: Metal	μ_{eff} (B. M.)	T_{1e} (ps)
Tb(III)	9.77	0.52
Dy(III)	10.4	0.36
Ho(III)	9.88	0.28
Er(III)	8.98	0.13
Tm(III)	7.31	0.12
Yb(III)	4.56	0.11
	τ_R	231 ps
	d	5.92 Å

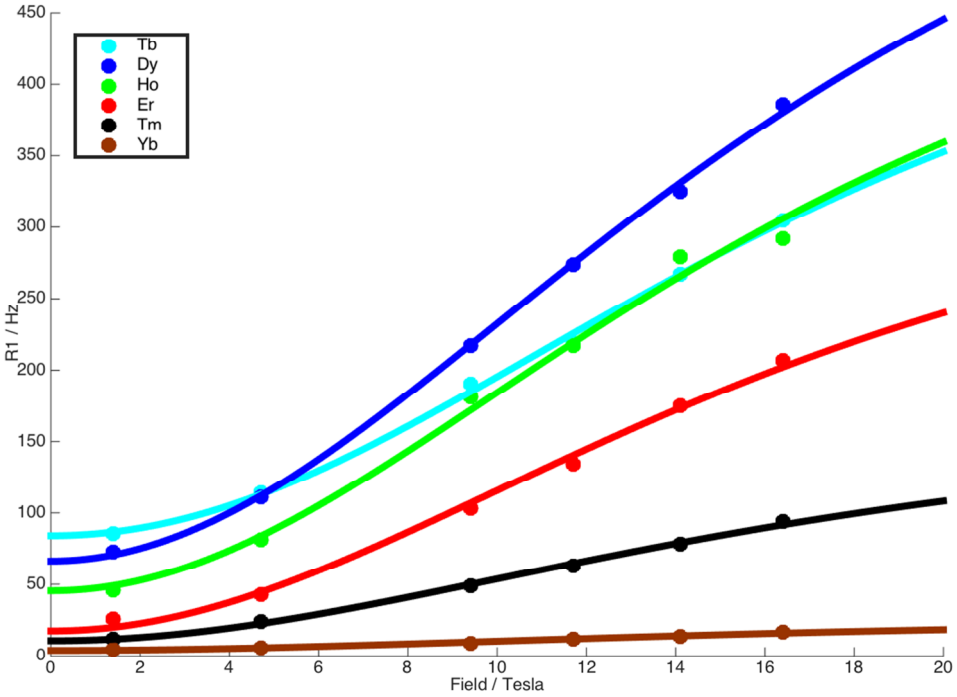

Figure 3-2: Global minimization of μ_{eff}, T_{1e}, d, and τ_R based on R_1 data at six field strengths for DOTAm-F12 complexes.

As shown in Figure 3-2, the BRW theory approximates the values of R_1 based on the defined set of parameters shown in Table 3-5. The same fitting procedure was used to reach the minimization values of μ_{eff} and T_{1e}, with subsequent generation of values for d and τ_R, and the results are provided for the DOTA-F6 series (Table 3-6and Figure 3-3), and the F-DOTPME series (Table 3-7and Figure 3-4), provided below.

Table 3-6: Global minimizations of μ_{eff}, T_{1e} as a function of relaxation rates for DOTA-F6 complexes. Subsequent iterations yielded the reported values for τ_R and d.

DOTA-F6: Metal	μ_{eff} (B. M.)	T_{1e} (ps)
Tb(III)	8.74	0.50
Dy(III)	8.96	0.27
Ho(III)	9.49	0.33
Er(III)	9.25	0.33
Tm(III)	6.85	0.031
Yb(III)	4.63	0.13
	τ_R	205 ps
	d	6.37 Å

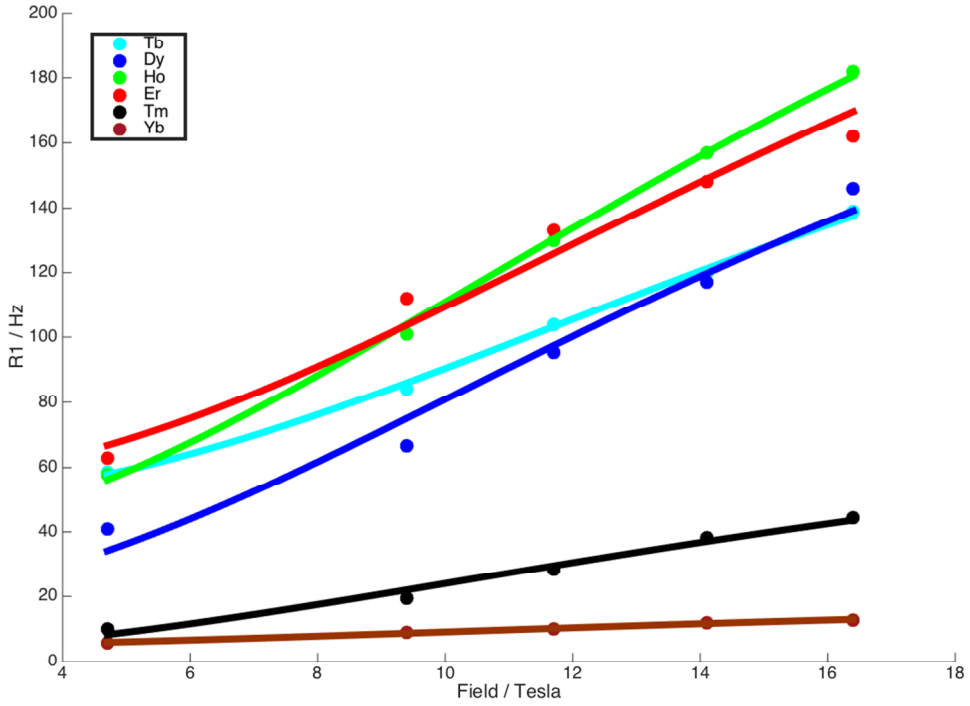

Figure 3-3: Global minimization of μ_{eff}, T_{1e}, d, and τ_R based on R_1 data at five field strengths for DOTA-F6 complexes.

Table 3-7: Global minimizations of μ_{eff}, T_{1e} as a function of relaxation rates for F-DOTPME complexes. Subsequent iterations yielded the reported values for τ_R and [d].

F-DOTPME: Metal	μ_{eff} (B. M.)	T_{1e} (ps)
Tb(III)	9.87	0.43
Dy(III)	10.6	0.59
Ho(III)	10.3	0.37
Er(III)	8.61	0.57
Tm(III)	7.37	0.16
Yb(III)	4.38	0.19
	τ_R	266 ps
	d	6.70 Å

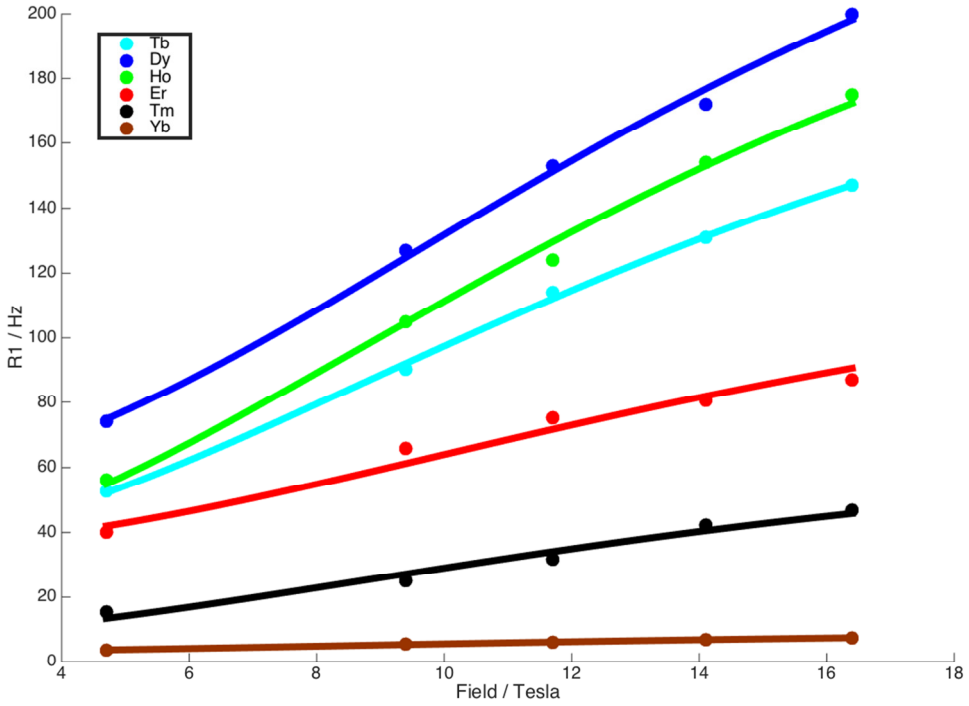

Figure 3-4: Global minimization of μ_{eff}, T_{1e}, d, and τ_R based on R_1 data at five field strengths for F-DOTPME complexes.

3.5.3 Analysis of Data Fitted to Classic BRW Theory

The first system analyzed was the DOTAm-F12 series of complexes. In addition to the five field strengths used for the tetraamide, these six complexes were also analyzed at low field in an additional collaborative effort between Prof. David Parker in Durham, England and Prof. Mauro Botta in Alessandra, Italy, as well as my adviser and myself. The data provided by Botta represents the low-field measurements plotted in figure 3-2 at 1.4 T (56.4 MHz for ^{19}F). The data fittings conducted with these additional low-field measurements further validated the BRW minimization for the DOTAm-F12 series, as trend lines plotted in Figure 3-2 indicate. The above minimizations for each system also were used to approximate values of τ_R and d, however these approximates are less accurate than the approximations of μ_{eff} and T_{1e}.

3.5.4 Approximation of τ_R and *d* from BRW Theory and Drawbacks of Global Minimization

The minimization techniques used to obtain the data above assume that isostructural series of metal complexes share the same value of *d* and τ_R across the entire series of lanthanides. This assumption disregards any component of lanthanide contraction across the series. This may only slightly change τ_R values, but *d* is not constant for these complexes due to lanthanide contraction.[140-142] These observations suggest that the global minimization method has significant limitations.

In all three of the preceding data fitting processes, the minimized data resulted in τ_R values that are much higher than expected. The tetraacid DOTA-F6 is very similar in structure to the unmodified DOTA ligand, for which the τ_R values have been found to be closer to 100 ps.[7,143,144] The slight structural modifications to the DOTA ligand, as in the case of DOTA-F6, as well as DOTAm-F12 and F-DOTPME (with approximated τ_R values from the global fitting of 205, 231, and 266 ps, respectively) suggest that these values obtained are far too high.

Likewise, the values obtained for the Ln(III)-^{19}F distance, *d*, are also in disagreement with the data obtained from X-ray crystallographic data and DFT calculations for DOTAm-F12, both described in Chapter 2. The Ln(III)-F distance found in both studies is ca. 6.2 Å, whereas the results of the minimization procedure indicate a distance of 5.9 Å. Classic BRW theory predicts R_1 having a d^3 dependency in the dipolar term, and in the Curie term—which is dominant at higher field strengths—a d^6 dependency. What may appear to be a small difference in *d* has a much more pronounced significance in the BRW theory governing ^{19}F relaxation rates, especially at higher field.

3.6 Other Methods Used to Determine τ_R and d

Determination of *d* was performed by X-ray crystallography of [Tm-DOTAm-F12]$^{3+}$ and gas- and solution-state DFT calculations performed by Dr. Kriti Srivastava and reported in Chapter 2. The results from both X-ray and DFT calculations result in *d* for [Tm-DOTAm-F12]$^{3+}$ of 6.26 Å.

3.6.1 Determination of τ_R Using NMRD and [Gd-DOTAm-F12]$^{3+}$

In collaboration with Prof. Mauro Botta, the nuclear magnetic relaxation dispersion (NMRD) profile of [Gd-DOTAM-F12]$^{3+}$ was obtained. NMRD is an indirect method of determining τ_R by measuring the relaxivity data of a Gd(III)-based metal complex as a function of field strength, often coupled with ^{17}O spectroscopy. The NMR instrumentation required has the ability to vary the Larmor frequency measured to provide data from extremely low field strengths iteratively to high field strengths. NMRD profiles for Gd(III) metal complexes often share the same behavior as demonstrated in Figure 3-5.

By examining the changes in relaxivities combined with ^{17}O spectroscopy, the τ_R value can be further refined. The NMRD data provided by Botta, shown in Figure 3-5, has yielded a number of constants for the DOTAm-F12 ligand, as shown in Table 3-8. The value for τ_R is not ultimately constant across the series of DOTAm-F12 metal complexes, but using the value of 89 ps obtained for the Gd(III) complex should be quite similar to the other metal complexes, as only the relative size of the other metal complexes is due to the decreasing size of the metal ion (lanthanide contraction).

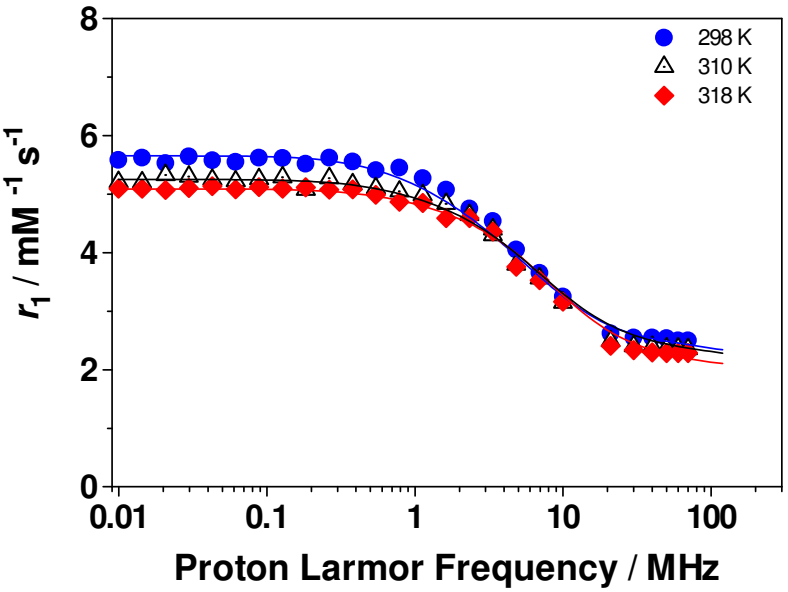

Figure 3-5: ^{1}H NMRD profiles (pH = 6.9) at different temperatures (298, 310 and 318 K). The curves are calculated with the parameters of table 3-8.

Table 3-8: Parameters obtained from the analysis of ^{17}O NMR and NMRD data[a] of [Gd-DOTAm-F12]$^{3+}$

Parameter	[GdL]$^{3+}$
$^{20}r_1^{298}$ (mM^{-1}s^{-1})	2.6
Δ^2 / 10^{19} s^{-2}	1.6
τ_V^{298} / ps	6.1
τ_M^{298} / μs	19
τ_R^{298} / ps	89
q	1[b]
r / Å	3.0[b]
E_V / kJ mol^{-1}	1.0[b]
$\Delta H^{\#}_M$ / kJ mol^{-1}	45
$A/\hbar$ / 10^6 rad s^{-1}	-3.8

[a]For the parameters a, ^{298}D, E_R and E_D the values of 4.3 Å, 2.24×10^{-5} cm^2 s^{-1}, 16 and -26 kJ mol^{-1}, respectively, were used; [b] fixed in the fitting procedure.

3.7 Minimization of Data Using Known Values of τ_R and *d*

The minimization procedure and iteration process was used to calculate the values of μ_{eff} and T_{1e} for the DOTAm-F12 complexes, having now definite values for *d* and τ_R from X-ray crystallographic data and NMRD profiling. Holding these values as constants for the model complex [Tm-DOTAm-F12]$^{3+}$ (from which the X-ray value of *d* was obtained) has resulted in fitting of the BRW theory to the observed relaxation rate data obtained across five field strengths, and is shown in Figure 3-6.

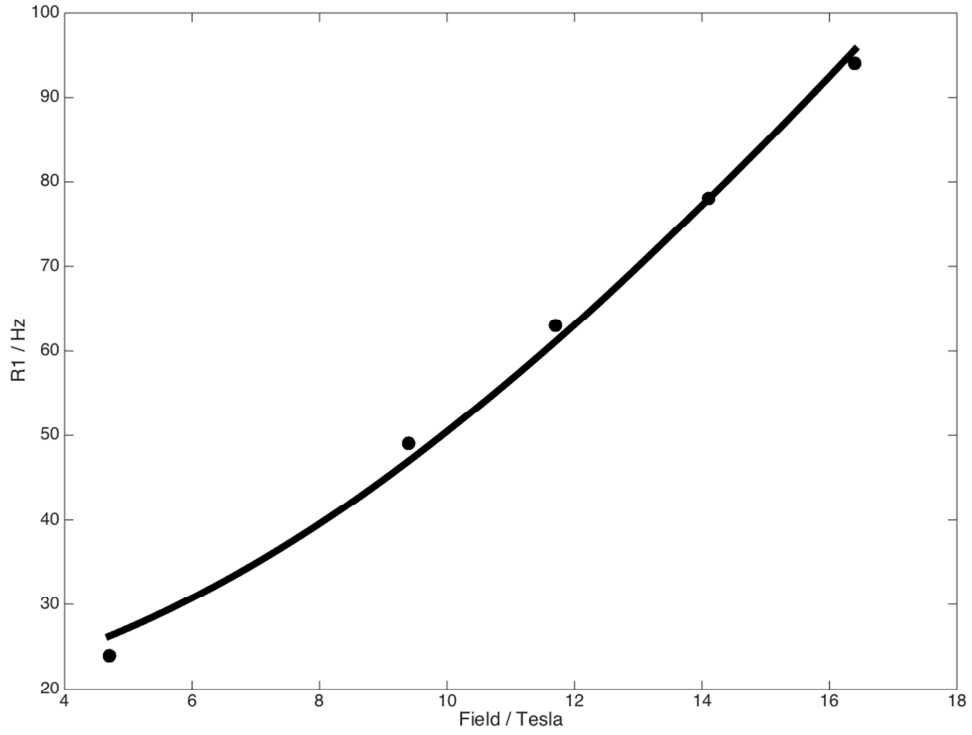

Figure 3-6: Minimization of [Tm-DOTAm-F12]$^{3+}$ using fixed *d* = 6.26 Å and τ_R = 89 ps. Minimization results in μ_{ef}f = 8.31 and T_{1e} = 0.19 ps.

3.7.1 Results

The minimization for [Tm-DOTAm-F12]$^{3+}$ has been fitted to the relaxation rate data points (Figure 3-6) with poorer agreement than that observed in Figure 3-2.

Specifically, the reconciliation of data points at 4.7 T and 9.3 T represent the poorest area of data fitting. This trend is also observed for the Tb(III), Dy(III), Ho(III), Er(III), and Yb(III) fittings (though these data assumed the same value of *d* as the Tm(III) complex, which is unlikely, as shown in Figure 3-7 and Table 3-9). The only resultant fit that matches the accuracy of the global fit with all variable terms is Yb(III), which, coincidentally, has the lowest μ_{eff} value of any of the preceding mentions, both provided as a literature standard of 4.5 when complexed with the non-fluorinated DOTAm ligand[126] and fitted for the DOTAm-F12 system of 4.56 (global, all vary) and 5.24 (global fit, fixed τ_R and *d*), meaning that the higher values of μ_{eff} found (>10 B. M. for Tb(III), Dy(III), Ho(III), and Er(III)) demonstrate most clearly the limitations of the global minimization approach.

Table 3-9: Global minimizations of μ_{eff} and T_{1e} as a function of relaxation rates for DOTAm-F12 complexes, using an all-vary global fit, and then using fixed values of τ_R = 89 ps and *d* = 6.26 Å in a global fit.

Ln(III)	μ_{eff} (B. M.) (global, all vary)	T_{1e} (ps) (global, all vary)		μ_{eff} (B. M.) (global, fixed τ_R and *d*)	T_{1e} (ps) (global, fixed τ_R and *d*)
Tb(III)	9.77	0.52		11.2	0.62
Dy(III)	10.4	0.36		12.0	0.48
Ho(III)	9.88	0.28		11.3	0.41
Er(III)	8.98	0.13		10.3	0.20
Tm(III)	7.31	0.12		8.31	0.19
Yb(III)	4.56	0.11		5.24	0.12
	τ_R	231 ps		τ_R	89 ps
	d	5.92 Å		*d*	6.26 Å

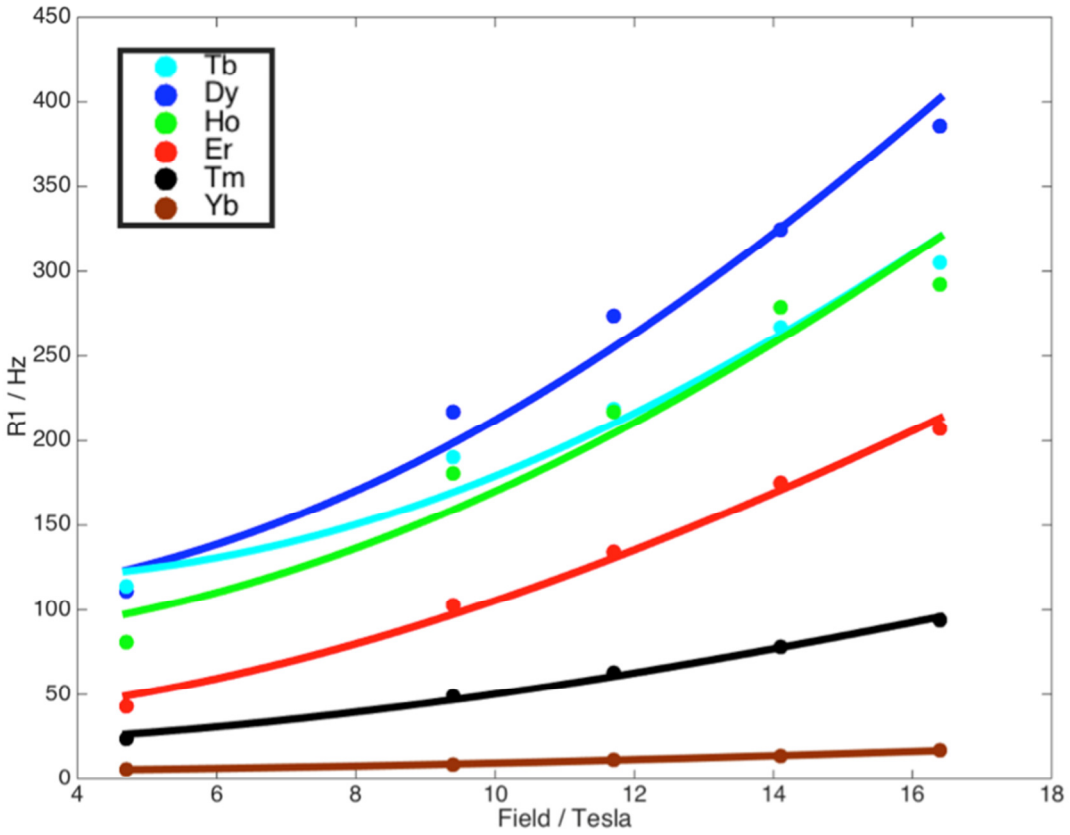

Figure 3-7: Minimization of Tb(III), Dy(III), Ho(III), Er(III), Tb(III), and Yb(III) using fixed d = 6.26 Å and τ_R = 89 ps.

3.7.2 Analysis of Each Approach

Fitting the relaxation rate data to BRW theory as outlined and performed in this chapter has reached its limits of valid approximations to some extent. Not only has this global fitting procedure not matched BRW theory, it also resulted in an incorrect value of d (which again, at lower field carries a d^3 and d^6 dependency, and at higher field is dicated by the Curie term of the BRW theory which carries solely a d^6 dependency), and it has also overestimated the τ_R value of each metal complex in the DOTAm-F12 series by over two-fold. If the same fitting operations are performed holding the values of d and τ_R constant to what has been determined with utmost certainty by X-ray crystallography and by NMRD profiling, respectively, the discrepancies between the

dipolar term and the Curie term of BRW theory clearly are not approximated effectively.

3.7.3 Additional Experiments to Determine μ_{eff} and *d*

The values of μ_{eff} and *d* can be determined using complementary procedures. These procedures have the potential to further weigh in on the values of μ_{eff} and *d*. The effective magnetic moment of each complex can be measured by Superconducting Quantum Interference Device (SQUID), as long as the concomitant measurement of metal concentration by ICP-MS has been performed. SQUID measurements or Evans' method NMR procedure, combined with ICP-MS to determine the magnetic component provided by the complex subtracting any residual salts formed in the complexation procedure, should yield the value of μ_{eff} with high accuracy.

Next, the values of *d* across the DOTAm-F12 series as well as the DOTA-F6 and F-DOTPME series can all be crystallized and analyzed by X-ray crystallography (though admittedly, this would be quite an undertaking). Further molecular modeling using DFT calculations in solution can be used to refine the X-ray crystallographic data or could be used in place of it.

While these options are open for further exploration, they have not been explored definitively at the time this document was written.

3.8 Conclusions and Future Work

The work presented in this chapter demonstrates how the relaxation rates of three different series of macrocyclic ^{19}F metal complexes behave at low and high field strength. The results reported can be taken into consideration when designing new ^{19}F probes for MRI.

The results obtained suggest that the relaxation rates of ^{19}F nuclei in probes of this kind can benefit from higher field strength devices, the strength of which is limited by R_2 values. With the demonstrated high T_2/T_1 ratio observed with Fe(II) complexes, the same ligands should be examined in this manner to possibly enhance further the resolution and sensitivity of ^{19}F MR data.

The minimization of data incorporated in the BRW theory developed by Kuprov may have limitations with regard to τ_R and d approximations, but otherwise appears to be accurate for the determination of the electron relaxation rate (T_{1e}) and the magnetic susceptibility (μ_{eff}). Since lanthanide contraction occurs across the series, the global fitting parameters could apply the contraction relative to one or more X-ray crystal structures or DFT calculations as a reference point.

With these design considerations in hand, new and responsive probes can be developed using functional groups of varying hardness and can be compared to those presented herein. While three types of ligands have been explored, many other designs are possible, including the use of alcohol donors similar to the commercial HP-DO3A Gd(III) contrast agent. These data can help predict the MR behavior of systems similar to those presented here.

3.9 Experimental Materials and Methods

General considerations. Starting materials were obtained from commercial suppliers and used without further purification. Water was distilled and further purified by a Millipore cartridge system (resistivity 1.8×10^7 Ω). All organic extracts were dried over anhydrous $MgSO_4$ and solvents were removed under reduced pressure with a rotary evaporator. All synthetic compounds were characterized at the LeClaire-Dow

Chemical Instrumentation Facility at the Department of Chemistry at the University of Minnesota, Twin-Cities. ^{1}H NMR spectra were recorded on a Varian 500 at 500 MHz, ^{13}C NMR spectra on a Bruker AV-500 at 125 MHz, and ^{19}F NMR spectra were recorded on a Varian VXR-300 at 282 MHz. The residual solvent peak was used as an internal reference for ^{1}H and ^{13}C NMR; $CFCl_3$ was used as an internal reference for ^{19}F NMR of organic intermediates; and KF was used as an external standard for metal complexes. Data for ^{1}H NMR are reported as follows: chemical shift (δ, ppm), multiplicity (s, singlet; br s, broad singlet; d, doublet; t, triplet; q, quartet; m, multiplet), integration, coupling constant (Hz). Data for ^{13}C NMR and ^{19}F NMR are reported in terms of chemical shift (δ, ppm). Longitudinal (T_1) and transverse (T_2) relaxation times of ^{19}F nuclei of metal complexes in D_2O were measured using the inversion recovery sequence and the Carr-Purcell-Meiboom-Gill sequence, respectively. A delay time of 30 ms and acquisition time of 64 ms were used for the collection of ^{1}H and ^{19}F NMR spectra of the paramagnetic M-DOTAm-F12 complexes. Mass spectra (HR, high resolution; ESI, electrospray ionization) were recorded on a Bruker BioTOF II at the Waters Center of Innovation for Mass Spectrometry at the Department of Chemistry at the University of Minnesota, Twin-Cities.

Diethyl 2,2'-(1,4,7,10-tetraazacyclododecane-1,7-diyl)bis(4,4,4-trifluorobutanoate) (3-3): Cyclen (1.38 g, 8.03 mmol) was dissolved in dry CH_3CN and magnetically stirred. K_2CO_3 (11.1 g, 80.3 mmol) was added, followed by 2-bromo-4,4,4-trifluorobutyric acid ethyl ester (3.31 mL, 20.1 mmol) and the reaction mixture was heated to 105 ˚C for 18 h. The reaction mixture was then filtered, and the filtrate

concentrated under reduced pressure to yield a yellow oil that was then deposited on to silica and purified via flash chromatography (eluent: 1-8% MeOH in CH_2Cl_2) to yield the pure product as a light yellow semi-oil that was further dried under high vacuum overnight (**3-3**, 2.45 g, 60.0 %). ^{1}H NMR (500 MHz, $CDCl_3$) δ 4.16-4.08 (m, 4 H), 3.77 (quintet, *J* = 8.0 Hz, 2 H), 2.79-2.57 (m, 22 H), 1.22 (t, *J* = 7.5 Hz, 6 H). ^{13}C NMR (125 MHz, $CDCl_3$) δ 170.3, 126.6 (q, *J* = 286 Hz), 61.1, 57.2 (q, *J* = 59.1 Hz), 48.7, 45.4, 32.1, 31.6, 13.9. ^{19}F NMR (470 MHz, $CDCl_3$) δ -63.6 (t, *J* = 10.8 Hz). HRMS-ESI (*m*/*z*) $[M + H]^+$ calc for $C_{20}H_{30}F_6N_4O_4$: 509.2557; found: 509.2560.

Diethyl 2,2'-(4,10-bis(2-(*tert*-butoxy)-2-oxoethyl)-1,4,7,10-tetraazacyclododecane-1,7-diyl)bis(4,4,4-trifluorobutanoate) (3-4): Compound **3-3** (1.29 g, 2.54 mmol) was dissolved in dry CH_3CN and magnetically stirred. K_2CO_3 (2.31 g, 16.8 mmol) was added, followed by tert-butyl bromoacetate (826 μL, 5.59 mmol) and the reaction mixture was heated to 45 ˚C for 16 h. The reaction mixture was then filtered, and the filtrate concentrated under reduced pressure to yield a yellow that was further dried under high vacuum overnight yielding a yellow oil that did not need further purification (**3-4**, 1.80 g, 96.0 %). ^{1}H NMR (500 MHz, $CDCl_3$) δ 4.15 (q, *J* = 7.0 Hz, 4 H), 3.76-3.73 (m, 2 H), 3.24 (s, 4 H), 2.84-2.64 (m, 20 H), 1.47 (s, 18 H), 1.26 (t, *J* = 7.0 Hz, 6 H). ^{13}C NMR (125 MHz, $CDCl_3$) δ 170.8, 170.4, 126.9 (q, *J* = 286 Hz), 80.7, 60.9, 59.5 (q, *J* = 58.3 Hz), 55.8, 52.9, 49.3, 32.6, 14.1. ^{19}F NMR (470 MHz, $CDCl_3$) δ -64.1 (t, *J* = 10.8 Hz). HRMS-ESI (*m*/*z*) $[M + H]^+$ calc for $C_{32}H_{54}F_6N_4O_8$: 737.3919; found: 737.3910.

Disodium 2,2'-(4,10-bis(2-(*tert*-butoxy)-2-oxoethyl)-1,4,7,10-tetraazacyclododecane-1,7-diyl)bis(4,4,4-trifluorobutanoate) (3-5): Compound **3-4** (1.21 g, 1.64 mmol) was dissolved in MeOH (10 mL) and magnetically stirred in an ice bath. Aqueous NaOH (6 M, 20 mL) was then added dropwise over 5 min., and the reaction mixture was allowed to warm to ambient temperature and stirred for 1 h. The aqueous phase was extracted with $CHCl_3$ (30 × 50 mL), and the combined organic phases were washed with brine, dried over $MgSO_4$, and concentrated under reduced pressure to yield a white crystalline solid that was further dried under high vacuum overnight (**3-5**, 1.15 g, 97.0 %). The solid was used immediately in the next step.

2,2'-(4,10-Bis(carboxymethyl)-1,4,7,10-tetraazacyclododecane-1,7-diyl)bis(4,4,4-trifluorobutanoic acid) tetrahydrochloride salt (DOTA-F6, 3-1): The disodium salt **3-5** was dissolved in water (100 mL) and magnetically stirred in an ice bath. Concentrated HCl (36 % w/v, 6.0 mL) was added dropwise over 5 min., and the reaction mixture was allowed to warm to ambient temperature and stirred for 1 h. The reaction mixture was then concentrated under reduced pressure to yield a sticky, white gum, that was immediately dissolved in H_2O (50 mL) and lyophilized to yield the tetraacid, tetrahydrochloride salt as a white solid (1.10 g, 93.9 % over two steps). ^{1}H NMR (500 MHz, D_2O) δ 4.37-4.08 (m, 4 H), 3.78-3.49 (m, 6 H), 3.32-2.77 (m, 16 H). ^{13}C NMR (125 MHz, D_2O) δ 174.1, 168.2, 122.2 (q, J = 285 Hz), 69.8, 55.8, 55.0, 54.0, 51.1, 44.4, 29.6, 27.1. ^{19}F NMR (470 MHz, D_2O) δ -75.7 (t, J = 10.8 Hz). HRMS-ESI (*m*/*z*) $[M + H]^+$ calc for $C_{20}H_{30}F_6N_4O_8$: 569.2041; found: 569.2031.

[La-DOTA-F6]$^-$ (3-5), representative procedure: Compound **DOTA-F6** (**3-1**) (100. mg, 0.140 mmol) was dissolved in mQ H_2O (25 mL) and magnetically stirred. An aqueous solution of $LaCl_3$ (0.100 M, 1.40 mL) was then added, and dilute aq. NaOH solution was added to the reaction mixture until pH = 7.5. The reaction mixture was then heated to 90 ˚C for 3.5 days and lyophilized to yield the complex **3-5** as a white crystalline solid (139 mg, >99.0 %). HRMS-ESI (*m*/*z*) $[M]^-$ calc for $C_{20}H_{30}F_6LaN_4O_8$: 707.1026; found: 707.1033.

[Eu-DOTA-F6]$^-$ (3-6): White solid, using $EuCl_3$ (140 mg, >97.0 %). HRMS-ESI (*m*/*z*) $[M]^-$ calc for $C_{20}H_{30}EuF_6N_4O_8$: 721.1175; found: 721.1170. The observed isotopic distribution matched the calculated one.

[Gd-DOTA-F6]$^-$ (3-7): White solid, using $GdCl_3$ (142 mg, >98.0 %). HRMS-ESI (*m*/*z*) $[M]^-$ calc for $C_{20}H_{30}F_6GdN_4O_8$: 726.1203; found: 726.1201. The observed isotopic distribution matched the calculated one.

[Tb-DOTA-F6]$^-$ (3-8): White solid, using $TbCl_3$ (143 mg, >98.5 %). HRMS-ESI (*m*/*z*) $[M]^-$ calc for $C_{20}H_{30}F_6N_4O_8Tb$: 727.1216; found: 727.1226.

[Dy-DOTA-F6]$^-$ (3-9): Brown solid, using DyI_3. (143 mg, >98.0 %). HRMS-ESI (*m*/*z*) $[M]^-$ calc for $C_{20}H_{30}DyF_6N_4O_8$: 732.1254; found: 732.1254. The observed isotopic distribution matched the calculated one.

[Ho-DOTA-F6]$^-$ (3-10): Pink solid, using $HoBr_3$ (144 mg, >97.0 %). HRMS-ESI (*m*/*z*) $[M]^-$ calc for $C_{20}H_{30}F_6HoN_4O_8$: 733.1266; found: 733.1279.

[Er-DOTA-F6]$^-$ (3-11): Brown solid, using ErI_3 (146 mg, >98.0 %). HRMS-ESI (*m*/*z*) $[M]^-$ calc for $C_{20}H_{30}ErF_6N_4O_8$: 734.1265; found: 734.1251. The observed isotopic distribution matched the calculated one.

[Tm-DOTA-F6]$^-$ (3-12): White solid, using $TmCl_3$ (147 mg, >98.0 %). HRMS-ESI (*m*/*z*) $[M]^-$ calc for $C_{20}H_{30}F_6N_4O_8Tm$: 737.1304; found: 737.1295.

[Yb-DOTA-F6]$^-$ (3-13): White solid, using $YbCl_3$ (146 mg, >98.0 %). HRMS-ESI (*m*/*z*) $[M]^-$ calc for $C_{20}H_{30}F_6N_4O_8Yb$: 742.1351; found: 742.1350. The observed isotopic distribution matched the calculated one.

1,4,7,10-tetraazacyclododecane-1,4,7,10-tetrakis(methanephosphonic acid di(2',2',2'-trifluoroethyl) ester) [F-DOTPME] (3-14). Cyclen (2.66 g, 15.4 mmol) was suspended in benzene (15 mL) and magnetically stirred. Glacial acetic acid (5 mL) was added, followed by paraformaldehyde (3.20 g, 110 mmol). Bis(2,2,2-trifluoroethyl)phosphite (13.0 g, 52.8 mmol) diluted in benzene (15 mL), was then added, and the reaction was stirred at 25 ºC for 72 h. Volatiles were removed under reduced pressure to yield an off-white gum which was washed with benzene (2 × 30 mL) and dried under high vacuum overnight yielding a hygroscopic white solid. This solid was dissolved in diethyl ether (50 mL) with stirring and water (30 mL) was added,

and the acidic mixture was neutralized with solid sodium bicarbonate. The organic layer was separated and the aqueous layer further extracted with diethyl ether (6 × 30 mL). The organic phases were combined and dried over $MgSO_4$, filtered, and concentrated under reduced pressure to yield the perester **3-15** as a white solid. Aqueous NaOH (5 M, 50 mL) was added to the solid, and the resultant suspension was heated at reflux for 30 min and further stirred at ambient temperature for 2 days. Additional aqueous NaOH (12 M, 50 mL) was added to the solution, refluxed for 1 h, and cooled to ambient temperature precipitating a white solid that was filtered off and collected. This step was repeated three more times, yielding F-DOTPME **(3-14)** as the tetrasodium salt (2.7 g, 2.8 mmol, 18%). ^{1}H NMR (300 MHz, D_2O) δ = 2.59 (s, 8 H), 2.77 (d, *J* = 9.6 Hz, 16 H), 4.13 (quintet, *J* = 8.1 Hz, 8 H). ^{19}F NMR (282 MHz, D_2O) δ = -75.8. ^{31}P NMR (121 MHz, D_2O) δ = 23.3. HRMS-ESI (*m/z*) $[M + 2Na]^{2-}$ calc. for $C_{20}H_{32}F_{12}N_4O_{12}P_4$ 459.0, found: 459.0.

[La-F-DOTPME]$^-$ (3-16), representative procedure. Ligand **3-14** (220 mg, 0.233 mmol) was dissolved in mQ water (15 mL). The solution was adjusted to pH = 7.5 with aq. HCl, and aq. thulium(III) chloride (0.291 M, 726 μL) was added. The pH was again adjusted to 7.5 with aq. NaOH. The reaction was stirred at 75 ºC for 72 h, then was lyophilized, yielding a white crystalline solid (278 mg, quant.). HRMS-ESI (*m/z*) calc. for $C_{20}H_{32}F_{12}LaN_4O_{12}P_4$ $[M]^-$: 1010.9839, found: 1010.9861.

[Eu-F-DOTPME]$^-$ (3-17): White solid, using $EuCl_3$ (129 mg, >99.0 %). HRMS-ESI (*m*/*z*) [M]$^-$ calc for $C_{20}H_{32}EuF_{12}N_4O_{12}P_4$: 1024.9988; found: 1025.0001. The observed isotopic distribution matched the calculated one.

[Gd-F-DOTPME]$^-$ (3-18): White solid, using $GdCl_3$ (128 mg, >98.0 %). HRMS-ESI (*m*/*z*) [M]$^-$ calc for $C_{20}H_{32}F_{12}GdN_4O_{12}P_4$: 1030.0017; found: 1030.0004. The observed isotopic distribution matched the calculated one.

[Tb-F-DOTPME]$^-$ (3-19): White solid, using $TbCl_3$ (129 mg, >99.0 %). HRMS-ESI (*m*/*z*) [M]$^-$ calc for $C_{20}H_{32}F_{12}N_4O_{12}P_4Tb$: 1031.0029; found: 1031.0025.

[Dy-F-DOTPME]$^-$ (3-20): Yellow solid, using DyI_3. (128 mg, >98.0 %). HRMS-ESI (*m*/*z*) [M]$^-$ calc for $C_{20}H_{32}DyF_{12}N_4O_{12}P_4$: 1036.0067; found: 732.1254. The observed isotopic distribution matched the calculated one.

[Ho-F-DOTPME]$^-$ (3-21): Pink solid, using $HoBr_3$ (130 mg, >99.0 %). HRMS-ESI (*m*/*z*) [M]$^-$ calc for $C_{20}H_{32}F_{12}HoN_4O_{12}P_4$: 1037.0079; found: 1037.0031.

[Er-F-DOTPME]$^-$ (3-22): Brown solid, using ErI_3 (130 mg, >98.0 %). HRMS-ESI (*m*/*z*) [M]$^-$ calc for $C_{20}H_{32}ErF_{12}N_4O_{12}P_4$: 1038.0078; found: 1038.0041. The observed isotopic distribution matched the calculated one.

[Tm-F-DOTPME]$^-$ (3-23): White solid, using $TmCl_3$ (131 mg, >99.0 %). HRMS-ESI (*m*/*z*) $[M]^-$ calc for $C_{20}H_{32}F_{12}N_4O_{12}P_4Tm$: 1041.0118; found: 1041.0110.

[Yb-F-DOTPME]$^-$ (3-24): White solid, using $YbCl_3$ (128 mg, >96.0 %). HRMS-ESI (*m*/*z*) $[M]^-$ calc for $C_{20}H_{32}F_{12}N_4O_{12}P_4Tm$: 1046.0164; found: 1046.0155. The observed isotopic distribution matched the calculated one.

4 A Responsive ^{19}F MRI Contrast Agent for Detection of Cu(I)

4.1 Introduction

In the last decade, responsive MRI contrast agents have increasingly become the subjects of studies, with targets as varied as cations, sugars, proteins, enzymes, nucleic acids and viruses. However, to date, neither gadolinium nor particulate responsive contrast agents are frequently used for *in vivo* studies. The fundamental problem with these probes is that the response observed, that is the change in the relaxation time (T_1 for gadolinium and T_2 for particulate contrast agents), depends on two parameters: the concentration of the targeted marker and that of the contrast agent. A single image, however, cannot differentiate these two parameters. Thus, *in vivo* images acquired using these responsive contrast agents are often inconclusive in the determination of the distribution of their targeted analytes.

The design considerations of a ^{19}F MRI contrast agent that is both responsive and ratiometric require a response mechanism that is selective for a single analyte, and the presence of at least two unique fluorine signals, one of which changes with response to the analyte, and another that does not.

This problem can in theory be solved with the use of ratiometric responsive contrast agents. Of those, PARACEST agents[145-151] and ^{1}H and ^{19}F chemical shift probes, have shown much promise, particularly by magnetic resonance spectroscopy (MRS). In the latter case, groundbreaking work by Mason,[34,152-166] Ahrens[66,167-177] and others demonstrated that the change in chemical shift induced by reaction with or upon reversible binding to an analyte can induce a shift significant enough to be observed by MRS in cells or tissues; although they are rarely large enough to enable three dimensional imaging by MRI. In terms of shift reagents, ^{19}F is preferred over ^{1}H due

to the large chemical shift range of this nucleus which facilitates monitoring of multiple fluorines, thereby raising the enticing possibility of multichromic MRI and the development of ratiometric probes.[178,179]

Developed for this project is a proof-of-principle demonstration of a ratiometric, responsive MRI contrast agent that responds catalytically to Cu(I). In particular, the designed probe does not respond to Cu(II) nor to other metal ions. This biomarker was chosen for this study due to its relevance to *in vivo* pathology: Cu(I) is improperly sequestered in amyloid-beta (Aβ) plaques in the brain of patients with Alzheimer's Disease (AD).[180-186]

4.2 Challenges of Copper Detection

Several innate properties of this Cu (I) ion have made it particularly difficult to image. Copper's redox ability can allow rapid interconversion between Cu(I) and Cu(II), presenting a challenge for imaging agents in that they must selectively respond to either Cu(I) or Cu(II). The intracellular reducing environment renders the copper as Cu(I), but in amyloid-beta plaques the reduction/oxidation potential is not known. Endogenous proteins, such as glutathione (GSH) and metallothionein, actively sequester, exchange, and transport copper throughout the body, limiting free copper to less than 1.6 μM in serum.[187] On the other hand, bound copper concentrations can be as high as 100 μM[188] in the brain and 400 μM in Aβ plaques. [189,190]

4.3 Tm-DOTA-Click

In order to address the demands of low fluorine sensitivity in ^{19}F MRI probes, as well as having a ratiometric response generated by two unique fluorines to be imaged,

a new probe, Tm-DOTA-Click, was synthesized containing a Tm(III) metal center, two different fluorines, a response mechanism to detect Cu(I), while retaining high water solubility. Tm-DOTA-click contains a DOTA tetraamide ligand for the Tm(III) center, and contains two different types of ^{19}F nuclei: four aromatic fluorines positioned away from the metal center in the unreacted state, and six aliphatic ones which are substantially closer to the paramagnetic ion. The reactive functionality pair of a terminal acetylene and an organic azide allows for the copper(I)-catalyzed Huisgen cycloaddition that clicks the terminal azide and acetylene groups together, thereby locking the probe in a substantially different conformation. This conformational change alters both the chemical shifts and the relaxation times of both fluorine signals.

Intermolecular reactions and the formation of oligomers, however is possible, especially at higher concentrations of the probe. Advantageously, whether the reaction occurs in an intra- or inter-molecular fashion has little bearing on the observed results, since the resultant configuration of the probe's fluorines either in the monomeric or oligomeric forms of the probe add similar steric bulk to the aliphatic fluorines, causing a ^{19}FLIS of those resonances. Either form as well would position the aryl fluorines much closer to the Tm(III) center, producing the same ^{19}FLIS and ^{19}FPRE response from either the monomeric or oligomeric forms of Tm-DOTA-click. The similarity in response between either the monomeric or polymeric forms of the reacted probe cause the same changes in the Tm(III)-^{19}F distances for the aryl fluorines, and the same changes in the position the aliphatic fluorines relative to the principal magnetic axis of the paramagnetic Tm(III) center. As a result, either the reacted monomer or reacted

oligomer would render identical MRI/MRS data both with respect to the aryl fluorines as well as the aliphatic fluorines.

Reported in Chapters 2 and 3, it was demonstrated that M-DOTAm-F12 complexes, which are readily soluble in water at concentrations as high as 100 mM, give excellent signal-to-noise ratios (SNR's) in blood (up to 23 for 1 mM mixture) given acquisition parameters suitable for *in vivo* imaging (2 min scan times for 0.5 mm resolution). Note that the contrast of responsive probes is defined as the difference in signal intensity of the probe in the presence of the analyte divided by that in the absence of the latter. Thus, a DOTA tetraamide ligand was central to the probe design. The two different fluorines were installed on the probe, and the probe's two configurations both before and after reaction with Cu(I) are indicated in Scheme 4-1

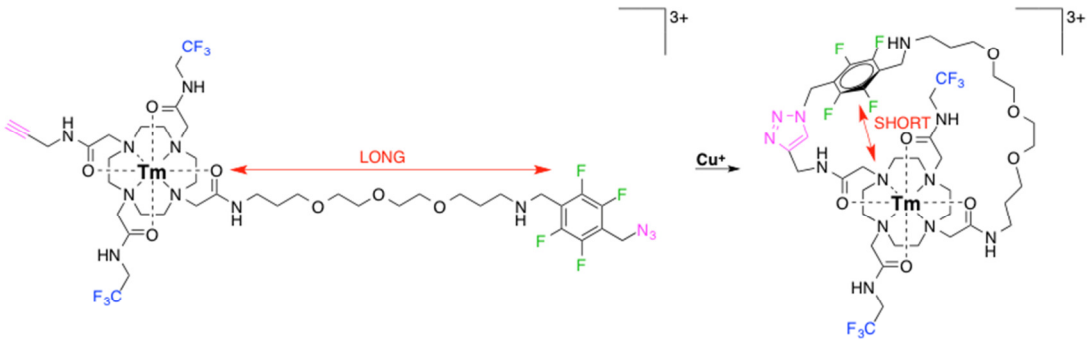

Scheme 4-1: Chemical structure and proposed mode of action of the ratiometric fluorine responsive contrast agent for Cu(I), Tm-DOTA-click (4-1). Copper(I)-catalyzed cycloaddition clicks the terminal azide and acetylene groups together, inducing a conformational change that affects the chemical shift and longitudinal relaxation times of both the aliphatic (blue) and the aromatic (green) fluorines. The reactive functionality pair are indicated in purple

In order to evaluate the different parameters that can be exploited to render paramagnetic fluorine complexes responsive, the lanthanide metal chosen for the

complex was thulium, creating a complex was designed and synthesized, Tm-DOTA-click, depicted in Figure **4-1**, which catalytically reports on the presence of Cu(I).

4.4 Synthesis of Tm-DOTA-Click

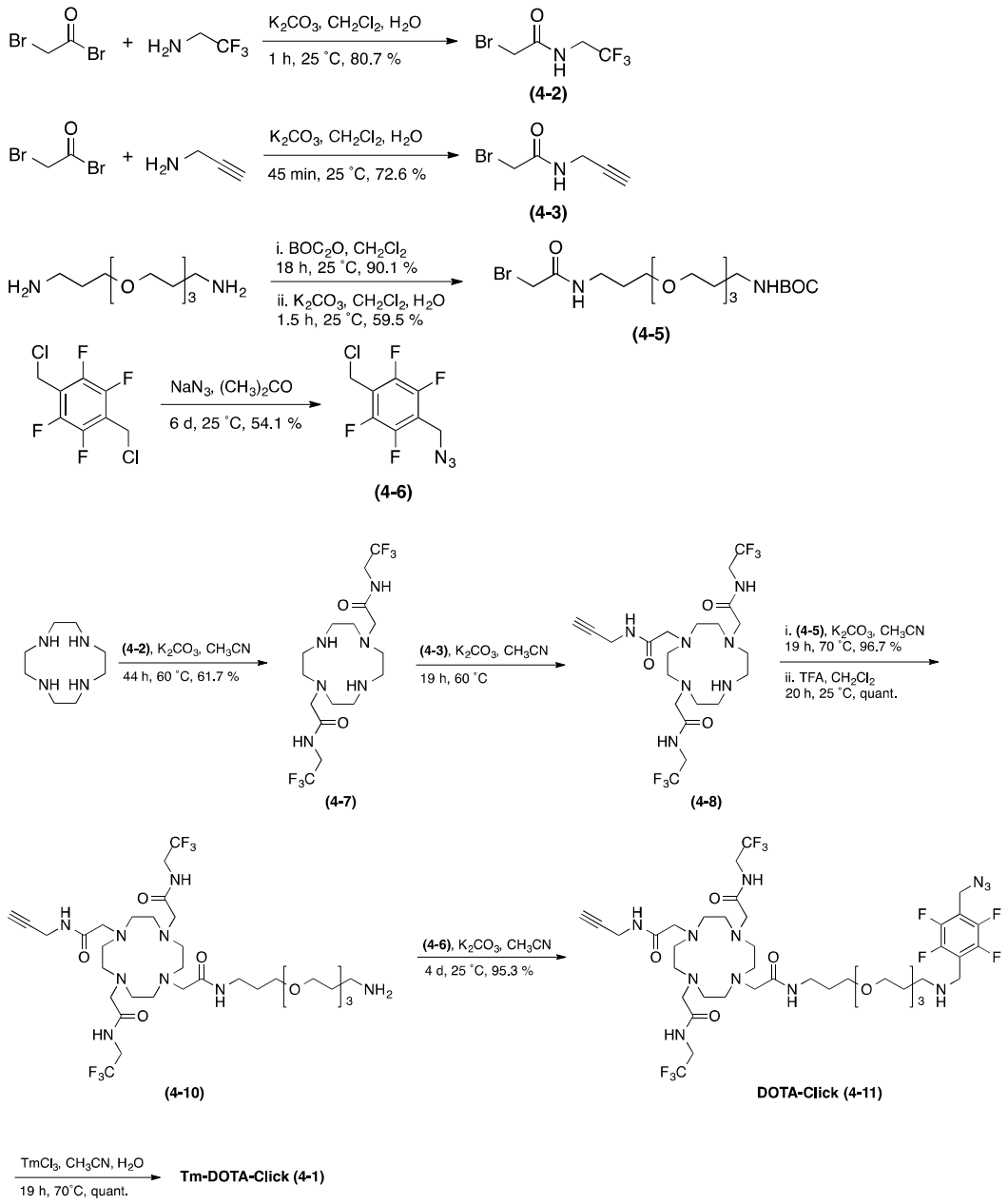

Scheme 4-2: Synthesis of Tm-DOTA-click (4-1); Reagents & conditions are as indicated.

Tm-DOTA-click (**1**) was synthesized over eleven steps, illustrated in Scheme 4-2. Mild alkylation conditions allowed for regioselective substitution at the 1- and 7-secondary nitrogens of cyclen with the aliphatic, CF_3 fluorine label. The third position was then alkylated with the propargylic group, and then the fourth with the BOC-protected PEG spacer. Deprotection with TFA afforded the free amine distant from the chelate which was coupled to the complementary aryl fluorine label with the azide, previously synthesized from the bis-chloromethyl starting material. The final complex was obtained by refluxing the ligand with one equivalent of $TmCl_3$ at neutral pH.

4.5 Analysis of MR Properties for Tm-DOTA-Click

4.5.1 ^{19}F Lanthanide-Induced Shift (^{19}FLIS)

For lanthanide-based responsive fluorine MR probe, the lanthanide-induced shift of a fluorine signal, defined as ^{19}FLIS, is the difference between the chemical shift of a ^{19}F in the presence and absence of the probe's analyte ($^{19}FLIS = \Delta\delta = \delta_{probe + analyte} - \delta_{probe}$).[82] This shift is the sum of the contributions from the contact shift, δ^c, and the pseudocontact shift, δ^{pc}. [191,192] Since for steric reasons the fluorines cannot come closer than 5 Å to the lanthanide, the contribution from the contact shift is negligible, and the observed ^{19}FLIS is primarily the result of the pseudocontact shift. Given this simplification, ^{19}FLIS follows the McConnell–Robertson equation; it is inversely proportional to the cube of the distance separating the lanthanide from the ^{19}F nuclei and follows a cosine relationship with the angle θ separating the lanthanide-fluorine vector and the principle magnetic dipolar axis of the complex. [191,193]

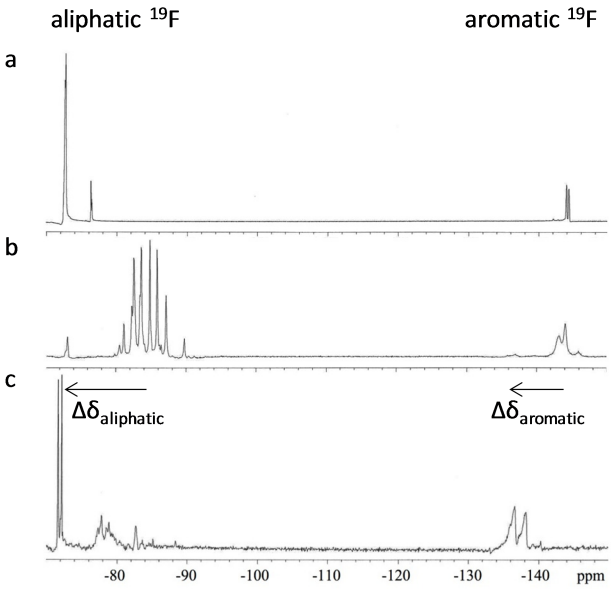

Figure 4-1: **N**MR spectra of a) the free ligand DOTA-click (**3-11**), b) Tm-DOTA-click (**3-1**) in the absence of Cu(I), and c) Tm-DOTA-click (**1**) after addition of 0.10 eq. Cu(I)Asc. Note that it is necessary to maintain a long delay time in order to fully observe the aromatic ^{19}F nuclei of the probe in the absence of Cu(I). Experimental conditions: [Tm-DOTA-click] = 1 mM, water pH 7, B_0 = 11.7 T, pulse-acquire, T_R = 20 m.

Table 4-1: Chemical shift, δ, and longitudinal, T_1, and transverse, T_2, relaxation times of the signals of the aliphatic and aryl fluorine nuclei of Tm-DOTA-click (1) before and after reaction with Cu(I). Numbers in parentheses represent standard deviations, n = 3

	- Cu(I)	+ Cu(I)
aliphatic ^{19}F		
δ (ppm)	-80 – -90	-71 – -80
T_1 (ms)	23 (1)	23 (1)
T_2 (ms)	11 (1)	9 (1)
aryl ^{19}F		
δ (ppm)	-142 – -146	-135 – -138
T_1 (ms)	241 (5)	18 (1)
T_2 (ms)	40 (3)	17 (1)

The copper-catalyzed cycloaddition thus affects the chemical shift of both the aliphatic and the aryl fluorines, albeit in a different manner. The aryl ^{19}F are brought within close proximity of the thulium, which, as expected, results in a strong downfield shift in their signal by 12 ppm (Table 4-1, Figure 4-1)

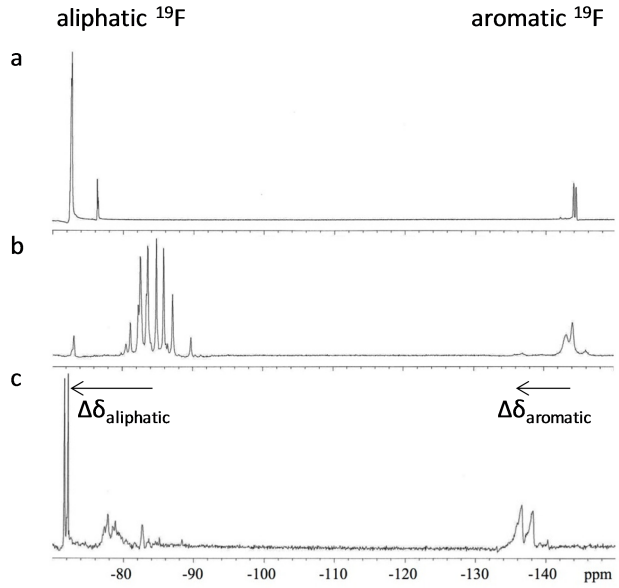

Figure 4-1: **N**MR spectra of a) the free ligand DOTA-click (**3-11**), b) Tm-DOTA-click (**3-1**) in the absence of Cu(I), and c) Tm-DOTA-click (**1**) after addition of 0.10 eq. Cu(I)Asc. Note that it is necessary to maintain a long delay time in order to fully observe the aromatic ^{19}F nuclei of the probe in the absence of Cu(I). Experimental conditions: [Tm-DOTA-click] = 1 mM, water pH 7, B_0 = 11.7 T, pulse-acquire, T_R = 20 m.

The steric hindrance caused by the capping aryl fluorines also changes the conformation of the thulium macrocycle in such a way that its aliphatic fluorines are pushed further away from the principal magnetic dipolar axis. As a result, the angle θ is altered causing the aliphatic ^{19}F signals to also shift by ~15 ppm. Although more difficult to predict than a change in Ln-^{19}F distance, an analyte-induced conformational change of a lanthanide complex that the angle θ can yield an equal or greater signal shift than one varying d. Note that the greater the chemical shift

difference between fluorine groups, the easier it is to image each fluorine group independently in three dimensions.

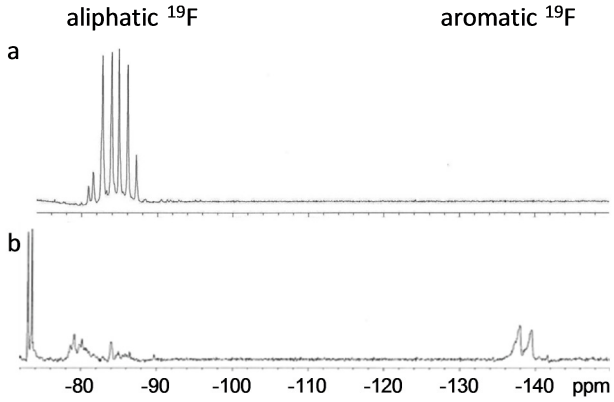

Figure 4-2: MR spectra of Tm-DOTA-click in water a) in the absence of Cu(I) and b) after addition of 0.10 eq. Cu(I)Asc obtained with the 19FLIRE sequence. The aromatic ^{19}Fs of the probe in the absence of Cu(I) disappear due to the addition of an inversion time equal to $ln(2)\times T_{1\,(\text{aromatic F})}$ in the pulse sequence. Without this inversion time, the NMR spectrum in a would be identical to that of Figure 3b. The signal of the aromatic fluorines only reappear after reaction with Cu(I) due to a change in the conformation of the probe that shortens their T_1. Experimental conditions: [Tm-DOTA-click] = 1 mM, B_0 = 11.7 T

The ^{19}FLIS response of both the aliphatic and aryl fluorines can be imaged in three dimensions by MRI, thereby giving two unique signals for ratiometric imaging. As illustrated in Figure 4-2 since the four fluorine signals - aliphatic and aryl before and after reaction with Cu(I) - are more than 10 ppm apart from each other, each can be imaged in three dimensions independently. Images of the aliphatic ^{19}F nuclei of unreacted Tm-DOTA-click were acquired by centering the excitation pulse at -95 ppm and can be seen in Figure 4-3b. Any signal observed in this image indicates where the probe is present but copper(I) is absent. On the other hand, applying a pulse at -60 ppm allows the observation of only the aliphatic ^{19}F nuclei of the reacted probe, that is, regions where both the probe and copper were present, which can be seen in Figure 4-3c.

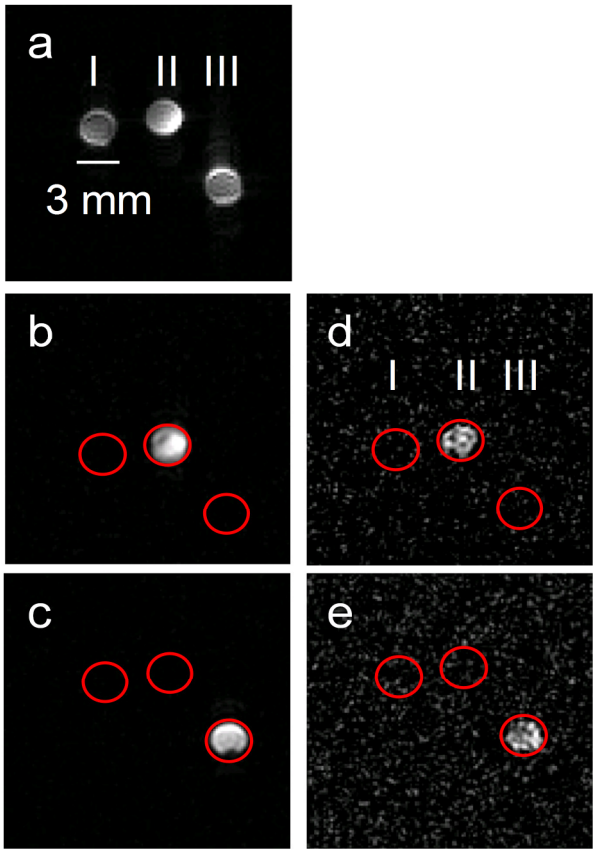

Figure 4-3: Ratiometric response of Tm-DOTA-click to Cu(I). I) water, II) Tm-DOTA-click (1) in water, III) Tm-DOTA-click (1) + 0.10 eq. Cu(I)Asc in water. a) T1-weighted 1H gradient echo image; 19F gradient echo images at b) -95 ppm and d) -145 ppm indicate indicate location of unreacted probe in the absence of Cu(I); ^{19}F gradient echo images at c) -60 ppm and e) -127 ppm indicate location of reacted probe in the presence of Cu(I). Experimental conditions: [Tm-DOTA-click] = 1 mM, B_0 = 16.4 T, na = (c) 512, (b, d, e) = 2048.

Moreover, an absence of probe can readily be detected by an absence of any signal at both -60 ppm and -95 ppm, as in Figure 4-2, tube I. Note that similar results are obtained if one focuses instead on the aryl fluorines' signal in the absence (-145 ppm, Figure 4-3d) and presence (-127 ppm) of copper (Figure 4-3e). This technique of multichromic MRI with a ratiometric response has a notable advantage: the two parameters that affect contrast – the concentration of the probe and the presence of an analyte – can be distinguished by collecting two independent images

4.5.2 ^{19}F Paramagnetic Relaxation Enhancement (^{19}FPRE) Response

The effect of the paramagnetic lanthanide ion on the longitudinal (T_1) and transverse (T_2) relaxation rates of the fluorines follows the Bloch-Redfield-Wangsness theory and a much steeper d^6 dependence on the Ln-^{19}F distance than ^{19}FLIS, but is independent of the angle θ between the fluorine-lanthanide vector and the principal

magnetic dipolar axis of the lanthanide ion.[194-196] As such, since the mean distance of the aliphatic ^{19}F nuclei to the Tm(III) center of the probe does not vary upon reaction with Cu(I), neither does their T_1 and T_2.

In a ^{19}FLIRE experiment, these aliphatic fluorines act as an internal standard, indicating the location and concentration of the probe. The distance separating the aryl fluorines from the lanthanide ion, however, changes substantially. As the probe reacts and the aryl ^{19}F's are brought closer to Tm, their T_1 and T_2 values decrease by 13-fold and 2-fold, respectively.

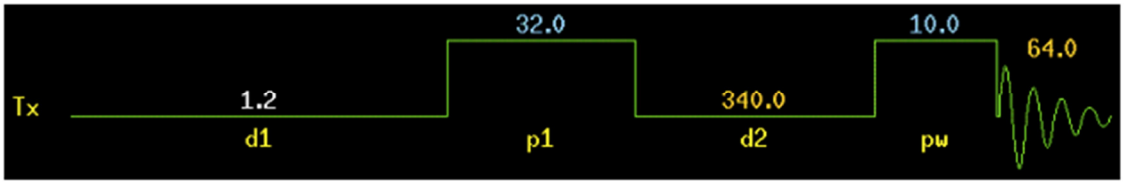

Figure 4-4: Pulse sequence used for ^{19}FLIRE-based signal silencing. Recycle delay (d1) = 1.2 s, 180° pulse (p180) = 32 ns, T_1(long) delay time (d2) = 340 ms, 90° pulse (pw) = 10 ns, acquisition time (at) = 64 ms.

This substantial change in T_1 can be readily utilized by MR spectroscopy to differentiate the unreacted form of the probe with the reacted form. Resonance suppression from ^{19}FLIRE silenced the aromatic ^{19}F nuclei of the unreacted form of Tm-DOTA-Click according to the pulse sequence in Figure 4-4.

The pulse sequence used and as depicted in Figure 4-4 Includes a recycle delay (**d1**) time of $5 \times T_{1(long)}$ (1.21 s) to allow all spins to relax between scans, a **p180** pulse (**p1**), and **d2** which are set to ln (2) $\times$ $T_{1(long)}$ (340 ms, the time required for the slow relaxing nuclei to show no magnetization in the Z-direction and completely in the XY plane), after which the **pw90** is applied and the acquisition is taken. With no Z-component at the time of the **pw90**, the aromatic nuclei with $T_{1(long)}$ are then not observed. Using the same pulse sequence but with reacted Tm-DOTA-Click with

Cu(I), both signals were observed, allowing for the exploitation of the ^{19}FLIRE, shortening T_1(long) to 19 ms, providing an $T_{1(short)}$ value that is not observable using the aforementioned pulse sequence. Tm-DOTA-Cick was then explored by MRI phantom imaging in concentrations reasonable for MR field strength strengths.

With such a sequence, the signal corresponding to the fluorine with the longest T_1 – the aryl fluorine in the absence of copper – is completely removed, as seen in Figure 4-6a. Without this inversion, the probe's spectrum is identical to that of Figure 3b. The aryl fluorines are thus only observed when copper is present, whereas the signal of alkyl fluorines is always observed, regardless of the presence of the probe's analyte. A ratiometric response is therefore maintained. Note that in three-dimensional MR imaging, similar results, albeit ones that are not fully on/off, can be obtained with a standard T_1-weighted gradient echo pulse sequence with a short repetition time.

4.5.3 Sensitivity

As with any ^{19}F MRI contrast agent, an important consideration is its sensitivity. The aliphatic fluorines of Tm-DOTA-Click are the same type of fluorines used in the DOTAm-F12 ligand and its complexes, except in Tm-DOTA-Click there are only two fluorine pendant arms rather than four, found in DOTAm-F12. While this difference does result in a loss of signal intensity, and the larger molecular weight of the compound renders the percentage of fluorine labeling much lower than DOTAm-F12, the aliphatic fluorines of Tm-DOTA-Click were found to be easily imaged in water by MRI and in a reasonable amount of time and with high SNR values, as seen in Figure 4-3 b,c.

Finally, the enhanced SNR of the aliphatic fluorines (Figure 4-3b-c) over the aromatic fluorines (Figure 4-3, d-e) result in a probe wherein the aliptatic signals are shifted between the reacted and unreacted forms of Tm-DOTA-Click. This change is provided in this probe by the aromatic ring changing the sterics of the aliphatic fluorines by increased steric bulk. In theory then, other reactive groups which increases the steric bulk (in the case of Tm-DOTA-Click, the aromatic ring) could be used to generate second-generation probes that operate in the same was as Tm-DOTA-Click.

4.5.4 Demonstration of Effective and Sensitive Response to Cu(I)

^{19}F NMR analysis was used in order to determine that the probe Tm-DOTA-Click reacts efficiently and catalytically with Cu(I). Various concentrations of Tm-DOTA-Click and Cu(I)-ascorbate (at catalytic levels) were incubated for 2 h at 37 ˚C. The resonances at -144 ppm and -136 ppm were used exclusively to monitor the percent conversion from the unreacted to the reacted state.

The results are summarized in Table 4-2. Tm-DOTA-Click is effectively and completely reacted at Cu(I) concentrations of 0.1% [Cu(I)] and higher. Given the short reaction time of 2 hours and the high concentrations of Tm-DOTA-Click in solution rather than biological media, show that Tm-DOTA-Click is quite sensitive to Cu(I), with an estimated limit of detection (LOD) at less than 10 μM. Additionally, to detect the presence of improperly sequestered Cu(I) in brain tissue of those with AD, the biological concentrations used with full catalytic conversion are observed.[183,184,186] However, this cannot be concluded with certainty that Tm-DOTA-click would

properly be catalyzed by Cu(I) in the brain, since neither its biodistribution nor its blood-brain-barrier (BBB) transmission *in vivo* has been determined.

Table 4-2: Percentage of Tm-DOTA-Click catalyzed by Cu(I) when incubated in D_2O for 2 h. The concentration of Cu(I) relative to the concentration of Tm-DOTA-Click is presented, as well as its net concentration. Mixtures of 0.1% Cu(I) or higher effectively catalyze all of the probe in the sample after 2 h incubation period.

[Tm-DOTA-Click]	[Cu(I)] relative to [Tm-DOTA-Click]	Actual [Cu(I)]	% Catalyzed (2 h)
50 µM	0.05 %	25 nM	65%
50 µM	0.10 %	50 nM	92%
250 µM	0.10 %	250 nM	**100%**
250 µM	0.25 %	625 nM	**100%**
250 µM	0.50 %	1.25 µM	**100%**
1 mM	0.10 %	1.0 µM	**100%**
1 mM	0.25 %	2.5 µM	**100%**
1 mM	0.50 %	5.0 µM	**100%**
1 mM	1.0 %	10 µM	**100%**

The probe Tm-DOTA-Click is a promising representation of a ratiometric and responsive ^{19}F MRI contrast agent with demonstrated ability to be imaged in three dimensions by ^{19}F MRI. Likewise, it provides evidence that other ratiometric probes can be developed and imaged using many of the principles that make Tm-DOTA-Click effective. However, the probe does have several limitations in its design for two primary reasons. First, the reaction mechanism (1,3-Huisgen cycloaddition) is catalytic in nature.

4.5.5 Drawbacks of a Catalytic Response Mechanism

Since the response mechanism of Tm-DOTA-click is catalytic, a single Cu(I) center would react with many molecules of the probe *in vivo*. This potential drawback could be eliminated in the designs of future ^{19}F MRI contrast agents wherein the response mechanism is not based on a catalytic reaction, but rather one that forms a complex with the analyte, sequestering its ability to participate in additional reactions with a other molecules of the probe. We chose the Cu(I)-catalyzed 1,3-Huisgen cycloaddition as mentioned before due to its relevance to AD, as well as our group's complimentary effort in developing luminescent sensors for Cu(I).

With these considerations, the ideal ^{19}F contrast agent would demonstrate a ratiometric response concomitant with a binding mechanism for its target analyte.

4.6 Conclusions

The design, synthesis and *in vitro* evaluation of a ratiometric responsive MR contrast agent for Cu(I) that consists of a fluorinated thulium complex has been presented. The paramagnetic thulium ion increases the sensitivity of the fluorines by decreasing their longitudinal relaxation rates by two orders of magnitude, thereby enabling more scans to be acquired per unit time. Notably, Tm(III) also provides two mechanisms for obtaining a response: variations in the conformation of the complex shift the ^{19}F signals by more than 10 ppm, whereas a change in the ^{19}F-Tm distance alters both the chemical shift and the longitudinal relaxation times of the fluorines. The large range of chemical shifts of ^{19}F, combined with the substantial response enables multichromic and ratiometric imaging of Cu(I) in three dimensions by MRI.

4.7 Experimental Materials and Methods

4.7.1 General Considerations

Unless otherwise noted, starting materials were obtained from commercial suppliers and used without further purification. Water was distilled and further purified by a Millipore cartridge system (resistivity 1.8×10^7 Ω). All organic extracts were dried over anhydrous $MgSO_4$ and solvents were removed under reduced pressure with a rotary evaporator. Flash chromatography was performed on Salicycle Silica Gel (230-400 mesh) or Brockmann activated aluminum oxide (neutral, 60 mesh). ^1H NMR spectra were recorded on a Varian 500 at 500 MHz, ^{13}C NMR spectra on a Bruker AV-500 at 125 MHz or a Varian 300 at 75 MHz, and ^{19}F spectra were recorded on a Bruker AV-500 at 471 MHz or a Varian Unity VXR-300 at 282 MHz at the LeClaire-Dow Characterization Facility of the Department of Chemistry at the University of Minnesota. The residual solvent peak was used as an internal reference for ^1H and ^{13}C NMR, and $CFCl_3$ or KF for ^{19}F NMR. Data for ^1H NMR are reported as follows: chemical shift (δ, ppm), multiplicity (s, singlet; br s, broad singlet; d, doublet: t, triplet; q, quartet; m, multiplet), integration, coupling constant (Hz). Data for ^{13}C and ^{19}F NMR are reported in terms of chemical shift (δ, ppm). Mass spectra (LR = low resolution; HR = high resolution; MS-ESI = electrospray mass spectrometry) were recorded on a Bruker BioTOF II at the Waters Center of Innovation for Mass Spectrometry at the Department of Chemistry at the University of Minnesota, Twin Cities.

4.7.2 Chemical Synthesis of Tm-DOTA-Click

2-Bromo-N-(2,2,2-trifluoroethyl)acetamide (4-2): 2,2,2-Trifluoroethylamine (4.00 mL, 27.5 mmol) was dissolved in CH_2Cl_2 (50 mL) and the solution was stirred in an ice bath. A solution of K_2CO_3 (16.5 g, 120 mmol) in H_2O (50 mL) and a solution of bromoacetyl bromide (2.40 mL, 27.7 mmol) in CH_2Cl_2 (50 mL) were simultaneously added dropwise over 30 min to the trifluoroethylamine, after which the reaction mixture was allowed to warm to room temperature and stirred for 1 h. The organic phase was separated and washed with H_2O (5 × 25 mL) and brine (1 × 20 mL), dried over $MgSO_4$, and concentrated under reduced pressure to yield the product (**4-2**, 4.88 g, 80.7 %) as white crystals. ^{1}H NMR (500 MHz, $CDCl_3$) δ 3.88-3.97 (m, 4H), 7.19 (br s, 1H); ^{13}C NMR (75 MHz, $CDCl_3$) δ 28.9, 41.9 (q, J = 34.8 Hz), 124.4, (q, J = 277 Hz), 167.4; ^{19}F NMR (282 MHz, $CDCl_3$) δ -72.9 (t, J = 8.7 Hz); MS (ESI) for $[C_4H_5BrF_3NO]^+$ ($[M + H]^+$): *m/z* 219.9579, found: 219.9579. The observed isotopic distribution matched the calculated one.

2-Bromo-N-(prop-2-yn-1-yl)acetamide (4-3): Propargylamine (2.00 mL, 31.2 mmol) was dissolved in CH_2Cl_2 (25 mL) and the solution was stirred in an ice bath. A solution of K_2CO_3 (17.5 g, 127 mmol) in H_2O (50 mL) and a solution of bromoacetyl bromide (2.80 mL, 32.3 mmol) in CH_2Cl_2 (50 mL) were simultaneously added dropwise to the propargylamine over 30 min, after which the reaction mixture was allowed to warm to room temperature and stirred for 45 min. The organic phase was separated and washed with H_2O (4 × 25 mL) and brine (1 × 20 mL), dried over $MgSO_4$, and concentrated under reduced pressure to yield the product (**4-3**, 3.99 g,

72.8 %) as dull orange crystals. ^{1}H NMR (500 MHz, $CDCl_3$) δ 2.28 (t, J = 2.5 Hz, 1H), 3.89 (s, 2H), 4.07 (dd, J_1 = 2.5 Hz, J_2 = 3.0 Hz, 2H), 6.82 (br s, 1H); ^{13}C NMR (75 MHz, $CDCl_3$) δ 29.4, 30.6, 79.3, 166.0; HRMS (ESI) calc for $[C_5H_6BrNO]^-$ ($[M - H]^-$): *m/z* 173.9555, found: 173.9545. The observed isotopic distribution matched the calculated one.

***Tert*-butyl (3-(2-(2-(3-aminopropoxy) ethoxy)ethoxy)propyl) carbamate (4-4):** A solution of di-*tert*-butyl dicarbonate (10.0 g, 45.9 mmol) in CH_2Cl_2 (50 mL) was added dropwise to a stirred solution of 1,13-diamino-4,7,10-trioxotridecane (20.2 g, 91.7 mmol) in CH_2Cl_2 (150 mL) over 1 h. The reaction mixture was stirred overnight then extracted with 0.1 M HCl (*aq*) (2 × 25 mL). The aqueous layer was slowly basified to pH = 4 with NaOH (*aq*) and back-extracted with CH_2Cl_2 (6 × 25 mL). The combined organic phases were washed with brine (1 × 40 mL), dried over $MgSO_4$, and concentrated under reduced pressure to yield the product (**4-4**, 26.5 g, 90.1 %) as an opaque colorless oil. ^{1}H NMR (500 MHz, $CDCl_3$) δ 5.16 (br s, 1H), 3.61-3.50 (m, 12H), 3.19 (d, J = 5 Hz, 2H), 2.81 (t, J = 6 Hz, 2H), 2.81, 2.47 (s, 4H), 1.73 (m, 4H), 1.41 (s, 9H); ^{13}C NMR (75 MHz, $CDCl_3$) δ 156.3, 79.1, 70.7, 70.3, 70.3, 70.0, 69.7, 69.6, 39.7, 38.5, 32.6, 29.8, 28.6; HRMS (ESI) calc for $[C_{15}H_{31}N_2O_5]^+$ ($[M + Na]^+$): *m/z* 343.2203, found: 343.2189.

***Tert*-butyl (1-bromo-2-oxo-7,10,13-trioxa-3-azahexadecan-16-yl)carbamate (4-5)**: A solution of the carbamate **4-4** (843 mg, 2.63 mmol) in CH_2Cl_2 (50 mL) was stirred in an ice bath. A solution of K_2CO_3 (422 mg, 3.05 mmol) in 20 mL H_2O and a

solution of bromoacetyl bromide (754 mg, 3.73 mmol) in CH_2Cl_2 were added simultaneously over 30 min to the carbamate, after which the reaction mixture was allowed to warm to room temperature and stirred for 1.5 h. The organic phase was separated and washed with H_2O (2 × 25 mL) and brine (1 × 10 mL), dried over $MgSO_4$, and concentrated under reduced pressure to yield the product (**4-5**, 691 mg, 59.5 %) as a colorless oil that was used without further purification. ^{1}H NMR (500 MHz, $CDCl_3$) δ 7.22 (br s, 1H), 5.28 (s, 2H), 4.94 (br s, 1H), 3.83 (s, 2H), 3.65-3.56 (m, 10H), 3.51 (t, *J* = 6 Hz, 2H), 3.39 (q, *J* = 6 Hz, 2H), 3.19 (m, 2H), 1.79 (q, *J* = 6 Hz, 2H), 1.73 (q, *J* = 6 Hz, 2H), 1.41, (s, 9H); ^{13}C NMR (75 MHz, $CDCl_3$) δ 165.7, 156.2, 79.2, 70.7, 70.5, 70.5, 70.3, 69.7, 53.6, 39.2, 38.8, 29.8, 29.5, 28.6; HRMS (ESI) calc for $[C_{17}H_{33}BrN_2O_6]^+$ ($[M + H]^+$): *m/z* 441.1595, found: 441.1606. The observed isotopic distribution matched the calculated one.

(1-(Azidomethyl)-4-(chloromethyl)-2,3,5,6-tetrafluorobenzene) (4-6): 1,4-Bis(chloromethyl)-2,3,5,6-tetrafluorobenzene (270. mg, 1.09 mmol) and sodium azide (113 mg, 1.74 mmol) were dissolved in anhydrous acetone (15 mL) and the reaction mixture was stirred at room temperature for 6 days. The reaction mixture was then filtered and concentrated under reduced pressure, deposited onto silica and purified via flash chromatography eluting with hexanes to afford the azide **4-6** as a thin colorless oil (150. mg, 54.1%). ^{1}H NMR (500 MHz, $CDCl_3$) δ 4.68 (s, 2H), 4.48 (s, 2H); ^{13}C NMR (75 MHz, $CDCl_3$) δ 146.3 (tt, J_1 = 16.5 Hz, J_2 = 5.8 Hz), 142.9 (tt, J_1 = 16.5 Hz, J_2 = 5.8 Hz), 117.0 (t, *J* = 16.5 Hz), 114.0 (*J* = 16.5 Hz), 41.7, 31.3; ^{19}F NMR (282 MHz, $CDCl_3$) δ -145.5, (ddd J_1 = 102 Hz, J_2 = 16.1 Hz, J_3 = 7.9 Hz).

2,2'-(1,4,7,10-Tetraazacyclododecane-1,7-diyl)bis(N-(2,2,2-trifluoroethyl)acetamide) (4-7): Cs_2CO_3 (11.6 g, 35.7 mmol) followed by the fluorinated acetamide **4-2** (3.43 g, 15.6 mmol) were added to a solution of 1,4,7,10-Tetraazacyclododecane (1.54 g, 8.93 mmol) in anhydrous CH_3CN (50 mL). The reaction mixture was stirred at 60 ˚C for 44 h, then cooled to room temperature, filtered and concentrated under reduced pressure to yield a yellow oil that was deposited onto alumina and purified via column chromatography eluting with 1% MeOH in CH_2Cl_2 to yield the cyclen derivative (**4-7**, 2.48 g, 61.7%) as a colorless oil that was further dried under high vacuum overnight. ^{1}H NMR (500 MHz, CD_3OD) δ 2.46-2.60 (m, 12H), 3.01-3.10 (m, 4H), 3.68-3.74 (m, 4H); ^{13}C NMR (75 MHz, CD_3OD) δ 55.1, 56.0 (d, *J* = 17 Hz), 61.6 (d, *J* = 10 Hz), 62.4, 62.6 (d, *J* = 6 Hz), 66.9, 68.8 (d, *J* = 27 Hz), 126.9, 134.3 (q, *J* = 277 Hz), 181.8; ^{19}F NMR (282 MHz, CD_3OD) δ -73.1 (t, *J* = 8.7 Hz); HRMS (ESI) calc for $[C_{16}H_{28}F_6N_6O_2]^+$ ($[M + H]^+$): *m/z* 451.2251, found: 451.2256.

2,2'-(4-(2-Oxo-2-(prop-2-yn-1-ylamino)ethyl)-1,4,7,10-tetraazacyclododecane-1,7-diyl)bis(N-(2,2,2-trifluoroethyl)acetamide) (4-8): K_2CO_3 (473 mg, 7.00 mmol) followed by the acetylene **4-3** (267 mg, 1.51 mmol) were added to a solution of the disubstituted cyclen **4-7** (1.05 g, 2.33 mmol) in anhydrous CH_3CN (150 mL). The reaction mixture was then stirred at 60 ˚C for 19 h, then cooled to room temperature, filtered, and concentrated under reduced pressure to yield a colorless oil which was further purified via column chromatography on alumina eluting with 0-5% MeOH in

CH_2Cl_2. The tri-substituted cyclen derivative **4-8** was obtained as a colorless glass (712 mg, 56.0%). ^{1}H NMR (500 MHz, $(CH_3)_2CO$) δ 8.71 (br s, 1H), 8.62 (br s, 1H), 8.27 (br s, 1H), 4.02-3.97 (m, 4H), 3.43 (s, 4H), 3.36 (s, 2H), 3.29 (s, 2H), 3.07-2.63 (m, 16H), 2.07 (t, J = 2.2 Hz, 1H); ^{19}F NMR (282 MHz, $(CH_3)_2CO$) δ -72.8 (t, J = 8.0 Hz); HRMS (ESI) calc for $[C_{21}H_{33}F_6N_7O_3]^+$ ($[M + H]^+$): *m/z* 546.2622, found: 546.2606.

Tert-butyl (1-(4,10-bis(2-oxo-2-((2,2,2-trifluoroethyl)amino)ethyl)-7-(2-oxo-2-(prop-2-yn-1-ylamino)ethyl)-1,4,7,10-tetraazacyclododecan-1-yl)-2-oxo-7,10,13-trioxa-3-azahexadecan-16-yl)carbamate) (4-9): K_2CO_3 (106 mg, 0.765 mmol) was added, followed by the carbamate **4-5** (135 mg, 0.306 mmol) were added to a solution of the tri-substituted cyclen derivative **4-8** (139 mg, 0.255 mmol) in anhydrous CH_3CN. The reaction mixture was stirred at 70 ˚C for 19 h, cooled to room temperature, filtered, then deposited on to alumina and purified via column chromatography yielding the fully substituted cyclen **4-9** which was used immediately in the next step (223 mg, 96.7 %). ^{1}H NMR (500 MHz, CD_3OD) δ 4.04-3.95 (m, 4H), 3.63-3.58 (m, 12H), 3.29-3.82 (m, 16H), 2.78-2.10 (dd, J_1 = 13.5 Hz, J_2 = 6.5 Hz, 12H) 1.78 (q, J = 6.0 Hz, 4H), 1.72 (q, J = 6.5 Hz, 4H), 1.44 (s, 9H); ^{13}C NMR (75 MHz, CD_3OD) δ 171.2, 169.2, 154.2, 154.1, 124.2, (q, J = 279 Hz), 79.8, 79.3, 73.2, 72.2, 71.5, 70.5, 70.3, 69.2, 59.4, 58.2, 56.6, 56.2, 55.3, 52.7, 39.2, 38.3, 27,4, 21.1; ^{19}F NMR (282 MHz, $(CH_3)_2CO$) δ -72.8 (t, J = 8.0 Hz); HRMS (ESI) calc for $[C_{21}H_{33}F_6N_7O_3]^+$ ($[M + H]^+$): *m/z* 546.2622, found: 546.2606.

2,2'-(4-(16-amino-2-oxo-7,10,13-trioxa-3-azahexadecyl)-10-(2-oxo-2-(prop-2-yn-1-ylamino)ethyl)-1,4,7,10-tetraazacyclododecane-1,7-diyl)bis(N-(2,2,2-trifluoroethyl)acetamide) (4-10): Trifluoroacetic acid (10 mL) was added dropwise over 5 min to a solution of the protected cyclen **4-9** (223 mg, 0.247 mmol) in CH_2Cl_2 (50 mL) in an ice bath. Once addition was complete, the reaction mixture was warmed to room temperature and stirred overnight. Volatiles were removed under reduced pressure, after which subsequent portions of cold MeOH (3 × 5 mL) were added and then concentrated. The final amine **4-10**, obtained as a yellow oil, was further dried under high vacuum overnight (197 mg, 99.0%). ^{1}H NMR (500 MHz, CD_3CN) δ 7.57 (br s, 1H), 7.41 (br s, 1H), 7.23 (br s, 2H), 3.97-3.89 (m, 8H), 3.67 (d, *J* = 3.3 Hz, 4H), 3.59-3.48 (m, 16H), 3.35-2.73 (m, 20H), 1.72 (quintet, *J* = 7.2 Hz, 4H); ^{19}F NMR (282 MHz, CD_3CN) δ -76.4; HRMS (ESI) calc for $[C_{38}H_{65}F_6N_9O_9]^+$ ($[M + H]^+$): *m/z* 905.4809, found: 905.4783.

2,2'-(4-(1-(4-(Azidomethyl)-2,3,5,6-tetrafluorophenyl)-17-oxo-6,9,12-trioxa-2,16-diazaoctadecan-18-yl)-10-(2-oxo-2-(prop-2-yn-1-ylamino)ethyl)-1,4,7,10-tetraazacyclododecane-1,7-diyl)bis(N-(2,2,2-trifluoroethyl)acetamide) (4-11): K_2CO_3 (377 mg, 2.73 mmol), followed by a stock solution of the azide **4-6** in anhydrous CH_3CN (86.8 mg, 0.342 mmol), were added to a solution of the cyclen derivative **4-10** (550. mg, 0.683 mmol) dissolved in anhydrous CH_3CN (40 mL). The reaction mixture was stirred at 50 ˚C for 34 h, then filtered, and purified via column chromatography over alumina eluting with 0-5% MeOH in CH_2Cl_2. The free ligand DOTA-click (**4-11**) was obtained as a clear colorless oil that was further dried under

high vacuum overnight (285 mg, 81.5 %). ^{1}H NMR (500 MHz, $CDCl_3$) δ 1.75-1.85 (m, 4 H), 1.99-2.83 (m, 20 H), 2.84-3.31 (m, 12 H), 3.44-3.59 (m, 12 H), 3.75-3.99 (m, 6 H), 4.45 (s, 2 H), 8.25 (br s, 2 H), 8.80 (br s, 2 H); ^{13}C NMR (75 MHz, $CDCl_3$) δ 172.4, 171.9, 171.8, 171.3, 171.0, 170.9, 146.1, 143.0, 124.0 (q, J = 278 Hz), 79.8, 77.0, 71.0, 70.1, 70.0, 69.8, 69.7, 69.6, 69.5, 69.3, 56.8, 56.8, 52.9, 50.1, 46.2, 41.6, 40.6, 37.5, 29.3, 28.6; ^{19}F NMR (282 MHz, $CDCl_3$) δ -72.3 (t, J = 25.7 Hz), -143.9 (dt, J_1 = 87.1 Hz, J_2 = 13.5 Hz); HRMS (ESI) calc for $[C_{41}H_{60}F_{10}N_{12}O_7]^+$ ($[M + Na]^+$): *m/z* 1045.4440, found: 1045.4461.

Tm-DOTA-click (4-1): H_2O (10 mL) followed by a stock solution of $TmCl_3$ in H_2O (27.8 mg, 0.101 mmol) were slowly added to a solution of the free ligand **4-11** (103 mg, 0.101 mmol) in CH_3CN (10 mL). The acidic reaction mixture was stirred at room temperature, slowly basified with NaOH (*aq*) to pH 8, and then stirred at 70 ˚C for 19 h. The reaction mixture was then allowed to cool and diluted with H_2O (30 mL), passed through 0.2 µm syringe filter and lyophilized to yield an off-white crystalline solid (**4-1**, 119 mg, 99.0%). ^{1}H NMR (500 MHz, D_2O) δ -27.7-(-16.1) (m), -12.7-9.8 (m), 18.9-40.2 (m), 43.1-49.0 (br m); ^{19}F NMR (282 MHz, D_2O) δ -81.9-87.6 (m), -145.3 (d, J = 127 Hz); HRMS (ESI) calc for $[C_{41}H_{62}F_{10}N_{12}O_7]^{2+}$ ($[M - H]^{2+}$): *m/z* 596.1984, found: 596.1997.

^{19}F NMR. ^{19}F spectra were recorded on a Varian Unity VXR-300 at 282 MHz at 20 °C at the LeClaire-Dow Characterization Facility of the Department of Chemistry at the University of Minnesota. A KF solution in D_2O was used as an external standard and

to lock and shim all samples containing the paramagnetic Tm-DOTA-click. Samples of Tm-DOTA-click were dissolved in deionized water further purified by a Millipore cartridge system (resistivity 1.8×10^7 Ω) and analyzed. Cu(I)ascorbate was then added to the contrast agent sample to bring the final concentration of Cu(I) to 0.10 eq of Tm-DOTA-click. In each experiment, [ascorbate] = 5 × [Cu(I)]. The excess ascorbate is used in order to maintain all copper in its +1 oxidation state. Samples were allowed to react for 2 hours before measurements were performed. Longitudinal (T_1) and transverse (T_2) relaxation times of each fluorines in mQ water were measured using the inversion recovery sequence and the Carr-Purcell-Meiboom-Gill sequence, respectively. ^{19}F lanthanide induced relaxation enhancement (FLIRE) spectra were acquired with the following parameters. A recycle delay equal to 5 × the longest ^{19}F T_1 was followed by a 180° pulse and an inversion time equal to $ln(2) \times T_{1\,(longest)}$. At this point, fluorine nuclei with short T_1 have recovered some magnetization in the Z-direction whereas those with the longer T_1 have not. A 90° pulse was then applied and the FID was recorded. This pulse sequence enabled elimination of the signal of the fluorine nuclei with the longer $T_{1+,}$ which in this case were the aromatic fluorines prior to reaction of the probe with Cu(I).

MRI. MR images of samples in 3 mm NMR tubes were acquired on a 16.4 T, 26-cm horizontal bore magnet (Magnex Scientific, Oxford, UK) interfaced with a Varian Direct Drive console (Varian, Palo Alto, CA, USA). The magnet was equipped with a gradient insert capable of reaching 1000 mT/m in 150 μs (Resonance Research, Inc.,

Billerica, MA). A linear surface coil (12 mm diameter) tunable to both ^{1}H (698.1 MHz) and ^{19}F (656.8 MHz) frequency was used to transmit and receive the signal. ^{1}H gradient echo images were acquired using following parameters: repetition time (T_R) = 40 ms, echo time (T_E) = 1.28 ms, field of view (FOV) = 3 cm x 3 cm, matrix = 128 x 128, slice thickness = 10 mm, flip angle = 20°. ^{19}F gradient echo images were acquired using following parameters: T_R = 20 ms, T_E = 2.73 ms, FOV = 2 cm x 2 cm, matrix = 64 x 64, slice thickness = 10 mm, excitation pulse = 4 ms sinc, flip angle = 90°, number of averages (na) = 512 or 2048.

5 *In Vivo* Analysis of ^{19}F MRI Contrast Agents

5.1 Introduction

In the final chapter of this dissertation, the work done to finally test ^{19}F-based MRI contrast agents *in vivo* will be described. The complexes described in the preceding chapters have only been tested *in vitro*, and while they had always been designed with biocompatibility in mind, they had not been tested *in vivo* to this point. Some of the design considerations and goals of the aforementioned compounds were made with greater focus for sensitivity and responsive probes rather than with maintaining the characteristics of what makes for a biocompatible probe. This chapter addresses perhaps the most important property of any new potential therapeutic compound: biocompatibility. As such, a number of ^{19}F MRI contrast agents were tested in rat models *in vivo*, and observations of their half-life and biodistribution were recorded, as well as monitoring the health of the rats following the administration of these probes.

5.1.1 ^{19}F MRI Contrast Agents Used for *in vivo* Studies—Structure

Six paramagnetic contrast agents were used for ^{19}F MRI in an attempt to overcome solubility and in particular, toxicity issues, the former of which were discussed in detail in Chapters 2 and 3. These six contrast agents were produced by combining one of three macrocyclic scaffolds, with one based on a cyclen-tetraphosphontate (DOTP) ligand and two others with DOTA-tetraamide ligands, each with with the paramagnetic metal ion of either Tm(III) or Fe(II), as shown in Figure 5-1.

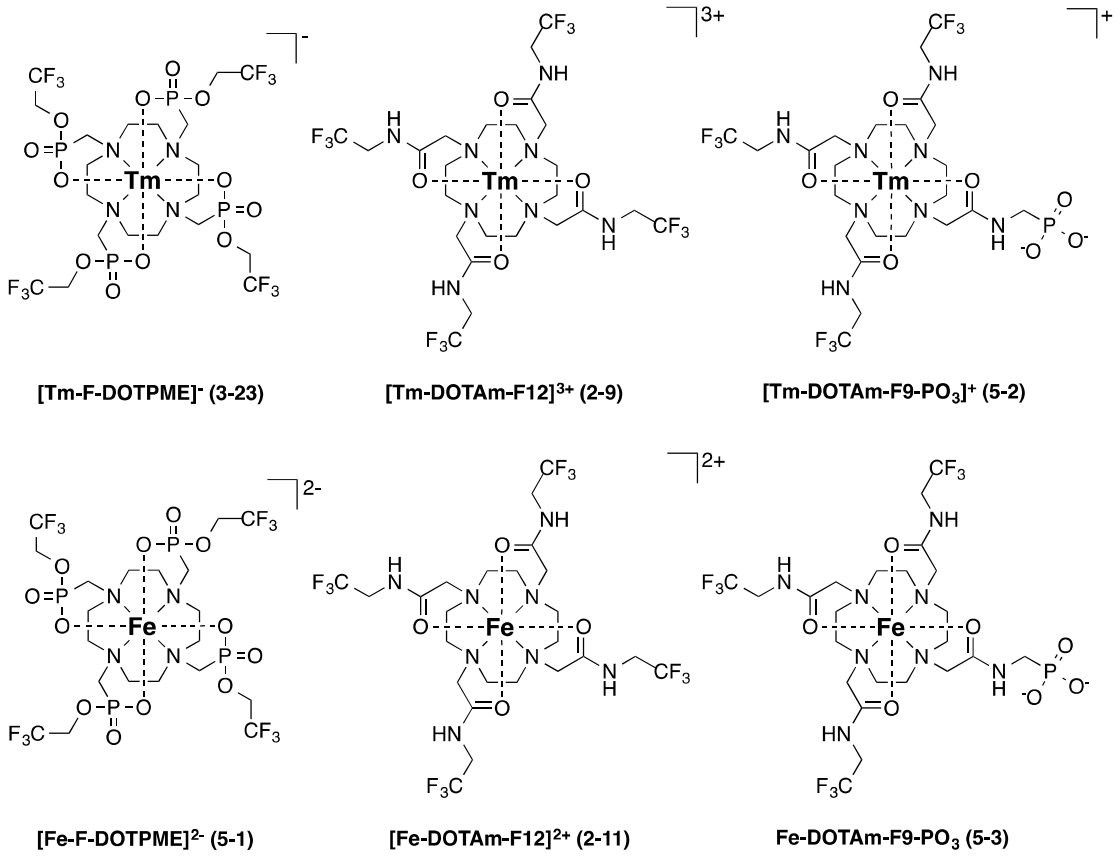

Figure 5-1: ^{19}F MRI contrast agents for in vivo studies. Chemical structures of Three ligands used, six complexes 3-23 and 5-1, 2-9 and 2-11, and 5-2 to 5-3 explored as potential fluorine-based MRI contrast agents in this project. Each of three ligands was complexed with either Fe(II) or Tm(III). While the structures are similar, the six contrast agents each possess a different net charge (ranging from -2 to +3) and a slightly varied chemical structure, giving each compound unique pharmacological and magnetic properties.

These structural motifs – of which their lanthanide complexes do have a significant history in the literature surrounding contrast agent development – were employed because they provide some of the highest levels of stability and kinetic inertness in complexes with gadolinium.[197] These contrast agents were synthesized with either nine or twelve fluorine atoms per molecule, which enabled facile detection by ^{19}F MRI, and Tm(III) and Fe(II)—rather than gadolinium—were used as the paramagnetic metal ions. These ions were chosen based on the study of T_1 and T_2 values of the DOTAm-F12 ligand containing various paramagnetic metal ions in both aqueous solution and in

rat blood, described in Chapter 2. Tm(III) and Fe(II) showed the greatest reduction of T_1 while maintaining a high ratio of T_2/T_1 in both systems. The combination of the high number of fluorine atoms per molecule and the Tm(III) or Fe(II) metal ions provided much greater sensitivity over currently available fluorinated contrast agents.

The number of fluorines per probe was maximized while employing different structural properties aimed at modulating the overall charge of the probes. The contrast agents in this study were all soluble in both water and saline buffer to concentrations over 50 mM. This high solubility in aqueous solutions made these compounds feasible for use as MRI contrast agents in biological systems.

The final aspect in this chapter is the evaluation of parameters that limit their toxicity. Many currently existing fluorinated contrast agents have either displayed very high toxicity in animal models or long retention times in biological systems, or they have not been studied in relevant systems to assess their toxicity. Structural similarities to clinically available gadolinium-based agents—which feature tight chelation of the metal ion—possess the potential to be non-toxic to live animals. Additionally, using three different ligands and two different metals provided greater diversity of molecular structure, charge, and size, maximizing the possibility that a nontoxic contrast agent with the highest sensitivity in *in vivo* imaging could be found for the complexes examined. Finally, the use of iron eliminated any gadolinium- or lanthanide-based toxicity, which is a major drawback of currently available MRI contrast agents. While thulium has similar toxicity issues as gadolinium, the iron counterparts do not, and the iron complexes were predicted to produce much less toxicity issues if they were to dissociate from the complex *in vivo*.

Even though the basic architecture of these contrast agents was derived from work already published in the literature, the two DOTA-tetraamide ligands shown in Figure 5-1 were designed and synthesized for the first time in this project. The other ligand, F-DOTPME, was originally reported by Kim et al., but was only characterized in aqueous solutions and not in a biological environment.[84] Additionally, Fe(II) and Tm(III) have not previously been used *in vivo* as paramagnetic metals in MRI contrast agents. Finally, this work is the first systematic study of acute toxicity, retention times and biodistribution of any metal-based ^{19}F MRI contrast agent *in vivo*.

In this study, each of the six potential contrast agents was synthesized and characterized to ensure purity and to determine magnetic relaxation times T_1 and T_2. Additionally, a systematic pharmacological and toxicological study was undertaken by injecting rats with each of the contrast agents to first determine acute toxicity of the compounds. Blood and tissue samples taken from each animal were then analyzed for contrast agent concentration to assess organ biodistribution and blood retention times for each agent. These experiments aimed to identify the most favorable of the six compounds for *in vivo* use.

The ligand DOTAm-F12 was synthesized as reported in Chapter 2. The ligand F-DOTPME was synthesized as reported in Chapter 3. The ligand DOTAm-F9-PO_3 (**5-8**) was obtained over six steps, shown in Scheme 5-1. First, the amine (**5-4**) was obtained through cleavage of the commercially available Garbriel adduct with hydrazine.

5.1.2 Synthesis of Contrast Agents

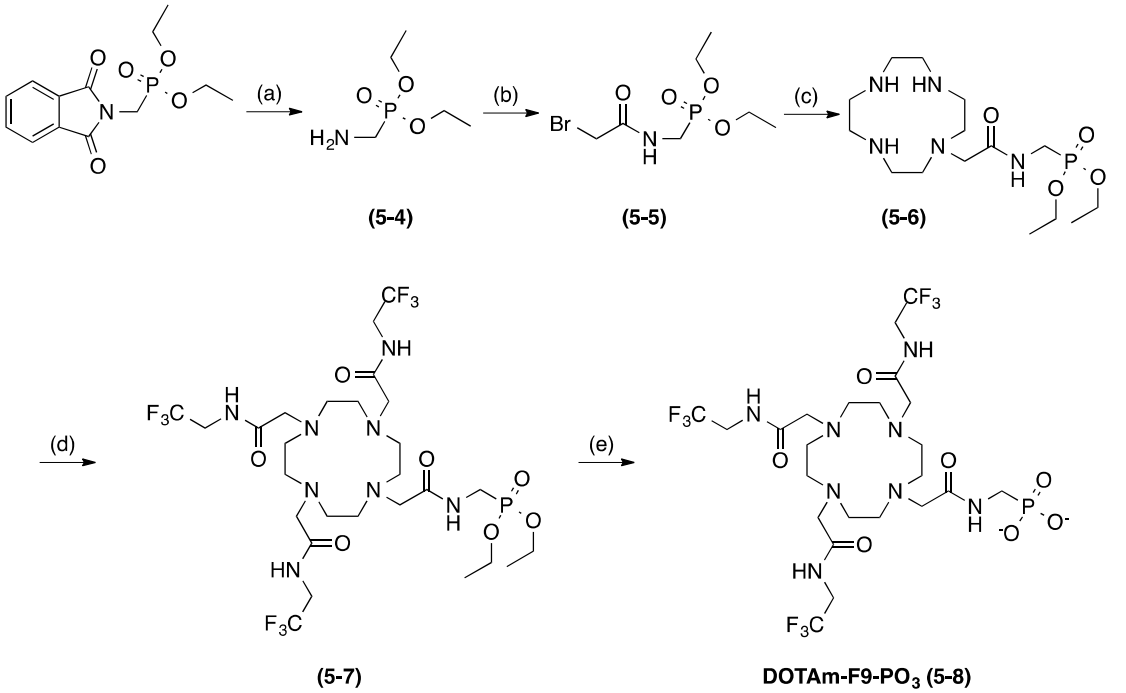

Scheme 5-1: Synthesis of f-DOTPME and DOTAm-F9-PO_3. Experimental conditions: (a) hydrazine, EtOH, 22 ºC, 18 h -> reflux, 3 h, 45%; (b) bromoacetyl bromide, NaOH, CH_2Cl_2/H_2O, 0 ºC -> 22 ºC, 1 h, 60%; (c) cyclen, triethylamine, $CHCl_3$, 60 ºC, 18 h, 57%; (d) 2-bromo-*N*-(2,2,2-trifluoroethyl)acetamide, K_2CO_3, CH_3CN, 60 ºC, 18 h, 54%; (e) TMS-Br, DMF, 0 ºC -> rt, 18 h, 55%.

Subsequent alkylation with bromoacetyl bromide yielded the protected phosphate arm (**5-5**) and singly alkylated to cyclen to yield **5-6**. The cyclen ring was then exhaustively alkylated with the -CF_3 pendant arm to yield the protected ligand **5-7** before hydrolysis of the phosphate esters with TMS-Br, and the final product was purified by reverse-phase HPLC and lyophilized to yield the free ligand DOTAm-F9-PO_3 (**5-8**) as a white powder.

Metallation of **5-8** with Tm(III) and Fe(II) was accomplished in similar fashion as for DOTAm-F12, described in Chapter 2, using instead a 10% excess of the ligand relative to the metal to yield $[Tm\text{-}F\text{-}DOTPME]^-$ (**3-23**), $[Fe\text{-}F\text{-}DOTPME]^{2-}$ (**5-1**), $[Tm\text{-}DOTAm\text{-}F9\text{-}PO_3]^+$ (**5-2**) and Fe-DOTAm-F9-PO_3 (**5-3**). All six resultant metal

complexes were readily soluble in water at neutral pH at concentrations greater than 100 mM.

5.1.3 ^{19}F Relaxation Times

Before *in vivo* testing was undertaken, the six contrast agents were tested in aqueous environments at neutral pH to determine the T_1 and T_2 relaxation times of the fluorine nuclei on each compound. As described earlier, contrast agents having high T_2/T_1 ratios as close to 1 as possible have produced the strongest signals and highest SNR ratios when imaged by MR. The T_1 and T_2 values for the two new free ligands and their respective Tm(III) and Fe(II) metal complexes were measured by ^{19}F NMR at 282 MHz and compared to the values obtained for the DOTAm-F12 ligand and its Tm(III) and Fe(II) complexes reported in Chapter 2. The results are reported in table 5-1.

As expected, the fluorine nuclei located on the three organic ligands lacking a paramagnetic metal ion exhibited very long relaxation times, ranging from 650 to 1000 milliseconds . Introduction of a paramagnetic ion induced significant reductions in the relaxation times to a range of 5 to 40 milliseconds, with the DOTA-tetraamides DOTAm-F12 and DOTAm-F9-PO_3 **(5-13)** displaying very similar values. As shown in Table 5-1 all of the contrast agents utilized in this study possessed T_1 values of 50 ms or less, and the highest T_2/T_1 ratios were observed for [Fe-DOTAm-F12]$^{2+}$ (0.98) and Fe-DOTAm-F9-PO_3 (5-3) (0.83 and 0.63).

The T_1 and T_2 values of 5.7 and 5.6 milliseconds for contrast agent 2-9 and 5.8 and 4.8 milliseconds for contrast agent 5-3 in this study were among the lowest fluorine relaxation times of any compound found in the literature.[82,198,199]

Table 5-1: T_1 and T_2 relaxation values for ^{19}F nuclei. T_1 and T_2 values of the ^{19}F nuclei in the three precursor ligands and in their Tm(III) and Fe(II) complexes, measured in aqueous solution at neutral pH at 282 MHz. [a]Value found by Kim et al.[84] [b]Spectrum for 5-1 displayed multiple resonances corresponding to stereoisomers. axial and equatorial over a wide frequency range, each with distinct T_1 and T_2 values. [c]For compounds with spectra displaying two signals over a narrow frequency range (i.e. both could be imaged in a single MRI scan), individual relaxation time values are given for each signal.

Contrast Agent	T_1 Relaxation Time (ms)	T_2 Relaxation Time (ms)
F-DOTPME (5-8)	928	312[a]
3-23	11 (ax.), 41 (eq.)[b]	5 (ax.), 19 (eq.)
5-1	29.5[c] 35.0	4.9 10.1
DOTAm-F12	880	680
2-9	26.0	16.0
2-11	5.7	5.6
DOTAm-F9-PO_3 (5-13)	719	154
5-2	25.8	17.1
5-3	6.4[c] 5.8	4.0 4.8

Fe(II) was particularly effective at reducing relaxation times and producing high T_2/T_1 ratios for the compounds used in this study, further indicating its potential for use and development in ^{19}F contrast agents. In fact, this study is the first report of an Fe(II)-based ^{19}F MRI contrast agent that has been tested *in vivo*. Using Fe(II) as the paramagnetic metal ion rather than lanthanides has yielded some of the most sensitive probes discussed herein, and may likely reduce potential safety concerns.

5.1.4 ^{19}F Signal Intensity

As reported by Kim et al., metal complexes of the F-DOTPME ligand **(5-8)** result in the formation of multiple stereoisomers in solution, resulting in multiple fluorine signals over a wide chemical shift range.[84] These resonances are produced from various combinations of isomers, wherein the -CF_3 groups can adopt either an axial or equatorial orientation relative to the metal center. Four unique combinations of *R* and *S* are possible for the four chiral centers. The peaks cluster at two main frequencies near -60 ppm and -120 ppm for fluorine atoms either in the axial or equatorial positions, respectively, relative to the principle magnetic axis of the paramagnetic metal (θ). The shifts in frequencies observed are rationalized by the McConnel-Robertson equation's (2-2) dependence on the angle θ between the paramagnetic metal center and the detected nuclei.

The presence of multiple peaks across the wide frequency range reduces MR sensitivity. In this case, the sensitivity would be reduced, as only six of the total twelve fluorine nuclei of the probe could be imaged with one pulse sequence. For the Tm(III) complex **3-23**, these would be the clustered signals from equatorial fluorines centered at δ = -39 ppm. The signals from axial fluorines are too distant from one another to be imaged together. In addition, while MRI could detect the equatorial fluorines in one pulse sequence, the images produced would further suffer a loss in resolution when imaged together, as was illustrated in the case of PFOB described in Chapter 1. Kim et al. briefly noted in that F-DOTPME epimerizes to a single isomer in the presence of aqueous detergents in their 1997 report but didn't explore this effect further at the time. However, in 2009 the same group reported that a metal complex—very similar to

3-23—epimerized to a single isomer with a single resonance when in blood, after originally displaying the expected twelve resonances by ^{31}P NMR in neutral aqueous media alone.[200] While contrast agent **3-23** was not tested in blood or serum albumin, it is possible that the same effect would occur. Thus, the problem of having signals spread over too wide a range for MRI may be eliminated.

Although the spectrum of contrast agent **3-23** displayed multiple signals over a wide frequency range, the other five compounds tested did not. Overall, the relaxation data obtained combined with high water solubility suggests that all six of these compounds should be sensitive enough for MR imaging at physiologically safe concentrations. These compounds would be especially advantageous over many of the perfluorocarbon agents described above that displayed very long T_1 relaxation times and low T_2/T_1 ratios.

5.2 Preliminary *In Vivo* Experiments

In order to examine the biocompatibility of the proposed contrast agents and to determine their retention times and distributions within a biological system, the six metal complexes were injected into rats fixed with a catheter. To minimize the potential toxicity produced by these injections, the compounds were determined to be pure by nuclear magnetic resonance spectroscopy and final determination of purity was analyzed by HPLC. Prior to injection, the contrast agents were also tested in the presence of the metal indicator xylenol orange to ensure that the injection contained no free metal ions. Each contrast agent was dissolved in phosphate-buffered saline (PBS) to form 1 mL of a 50 mM solution. The solutions of each agent were injected into a pair of three-month old rats fitted with jugular vein catheters for each compound. The

rats were monitored over a period of four hours, with blood samples removed throughout that period. Animals were euthanized after four hours so that tissue samples could also be removed. The four-hour period was chosen in order to accurately assess the physiological distribution of the contrast agent while limiting chronic toxicity effects. Because those chronic effects could result from the dissociation of metal ions from the ligand, they would require a much longer period of time to produce negative impacts on the animals.

5.2.1 Acute Toxicity of DOTAm-F12 Complexes

The first *in vivo* studies conducted were with the DOTAm-F12 contrast agents **2-9** and **2-11** (Figure 5-1). These two complexes resulted in death of all rats within five minutes post-injection. This demonstration of acute toxicity was hypothesized to be a result of ionic shock. These two contrast agents carry an overall charge of +3 and +2 for the Tm(III) and Fe(II) complexes, respectively. Previous studies of similar cationic compounds have found that the highly cationic charge interferes with, and may even completely stop, heart function.[201] Regardless of the actual cause of death, because the animals tested with these compounds died quickly, and contrast agents **2-9** and **2-11** were no longer considered for further study.

5.2.2 Four New Contrast Agents with Reduced Charge

Two new ligands were then designed and synthesized as discussed above to maintain high fluorine labeling but to reduce overall charge of the metal complexes. The DOTAm-F12 ligand is charge-neutral and produces Tm(III) and Fe(II) complexes of +3 and +2, whereas the F-DOTPME ligand and the DOTAm-F9-PO_3 ligand carry a -4 and -2 overall charge respectively, forming -1/-2 and +1/0 metal complexes with

Tm(III)/Fe(II). The other four contrast agents produced no visible impacts on the six rats over the course of the observation period. Rats injected with these contrast agents tolerated the compounds and were alive and active until the end of the four-hour period.

5.3 Biodistribution Properties

5.3.1 Blood Retention

Following injection of each contrast agent into rats, 500 μL blood samples were removed via the jugular vein catheter after 5, 15, 30, 60, 120, and 240 minutes. Each blood sample was then digested with heat and nitric acid to produce a clear, yellow liquid. The concentration of fluorine within the sample following acid digestion was determined using ^{19}F NMR using an external standard. The integration values for the peaks in the NMR spectrum corresponding to the digested sample were compared to integration values for the external standard solution of aqueous potassium fluoride of known concentration contained in a smaller, sealed capillary tube present along with the sample. As endogenous fluorine concentrations are extremely low (<0.1 ppm) in normal plasma, monitoring the concentration of fluorine over time served as a good proxy for following the concentration of the contrast agent as it was excreted.[202] The results are shown in Table 5-2.

As shown in Table 5-2, the concentrations of contrast agents **3-23** and **5-2** decreased rapidly within the first hour after injection, while the iron-containing agents **5-1** and **5-3** were removed from the blood at a slower, but nonetheless at rate for clearance of 4-6 hours. These clearance times are slightly longer than those for Gd(III)-

based contrast agents, but are still within an acceptable timeframe for established safety protocols.

Table 5-2: Summary of *in vivo* contrast agent injections. The blood half-life is the amount of time after injection at which half of the injected contrast agent was present in the blood, and the primary organs are those in which the highest concentrations of contrast agent were found four hours post-injection (p.i.).

Contrast Agent	Net Charge	Animal Outcome	Blood Half-Life	Primary Organs
F-DOTPME				
5-1	+1	Survived	49 min.	kidney
5-2	0	Survived	72 min.	kidney
DOTAm-F12				
5-3	+3	Died – 5 minutes p.i.	n/a	n/a
5-4	+2	Died – 2 minutes p.i.	n/a	n/a
DOTAm-F9-PO_3				
5-5	-1	Survived	58 min.	kidney
5-6	-2	Survived	55 min.	kidney

Each contrast agent examined *in vivo* was done so in triplicate to identify outliers. There is a clear trend in all four agents that only a fraction of the original amount of contrast agent remains in the blood after four hours.

As indicated in Table 5-2, clearance to half the initial concentrations found for each agent in the blood was between 45 and 75 minutes. This is not be confused with each probe's actual half-life but does suggest that the probes are rapidly cleared. For

comparison, all but one of the FDA-approved gadolinium-based contrast agents demonstrate elimination half-lives between 60 and 120 minutes.[24] Thus, the contrast agents in this study displayed retention and clearance times comparable to the contrast agents used today. These half-lives would allow for a 30-60 minute period of high concentration for imaging, followed by rapid clearance from the body. This time course suggests that the requisite sensitivity for MR imaging can be provided while maintaining a strong safety profile.

In terms of chronic toxicity, the Fe(II)-based contrast agents **5-1** and **5-3** in this study negated one major hazard of currently available MRI contrast agents, which is the gadolinium-based nephrogenic systemic fibrosis (NSF) that occurs in patients with moderate to severe kidney impairment.[203] The toxicity of Tm(III)-based contrast agents has not been studied in great detail, but, as a lanthanide metal that is not normally present in the body in large quantities, it is likely to have similar side effects to that of Gd(III). On the other hand, iron is far less toxic than gadolinium and is present at relatively high concentrations in most biological systems. For example, the average concentration of iron in human blood is 473 ± 88 ppm.[204] Most of this iron in the blood is not in its free ionic form because the human body has several mechanisms that maintain iron homeostasis. Hepcidin is a hormone produced by the liver that regulates the metabolism of iron by other cell types, and iron is also incorporated into other biological macromolecules, such as transferrin and ferritin.[205] An injection of the iron-containing contrast agents in this study at the standard concentration of 0.1 mmol/kg would increase the concentration by roughly 70 ppm. However, this increase would only be realized if all iron ions dissociated from their ligands. Work by Morrow

has demonstrated that Fe(II) complexes such as the contrast agents in this study are highly inert in the presence of other physiological anions, indicating that very little iron dissociates from the complexes in biological environments. [206]

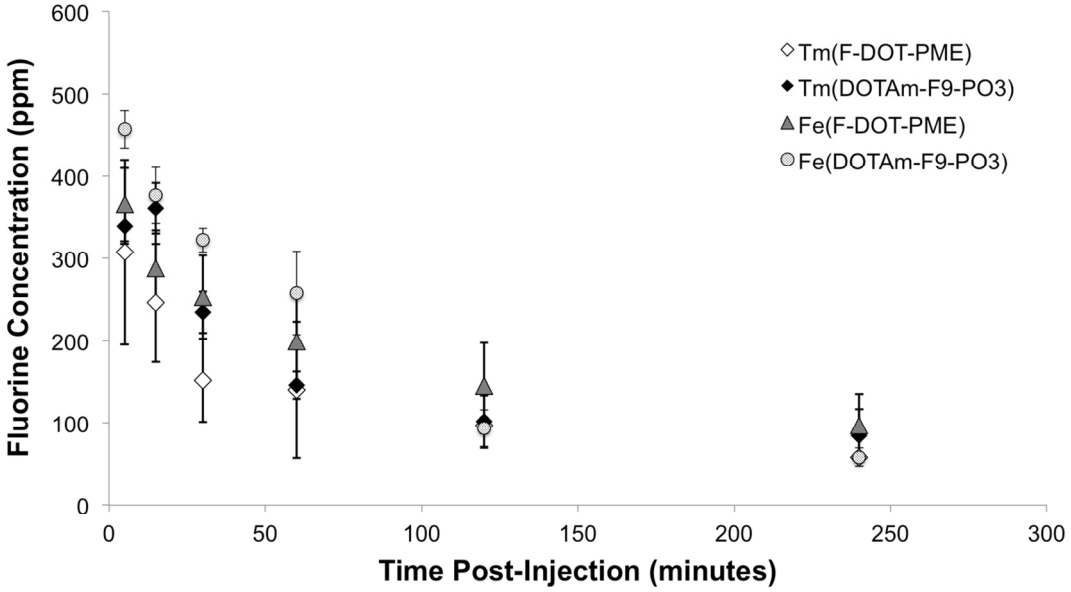

Figure 5-2: Mean concentration of contrast agents in rat blood over 4 hours post-injection. Mean concentrations of ^{19}F in blood samples from rats injected with contrast agent indicated. Concentrations are given in units of parts per million (ppm), error bars represent standard deviation (n = 3).

In addition, while iron and specifically Fe(II) are known to catalyze the formation of harmful reactive oxygen species (ROS) such as hydroxyl radical and nitric oxide, the same study also demonstrated that Fe(II) metal complexes similar to **5-1** and **5-3** used for this study produce extremely low ROS levels, thus limiting the degree of iron toxicity that these contrast agents might produce in this manner.

5.3.2 Organ Distribution

The four contrast agents that were non-lethal to rats *in vivo* were further studied by analyzing organ samples collected from the rat models euthanized 4 hours post-injection. Portions of brain, heart, kidney, liver, lung, and spleen were removed to determine the concentration of contrast agent within each vital organ. Like the blood

samples, the organ samples were also digested with heat and nitric acid, and the concentrations of fluorine were determined using NMR. The results are shown in Figure 5-3.

In this case, the data shown represents the percentage of total injected fluorine – out of 11.4 mg for **3-23** and **5-1** and 8.55 mg for **5-2** and **5-3** – that was present in each organ after four hours (Figure 5-2). Like gadolinium-based contrast agents, it was expected that these agents would primarily be excreted via the kidneys, given the basic structural similarities between the compounds. The data in Figure 5-3 indicates that the kidneys possessed the highest amount of each contrast agent, which is consistent with the renal system being the primary mode of elimination. The spleen, heart, brain, and lungs all displayed low levels of fluorine, which most likely stemmed from the vascularization of these organs and any excess blood that was removed when the organs were excised. The liver contained a slightly higher level of all three agents, but that was likely due to the fact that the liver is a much larger organ. There are two exceptions to the above trends in the data. One animal displayed a very high level of contrast agent **5-1** in the brain, and another showed a high level of contrast agent **2-9** in the liver.

Since the fluorine was found to accumulate at a significantly higher level in the kidneys than in other organs, it can be assumed that the urinary system is likely the primary mode of excretion for these contrast agents. The compounds' high water solubility also supports this conclusion. As in the case of gadolinium-based contrast agents, this mode of excretion provides the most rapid clearance from the body, limiting the potential for toxicity produced by transmetallation of metal ions.

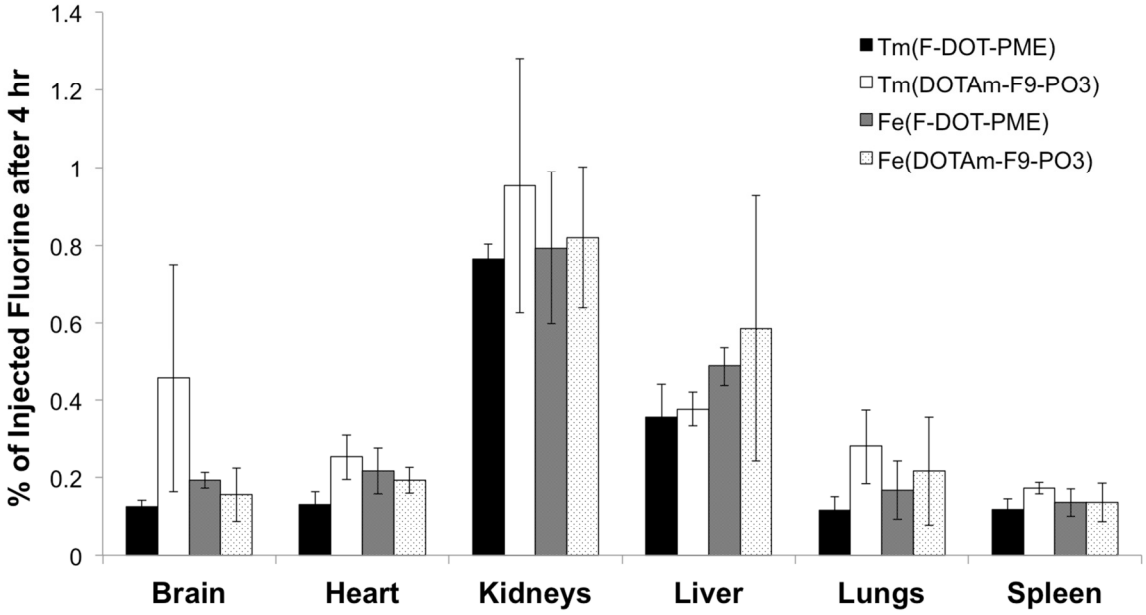

Figure 5-3: Concentration of contrast agents within vital organs. This figure shows the mean percentage (n = 3) of total contrast agent injected that accumulated in each of the six vital organs examined in the experiment. The concentration of 19F in each organ was first determined in parts per million. Then, the mass of each organ and the total mass of fluorine contained in each 1 mL injection volume were used to determine the percentages shown. Error bars represent the standard error of the mean

5.4 Imaging ^{19}F Contrast Agents Directly *In Vivo*

The final step of this project would be to acquire *in vivo* images of rats injected with the contrast agents presented in this chapter. These images will help determine if the non-lethal concentration used in these studies provides sufficient sensitivity for *in vivo* MRI. The concentration used for these experiments was near 0.2 mmol/kg. For the currently available gadolinium-based agents, the standard dose is 0.1 mmol/kg and the maximum dose allowed by the FDA is near 0.6 mmol/kg.[24] Thus, the concentration that would be used in this study to examine toxicity and sensitivity by collecting MR images is relevant to clinically available contrast agents.

While these final experiments are planned as future work in this study, they were unable to be completed by the time this document was written.

5.5 Conclusions and Future Work

Despite the promising nature of the results presented above, there are some important qualifications that merit identification and discussion. The most important is that although the compounds had no adverse effects on the rats in which they were tested, this study did not conduct a rigorous examination of those potential effects. It was noted whether or not the rats survived the injections for four hours, but no detailed examination was performed to determine any possible disruptions of internal physiological processes. Additionally, the compounds are modeled off existing structural motifs that produce high stability and inertness and prevent release of the metal ion from the organic ligand.[197] However, these parameters were not explored for these compounds specifically. Stability experiments and binding assays with competing metal ions that are present in tissues would need to be conducted to determine the behavior of interaction between the metal ion and the organic ligand in biological environments.

While numerous additional studies are required to assess the safety, pharmacology, and practicality of the contrast agents studied, the data presented in this chapter clearly indicates the potential of ^{19}F MRI contrast agents as diagnostic tools in medicine. These compounds, designed to possess high kinetic inertness and thermodynamic stability, displayed relaxation times consistent with high sensitivity for *in vivo* imaging. The Fe(II) contrast agents had relaxation parameters superior to any other ^{19}F MRI contrast agent described in the literature to date. *In vivo* experimentation demonstrated that four of the proposed agents produced no visible adverse effects on rats over a period of four hours, displayed adequate blood retention

time for imaging, and showed no abnormal accumulation in vital organs. With the observations made in this chapter, these compounds could serve as candidates for future in-depth pharmacological and toxicological testing that would further establish their suitability for ^{19}F MRI applications.

Combined with the results of the prior four chapters, this thesis is the first documented work that has examined and presented the design principles and behaviors of 19F MRI contrast agent systems in three areas: 1) theoretical predictions used to yield rational designs with high sensitivity and high water solubility, 2) demonstration that ^{19}F contrast agents can be responsive as well as ratiometric with a single probe, and 3) validation of their biocompatibility using *in vivo* models. Also reported herein are the first examples of ^{19}F contrast agents using Fe(II) as the paramagnetic metal ion that have been used *in vivo*. These results reported here represent significant advances in the field of ^{19}F MRI contrast agents to guide further studies in the area, and the improvements and observations made with these contrast agents could behave as templates for the production and study of future generations of ^{19}F MRI contrast agents for *in vivo* imaging.

5.6 Experimental Materials and Methods

General considerations. Starting materials were obtained from commercial suppliers and used without further purification. Water was distilled and further purified by a Millipore cartridge system (resistivity 1.8×10^7 Ω). All solvents were removed under reduced pressure with a rotary evaporator. All synthetic compounds were characterized at the LeClaire-Dow Chemical Instrumentation Facility at the Department of Chemistry at the University of Minnesota, Twin-Cities. ^{1}H NMR

spectra were recorded on a Varian VXR-300 at 300 MHz, ^{13}C NMR spectra at 75 MHz, ^{19}F NMR spectra at 282 MHz, and ^{31}P NMR spectra at 121 MHz, unless otherwise noted. The residual solvent peak was used as an internal reference for ^{1}H and ^{13}C NMR; $CFCl_3$ was used as an internal reference for ^{19}F NMR of organic intermediates; and KF was used as an external reference for tissue sample analysis. Data for ^{1}H NMR are reported as follows: chemical shift (δ, ppm), multiplicity (s, singlet; br s, broad singlet; d, doublet; t, triplet; q, quartet; quin, quintet; m, multiplet), integration, coupling constant (Hz). Data for ^{13}C, ^{19}F, and ^{31}P NMR are reported in terms of chemical shift (δ, ppm). Longitudinal (T_1) and transverse (T_2) relaxation times of ^{19}F nuclei of metal complexes in D_2O were measured using the inversion recovery sequence and the Carr-Purcell-Meiboom-Gill sequence, respectively, at 300 MHz. A delay time of 30 ms and acquisition time of 64 ms were used for the collection of ^{1}H and ^{19}F NMR spectra of the paramagnetic metal complexes. Mass spectra (HR, high resolution; ESI, electrospray ionization) were recorded on a Bruker BioTOF II at the Waters Center of Innovation for Mass Spectrometry at the Department of Chemistry at the University of Minnesota, Twin-Cities.

5.6.1 Synthesis of F-DOTPME (3-14), DOTAm-F12-PO_3 (5-13), and Metal Complexes

Tm(F-DOTPME)$^-$ (3-23). Ligand **3-14** (220 mg, 0.233 mmol) was dissolved in mQ water (15 mL). The solution was adjusted to pH = 7.5 with aq. HCl, and aq. thulium(III) chloride (0.291 M, 726 μL) was added. The pH was again adjusted to 7.5 with aq. NaOH. The reaction was stirred at 75 ºC for 72 h. Analysis using xylenol orange in phosphate buffer indicated the absence of free metal. The reaction was

lyophilized, yielding a white solid (**3-23**, 278 mg, quant.). ^{19}F NMR (282 MHz, D_2O) δ = -49.21, -54.25, -75.98, -76.37, -117.69, -118.15, -118.54, -118.79, -119.05, -119.48. ESI-MS [*m/z*] calc. for $C_{20}H_{32}F_{12}N_4O_{12}P_4Tm$ $[M]^-$: 1041.0, found: 1041.0.

Fe(F-DOTPME)$^{2-}$ (5-1). Ligand **3-14** (105 mg, 0.109 mmol) was dissolved in mQ water (1 mL). Then, methanol (14 mL) was added, and the reaction flask was flushed with argon for 15 minutes. Iron(II) trifluoromethanesulfonate (35.3 mg, 0.100 mmol) was added carefully to prevent introduction of air into the reaction. The reaction was stirred at 75 ºC for 48 h under Ar, then the temperature was increased to 90 ºC for 24 h to dry the reaction under Ar. The product was passed through a Sep-Pak Vac 6 cc (1 g) C18 cartridge (Waters) to exchange the coordinated trifluoromethanesulfonate ions with chloride. Briefly, the column was conditioned by eluting 1 volume (5 mL) of acetonitrile, followed by 1 volume of mQ water. The product, dissolved in mQ water (5 mL), was then deposited onto the column. 2 volumes of 1 M sodium chloride solution were passed through the column to perform ionic exchange, followed by 1 volume of mQ water to remove excess NaCl. Then, 2 volumes of acetonitrile were used to elute the product from the column as a pale yellow liquid. This liquid was lyophilized to yield the iron complex **5-1** as an orange powder. ^{19}F NMR (D_2O) δ = -73.73, -74.68. ESI-MS [*m/z*] calc. for $C_{20}H_{32}F_{12}N_4O_{12}P_4Fe$ $[M]^{2+}$: 464.0, found: 463.9.

Fe(DOTAm-F12)$^{2+}$ (2-11). Ligand **2-1** (50. mg, 68.7 μmol) was dissolved in methanol and acetonitrile (1:1, 25 mL) and magnetically stirred. Iron(II) trifluoromethanesulfonate (24.3 mg, 68.7 μmol) was added and the reaction mixture

was heated to 70ºC for 30 h under Ar (g). The resultant mixture was then concentrated under reduced pressure to yield the iron complex **2-11** as an orange solid in quantitative yield. Coordinated trifluoromethanesulfonate ions were exchanged for chloride by depositing the product on a Sep-Pak Vac 6 cc (1 g) C18 cartridge (Waters). The cartridge was washed with 2 volumes (5 mL each) of 1 M aqueous sodium chloride, followed by 1 volume of mQ water. The product was then eluted from the cartridge with 1 volume of acetonitrile. This eluent was collected and lyophilized to yield the desired product**.** ^{19}F NMR (D_2O) δ = -70.9 ppm. HRMS-ESI [*m/z*]: calc. for $C_{24}H_{36}F_{12}FeN_8O_4$ $[M]^{2+}$: 392.1009; found: 392.1000.

Diethyl (aminomethyl)phosphonate monooxalate (5-4). Diethyl ((1,3-dioxoisoindolin-2-yl)methyl)phosphonate (12.5 g, 42.1 mmol) was dissolved in absolute ethanol (250 mL). Hydrazine (1.68 mL, 52.6 mmol) was added, and the reaction was stirred for 18 hours at 22ºC as a white precipitate formed, followed by reflux at 100ºC for 3 hours. Next, mQ water (50 mL) was added to quench the remaining hydrazine, and the reaction was cooled to ambient temperature. The precipitate was removed by gravity filtration, and the remaining solution was concentrated under reduced pressure to 10 mL volume, then diluted with diethyl ether (250 mL) and filtered again. The solution was then added dropwise to a solution of oxalic acid (12.9 g, 143 mmol) in ethanol, forming the product as a white, flocculent precipitate. This precipitate was collected by vacuum filtration and dried under high vacuum (**5-4**, 4.85 g, 44.8%). ^{1}H NMR (500 MHz, D_2O) δ = 1.23 (t, *J* = 7.0 Hz, 6 H),

3.37 (d, J = 14 Hz, 2 H), 4.13 (tt, J_1 = 7.0 Hz, J_2 = 2.0 Hz, 4 H). ^{13}C NMR (125 MHz, D_2O) δ = 15.5, 33.0, 64.8, 165.0. ^{31}P NMR (201 MHz, D_2O) δ = 19.9.

Diethyl((2-bromoacetamido)methyl)phosphonate (5-5). The amine-phosphonate **5-4** (4.00 g, 16.5 mmol) was dissolved in a mixture of mQ water (25 mL) and methylene chloride (50 mL) and magnetically stirred in an ice bath. A solution of sodium hydroxide (2.50 g, 64.2 mmol) in water (50 mL) was added, followed by the dropwise addition of a solution of bromoacetyl bromide (2.03 mL, 23.3 mmol) in methylene chloride (10 mL) over 15 min. The reaction mixture was allowed to warm to ambient temperature and stirred for 70 min. The organic phase was separated and washed with water (5 × 25 mL), dried over $MgSO_4$ and concentrated under reduced pressure to yield the product as a colorless white crystal (**5-5**, 1.76 g, 60.3%). ^{1}H NMR (500 MHz, $CDCl_3$) δ = 1.34 (t, J = 7.0 Hz, 6 H), 3.72 (dd, J_1 = 12.5 Hz, J_2 = 6.0 Hz, 2 H), 3.90 (s, 2 H), 4.15 (quintet, J = 7.5 Hz, 4 H), 7.12 (br s, 1 H). ^{13}C NMR (125 MHz, $CDCl_3$) δ = 16.4, 35.6 (d, J = 156 Hz), 62.8, 165.7. ^{31}P NMR (201 MHz, $CDCl_3$) δ = 19.9 (s).

Diethyl ((2-(1,4,7,10-tetraazacyclododecan-1-yl)acetamido)methyl)phosphonate (5-6). Cyclen (10.6 g, 61.8 mmol) was dissolved in dry chloroform (300 mL), and the solution was magnetically stirred at room temperature. Triethylamine (1.03 mL, 7.42 mmol) was added, followed by the bromo-phosphonate arm **5-5** (1.76 g, 6.18 mmol). The reaction flask was then purged with Ar (g) and heated to 55 ºC under Ar (g) overnight. The reaction mixture was allowed to cool to ambient temperature and washed with 1 M aqueous sodium hydroxide (3 × 30 mL) and mQ water (3 × 50 mL),

dried over $MgSO_4$, filtered and concentrated under reduced pressure to yield the product as a clear colorless oil (**5-6**, 1.32 g, 56.6 %). ^{1}H NMR (500 MHz, $CDCl_3$) δ = 1.28 (t, *J* = 7.0 Hz, 6 H), 2.61-2.75 (m, 19 H), 3.18 (d, *J* = 5.5 Hz, 2 H), 3.69 (dd, J_1 = 11.5 Hz, J_2 = 5.0 Hz, 2 H), 4.08 (quintet, *J* = 7.0 Hz, 4 H), 9.09 (br s, 1 H). ^{13}C NMR (125 MHz, $CDCl_3$) δ = 16.5, 34.5 (d, *J* = 155 Hz), 47.4 (d, *J* = 64.8 Hz), 53.9, 58.9, 62.5, 172.2. ^{31}P NMR (201 MHz, $CDCl_3$) δ = 21.6 (s). HRMS-ESI [*m/z*] calc. for $C_{15}H_{34}N_5O_4P$ $[M + H]^+$: 380.2421, found 380.2416.

Diethyl ((2-(4,7,10-tris(2-oxo-2-((2,2,2-trifluoroethyl)amino)ethyl)-1,4,7,10-tetra azacyclododecan-1-yl)acetamido)methyl)phosphonate (5-7). The mono-substituted cyclen **5-6** (0.72 g, 1.90 mmol) was dissolved in acetonitrile (40 mL), and the solution was magnetically stirred. Potassium carbonate (4.20 g, 30.4 mmol) was added, followed by 2-bromo-*N*-(2,2,2-trifluoroethyl)acetamide (1.40 g, 6.27 mmol), and the reaction mixture was purged with Ar(g) and heated to 70 ºC overnight under Ar. The reaction mixture, which became orange overnight, was filtered and concentrated unde reduced pressure to yield an orange, translucent oil. The oil was suspended in water and chloroform (1:1, 200 mL), then washed with additional chloroform (2 × 25 mL) and diethyl ether (1 × 25 mL) before it was concentrated under reduced pressure to yield the protected ligand as an orange glass that was further dried under high vacuum overnight (**5-7**, 1.02 g, 53.7 %). ^{1}H NMR (500 MHz, CD_3OD) δ = 1.17 (t, *J* = 7.5 Hz, 6 H), 2.67-3.58 (m, 28 H), 3.93-4.09 (m, 8 H), 7.88 (br s, 3 H), 8.39 (br s, 1 H). HRMS-ESI [*m/z*] calc. for $C_{27}H_{46}F_9N_8O_7P$ $[M + Na]^+$: 819.2976, found 819.2989.

((2-(4,7,10-Tris(2-oxo-2-((2,2,2-trifluoroethyl)amino)ethyl)-1,4,7,10-tetraazacyclododecan-1-yl)acetamido)methyl)phosphonic acid (5-8, DOTAm-F9-PO_3): The diethyl-protected phosphonate ligand **5-7** (285 mg, 0.358 mmol) was dissolved in dry dimethylformamide (2 mL), and the reaction mixture was magnetically stirred. Trimethylsilylbromide (378 μL, 2.86 mmol) was added in four portions, causing a white smoke to evolve. The reaction mixture was stirred at room temperature overnight, after which methanol (5 mL) was added, and the reaction mixture was stirred for an additional 4 h. Volatiles were removed under reduced pressure to yield a brown gum. This gum was dissolved in 2 mL of a 0.1% TFA/H_2O mixture, and the resulting solution was purified by reverse-phase HPLC, eluting with 0-60% acetonitrile in 0.1% TFA/H_2O over 12 min., then 60% to 0% acetonitrile from 12-17 min. Fractions containing the product were collected and lyophilized to yield the product as a tetra-trifluoroacetic acid salt. The trifluoroacetate counter anions were removed by reacting the product with a high excess of propylene oxide (0.5 mL) at room temperature in the dark in methanol overnight; then the methanol and the remaining propylene oxide were removed under reduced pressure. The residue was subsequently washed and concentrated with methanol (3 x 5 mL), and then a methanol:diethyl ether (1:9) mixture, precipitating a white solid. The mixture was then concentrated under reduced pressure, dissolved in water (5 mL), and lyophilized to yield the free acid of ligand **5-8** as an off-white powder. (144 mg, 54.3%). ^{1}H NMR (500 MHz, D_2O) δ = 2.61-4.12 (m, 32 H). ^{19}F NMR (470 MHz) δ = -72.4 (t, J = 8.0 Hz), -72.3 (t, J = 8.0 Hz). ^{13}C NMR (125 MHz, D_2O) δ = 39.9 (d, J = 155 Hz), 54.6 (d,

J = 64.8 Hz), 54.4, 54.6, 55.1, 162.7, 163.0. HRMS-ESI [*m/z*] calc. for $C_{23}H_{38}F_9N_8O_7P$ $[M + H]^+$: 741.2530, found 741.2536.

Tm(DOTAm-F9-PO$_3$)$^+$ (5-2): The phosphonate ligand **5-8** (40 mg, 0.0540 mmol) was dissolved in mQ water (15 mL). The solution was adjusted to pH = 7 with dilute sodium hydroxide. Then, aqueous thulium(III) chloride (169 µL of 0.291 M solution) was added (0.0492 mmol, 0.91 eq). The pH was again adjusted to 7.4 with dilute sodium hydroxide. The reaction was stirred at 75ºC for 72 hours, with pH maintained between 7 and 8 daily. Xylenol orange test indicated that reaction had run to completion. Reaction was lyophilized, yielding the thulium complex as a white solid (**5-2**, 53 mg, 100%). ^{19}F NMR (D_2O) δ = -78.74, -86.41, -88.52. ESI-MS [*m/z*] calc. for $C_{23}H_{37}F_9N_8O_7P_4Tm$ $[M^{2+}]$: 454.1, found: 454.0.

Fe(DOTAm-F9-PO$_3$) (5-3): The phosphonate ligand **5-8** (139 mg, 0.188 mmol) was dissolved in mQ water (5 mL). Methanol (15 mL) was added, and the solution was magnetically stirred and flushed with Ar (g) for 30 minutes. Iron(II)trifluoromethanesulfonate (57.9 mg, 0.163 mmol) was added, and the reaction mixture was heated to 70ºC for 30 h under Ar (g). The resultant mixture was then concentrated under reduced pressure to yield the product **5-3** as an orange solid in quantitative yield. Coordinated trifluoromethanesulfonate ions were exchanged for chloride ions using a Sep-Pak Vac 6 cc (1 g) C18 cartridge (Waters). ^{19}F NMR (D_2O) δ = -70.50, -71.29. ESI-MS [*m/z*] calc. for $C_{23}H_{37}F_9FeN_8O_7$ $[M]^+$: 795.2; found: 795.2.

5.6.2 Testing For Free Metal Ions

Complex solutions were tested for unbound metal ions using xylenol orange as described by Averill et al.[207] Acetic acid (1.4 mL) was added to mQ water (400 mL), and the pH was adjusted to 5.8 using 1.0 M ammonium hydroxide. Additional mQ water was then added to bring the volume to 500 mL. An aliquot of this buffer was removed, and xylenol orange was added to produce a 16 μM solution. For each sample tested, 0.3 mg of the compound was added to 0.3 mL buffer, followed by 3 mL of the xylenol orange solution. A change in color from yellow to dark pink or violet indicated the presence of uncomplexed metal ions.

5.6.3 *In Vivo* Procedures

Female Sprague Dawley rats (230-250 g) fitted with jugular vein catheters were acquired from Harlan Labaratories (Madison, WI). Each contrast agent was prepared as a 50 mM solution in phosphate-buffered saline diluted with mQ water from a 10X commercial stock. 1 mL of this solution was injected into each animal through the catheter. Animals were then observed over a 4-hour period, with 500 μL blood samples collected through the catheter 5, 15, 30, 60, 120, and 240 minutes after administration of the complex. Following the final blood collection, the animals were euthanized with CO_2, and the brain, lung, liver, spleen, kidney, and heart were removed. Blood and organ samples were stored at 4ºC and -20ºC, respectively, until digestion. All animal experiments were conducted by Dr. Henry Wong of the Institute for Therapeutics Discovery and Development at the University of Minnesota. Protocols for animal experiments were generated by Dr. Wong and approved by the Institutional Animal Care and Use Committee at the University of Minnesota (protocol #1308-30830A).

5.6.4 Determination of Fluorine Concentration

Fluorine concentrations in blood and organ samples were determined following digestion in concentrated HNO_3. Each 500 µL blood sample was incubated with 500 µL concentrated nitric acid and stirred at 90 ºC for 15 h. For each organ sample, 3 mL concentrated nitric acid was used. Digestion yielded a clear, yellow liquid. The digested organ samples were reduced to a volume of 700 µL by removing solvent under reduced pressure.

Fluorine concentrations were then determined by ^{19}F NMR, referenced internally to aq. KF. Capillary tubes containing a 10 mM solution of KF in mQ water were prepared and flame sealed. A calibration curve was produced to determine the concentration of F^- in the capillary tubes. The capillary tube was inserted into an NMR tube containing 700 µL of potassium fluoride solutions in concentrated nitric acid with concentrations ranging from 30 to 300 ppm F^-. By comparing the ^{19}F NMR integration values of the capillary tube solution peak at -120 ppm with the main NMR tube solution peaks at -20 ppm, -76 ppm, -128 ppm, -148 ppm, and -164 ppm, the capillary tubes were determined to be equivalent to 38 ppm when inserted into a 700 µL external solution. All NMR spectra were gathered on a Varian 300 using delay time = 1.5 s, acquisition time = 600 ms, and number of transients = 1024. The standardized capillary tubes were then inserted into each 700 µL-volume digested blood or organ sample and scanned using the same parameters. The NMR integration values between the reference at δ = -120 ppm and the dominant resonance from the digested samples were compared to determine ^{19}F concentrations of each sample. Not all peaks were found in spectra for all samples.

References

(1) Control, C. f. D. **2013**.

(2) Damadian, R. *Science* **1971**, *171*, 1151.

(3) Damadian, R.; Zaner, K.; Hor, D.; DiMaio, T. *Proc Natl Acad Sci U S A* **1974**, *71*, 1471.

(4) Hollis, D. P., Economou, J. S., Parks, Leon C., Eggleston, Joseph C., Saryan, Leon A., Czeisler, Jeffrey L. *Cancer Research* **1973**, 2156.

(5) Hazlewood, C. F., Chang, D. C., Medina, D., Cleveland, G., Nichols, B. L. *Proc Natl Acad Sci U S A* **1972**, 1478.

(6) Merbach, A. E., Toth, E. *John Wiley and Sons* **2001**.

(7) Caravan, P.; Ellison, J. J.; McMurry, T. J.; Lauffer, R. B. *Chem Rev* **1999**, *99*, 2293.

(8) Aime, S.; Barge, A.; Botta, M.; Howard, J. A. K.; Kataky, R.; Lowe, M. P.; Moloney, J. M.; Parker, D.; de Sousa, A. S. *Chem Commun* **1999**, 1047.

(9) Yeh, T. C.; Zhang, W. G.; Ildstad, S. T.; Ho, C. *Magnet Reson Med* **1993**, *30*, 617.

(10) Moore, A.; Weissleder, R.; Bogdanov, A. *Jmri-J Magn Reson Im* **1997**, *7*, 1140.

(11) Weissleder, R.; Cheng, H. C.; Bogdanova, A.; Bogdanov, A. *Jmri-J Magn Reson Im* **1997**, *7*, 258.

(12) Sipe, J. C.; Filippi, M.; Martino, G.; Furlan, R.; Rocca, M. A.; Rovaris, M.; Bergami, A.; Zyroff, J.; Scotti, G.; Comi, G. *Magn Reson Imaging* **1999**, *17*, 1521.

(13) Modo, M.; Hoehn, M.; Bulte, J. W. M. *Mol Imaging* **2005**, *4*, 143.

(14) Laurent, S.; Forge, D.; Port, M.; Roch, A.; Robic, C.; Elst, L. V.; Muller, R. N. *Chem Rev* **2008**, *108*, 2064.

(15) Skjold, A.; Amundsen, B. H.; Wiseth, R.; Stoylen, A.; Haraldseth, O.; Larsson, H. B. W.; Jynge, P. *J Magn Reson Imaging* **2007**, *26*, 720.

(16) Small, W. C.; Macchi, D. D.; Parker, J. R.; Bernardino, M. E. *Acad Radiol* **1998**, *5*, S147.

(17) Wendland, M. F. *Nmr Biomed* **2004**, *17*, 581.

(18) Grobner, T. *Nephrol Dial Transpl* **2006**, *21*, 1104.

(19) High, W. A.; Ayers, R. A.; Chandler, J.; Zito, G.; Cowper, S. E. *J Am Acad Dermatol* **2007**, *56*, 21.

(20) Atanasijevic, T.; Zhang, X. A.; Lippard, S. J.; Jasanoff, A. *Inorg Chem* **2010**, *49*, 2589.

(21) Gilad, A. A.; Walczak, P.; McMahon, M. T.; Na, H. B.; Lee, J. H.; An, K.; Hyeon, T.; van Zijl, P. C. M.; Bulte, J. W. M. *Magnet Reson Med* **2008**, *60*, 1.

(22) Kim, T.; Momin, E.; Choi, J.; Yuan, K.; Zaidi, H.; Kim, J.; Park, M.; Lee, N.; McMahon, M. T.; Quinones-Hinojosa, A.; Bulte, J. W. M.; Hyeon, T.; Gilad, A. A. *J Am Chem Soc* **2011**, *133*, 2955.

(23) Taylor, K. M. L.; Rieter, W. J.; Lin, W. B. *J Am Chem Soc* **2008**, *130*, 14358.

(24) Aime, S.; Caravan, P. *J Magn Reson Imaging* **2009**, *30*, 1259.

(25) Nasu, H.; Takehara, Y.; Isogai, S.; Kodaira, N.; Takeda, H.; Saga, T.; Nakajima, S.; Sakata, I.; Sakahara, H. *J Magn Reson Imaging* **2004**, *20*, 294.

(26) Winter, M. B.; Klemm, P. J.; Phillips-Piro, C. M.; Raymond, K. N.; Marletta, M. A. *Inorg Chem* **2013**, *52*, 2277.

(27) Cheng, W. R.; Ganesh, T.; Martinez, F.; Lam, J.; Yoon, H.; Macgregor, R. B.; Scholl, T. J.; Cheng, H. L. M.; Zhang, X. A. *J Biol Inorg Chem* **2014**, *19*, 229.

(28) Qazi, S.; Uchida, M.; Usselman, R.; Shearer, R.; Edwards, E.; Douglas, T. *J Biol Inorg Chem* **2014**, *19*, 237.

(29) Harris, R. K.; Becker, E. D.; de Menezes, S. M. C.; Goodfellow, R.; Granger, P. *Solid State Nucl Mag* **2002**, *22*, 458.

(30) Code, R. F.; Harrison, J. E.; Mcneill, K. G.; Szyjkowski, M. *Magnet Reson Med* **1990**, *13*, 358.

(31) Harvey, P.; Kuprov, I.; Parker, D. *Eur. J. Inorg. Chem.* **2012**, 2015.

(32) Senanayake, P. K.; Kenwright, A. M.; Parker, D.; van der Hoorn, S. K. *Chem Commun* **2007**, 2923.

(33) Higuchi, M.; Iwata, N.; Matsuba, Y.; Sato, K.; Sasamoto, K.; Saido, T. C. *Nat Neurosci* **2005**, *8*, 527.

(34) Yu, J. X.; Liu, L.; Kodibagkar, V. D.; Cui, W. N.; Mason, R. P. *Biorg. Med. Chem.* **2006**, *14*, 326.

(35) Holland, G. N.; Bottomley, P. A.; Hinshaw, W. S. *Journal of Magnetic Resonance* **1977**, *28*, 133.

(36) Lauterbur, P. C. *Nature* **1973**, *242*, 190.

(37) Wolf, W.; Albright, M. J.; Silver, M. S.; Weber, H.; Reichardt, U.; Sauer, R. *Magn Reson Imaging* **1987**, *5*, 165.

(38) Li, C. W.; Negendank, W. G.; PadavicShaller, K. A.; ODwyer, P. J.; MurphyBoesch, J.; Brown, T. R. *Clin Cancer Res* **1996**, *2*, 339.

(39) Kuribayashi, H.; Doi, Y.; Kanazawa, Y. *Magnet Reson Med* **2001**, *46*, 864.

(40) Yu, J. X.; Kodibagkar, V. D.; Cui, W. N.; Mason, R. P. *Curr Med Chem* **2005**, *12*, 819.

(41) Partlow, K. C.; Chen, J. J.; Brant, J. A.; Neubauer, A. M.; Meyerrose, T. E.; Creer, M. H.; Nolta, J. A.; Caruthers, S. D.; Lanza, G. M.; Wickline, S. A. *Faseb J* **2007**, *21*, 1647.

(42) Hall, L. W., Jackson, S. R. K., Massey, G. M. *Oxford* **1975**.

(43) Park, B. K.; Kitteringham, N. R.; O'Neill, P. M. *Annu Rev Pharmacol* **2001**, *41*, 443.

(44) Flaherty, D. P.; Walsh, S. M.; Kiyota, T.; Dong, Y.; Ikezu, T.; Vennerstrom, J. L. *J Med Chem* **2007**, *50*, 4986.

(45) Flogel, U.; Ding, Z.; Hardung, H.; Jander, S.; Reichmann, G.; Jacoby, C.; Schubert, R.; Schrader, J. *Circulation* **2008**, *118*, 140.

(46) Kuethe, D. O.; Behr, V. C.; Begay, S. *Magnet Reson Med* **2002**, *48*, 547.

(47) Kauczor, H. U.; Chen, X. J.; van Beek, E. J. R.; Schreiber, W. G. *Eur Respir J* **2001**, *17*, 1008.

(48) Kenwright, A. M.; Kuprov, I.; De Luca, E.; Parker, D.; Pandya, S. U.; Senanayake, P. K.; Smith, D. G. *Chem Commun* **2008**, 2514.

(49) Kodibagkar, V. D.; Yu, J. X.; Liu, L.; Hetherington, H. P.; Mason, R. P. *Magn Reson Imaging* **2006**, *24*, 959.

(50) Sled, J. G.; Pike, G. B. *Journal of Magnetic Resonance* **2000**, *145*, 24.

(51) Alfakih, K.; Plein, S.; Thiele, H.; Jones, T.; Ridgway, J. P.; Sivananthan, M. U. *J Magn Reson Imaging* **2003**, *17*, 323.

(52) Oshio, K.; Feinberg, D. A. *Magnet Reson Med* **1991**, *20*, 344.

(53) Idiyatullin, D.; Corum, C.; Park, J. Y.; Garwood, M. *Journal of Magnetic Resonance* **2006**, *181*, 342.
(54) Idiyatullin, D.; Corum, C.; Moeller, S.; Garwood, M. *Journal of Magnetic Resonance* **2008**, *193*, 267.
(55) Gianolio, E.; Napolitano, R.; Fedeli, F.; Arena, F.; Aime, S. *Chem Commun* **2009**, 6044.
(56) Lauffer, R. B. *Chem. Rev.* **1987**, *87*, 901.
(57) Alsaadi, B. M.; Rossotti, F. J. C.; Williams, R. J. P. *J Chem Soc Dalton* **1980**, 2151.
(58) Alsaadi, B. M.; Rossotti, F. J. C.; Williams, R. J. P. *J Chem Soc Dalton* **1980**, 813.
(59) Smolensky, E. D.; Marjanska, M.; Pierre, V. C. *Dalton T* **2012**, *41*, 8039.
(60) Deutsch, C. J.; Taylor, J. S. *Biophys J* **1989**, *55*, 799.
(61) Vervoort, J.; Rietjens, I. M. C. M.; Moonen, C. T. W.; Vonkienlin, M.; Despres, D. *Nmr Biomed* **1991**, *4*, 255.
(62) Mizukami, S.; Takikawa, R.; Sugihara, F.; Hori, Y.; Tochio, H.; Walchli, M.; Shirakawa, M.; Kikuchi, K. *J Am Chem Soc* **2008**, *130*, 794.
(63) Takaoka, Y.; Kiminami, K.; Mizusawa, K.; Matsuo, K.; Narazaki, M.; Matsuda, T.; Hamachi, I. *J Am Chem Soc* **2011**, *133*, 11725.
(64) Wang, K.; Peng, H.; Thurecht, K. J.; Puttick, S.; Whittaker, A. K. *Polymer Chemistry* **2013**, *4*, 4480.
(65) Hendrick, R. E.; Kneeland, J. B.; Stark, D. D. *Magnetic Resonance Imaging* **1987**, *5*, 117.
(66) Janjic, J. M.; Srinivas, M.; Kadayakkara, D. K. K.; Ahrens, E. T. *J. Am. Chem. Soc.* **2008**, *130*, 2832.
(67) Nurmi, L.; Peng, H.; Seppala, J.; Haddleton, D. M.; Blakey, I.; Whittaker, A. K. *Polymer Chemistry* **2010**, *1*, 1039.
(68) Jiang, Z.-X.; Feng, Y.; Yu, Y. B. *Chem. Commun.* **2011**, *47*, 7233.
(69) Rossi, S.; Benaglia, M.; Ortenzi, M.; Micotti, E.; Perego, C.; De Simoni, M. G. *Tetrahedron Lett.* **2011**, *52*, 6581.
(70) Criscione, J. M.; Le, B. L.; Stern, E.; Brennan, M.; Rahner, C.; Papademetris, X.; Fahmy, T. M. *Biomaterials* **2009**, *30*, 3946.
(71) Peng, H.; Blakey, I.; Dargaville, B.; Rasoul, F.; Rose, S.; Whittaker, A. K. *Biomacromolecules* **2009**, *10*, 374.
(72) Ogawa, M.; Nitahara, S.; Aoki, H.; Ito, S.; Narazaki, M.; Matsuda, T. *Macromol. Chem. Phys.* **2010**, *211*, 1602.
(73) Ogawa, M.; Nitahara, S.; Aoki, H.; Ito, S.; Narazaki, M.; Matsuda, T. *Macromol. Chem. Phys.* **2010**, *211*, 1369.
(74) Ogawa, M.; Kataoka, H.; Nitahara, S.; Fujimoto, H.; Aoki, H.; Ito, S.; Narazaki, M.; Matsuda, T. *Bull. Chem. Soc. Jpn.* **2012**, *85*, 79.
(75) Du, W.; Xu, Z.; Nyström, A. M.; Zhang, K.; Leonard, J. R.; Wooley, K. L. *Bioconjugate Chem.* **2008**, *19*, 2492.
(76) Du, W.; Nystrom, A. M.; Zhang, L.; Powell, K. T.; Li, Y.; Cheng, C.; Wickline, S. A.; Wooley, K. L. *Biomacromolecules* **2008**, *9*, 2826.
(77) Thurecht, K. J.; Blakey, I.; Peng, H.; Squires, O.; Hsu, S.; Alexander, C.; Whittaker, A. K. *J. Am. Chem. Soc.* **2010**, *132*, 5336.

(78) Neubauer, A. M.; Myerson, J.; Caruthers, S. D.; Hockett, F. D.; Winter, P. M.; Chen, J.; Gaffney, P. J.; Robertson, J. D.; Lanza, G. M.; Wickline, S. A. *Magnetic Resonance in Medicine* **2008**, *60*, 1066.

(79) Caruthers, S. D.; Neubauer, A. M.; Hockett, F. D.; Lamerichs, R.; Winter, P. M.; Scott, M. J.; Gaffney, P. J.; Wickline, S. A.; Lanza, G. M. *Invest Radiol* **2006**, *41*, 305.

(80) Takaoka, Y.; Kiminami, K.; Mizusawa, K.; Matsuo, K.; Narazaki, M.; Matsuda, T.; Hamachi, I. *J. Am. Chem. Soc.* **2011**, *133*, 11725.

(81) Chalmers, K. H.; Botta, M.; Parker, D. *Dalton Transactions* **2011**, *40*, 904.

(82) Chalmers, K. H.; De Luca, E.; Hogg, N. H. M.; Kenwright, A. M.; Kuprov, I.; Parker, D.; Botta, M.; Wilson, J. I.; Blamire, A. M. *Chem-Eur J* **2010**, *16*, 134.

(83) Chalmers, K. H.; Kenwright, A. M.; Parker, D.; Blamire, A. M. *Magnetic Resonance in Medicine* **2011**, *66*, 931.

(84) Kim, W. D.; Kiefer, G. E.; Huskens, J.; Sherry, A. D. *Inorg Chem* **1997**, *36*, 4128.

(85) Harvey, P.; Chalmers, K. H.; De Luca, E.; Mishra, A.; Parker, D. *Chemistry-a European Journal* **2012**, *18*, 8748.

(86) Placidi, M. P.; Botta, M.; Kálmán, F. K.; Hagberg, G. E.; Baranyai, Z.; Krenzer, A.; Rogerson, A. K.; Tóth, I.; Logothetis, N. K.; Angelovski, G. *Chemistry – A European Journal* **2013**, *19*, 11644.

(87) Tsitovich, P. B.; Morrow, J. R. *Inorg. Chim. Acta* **2012**, *393*, 3.

(88) Dorazio, S. J.; Olatunde, A. O.; Tsitovich, P. B.; Morrow, J. R. *J Biol Inorg Chem* **2014**, *19*, 191.

(89) Dorazio, S. J.; Tsitovich, P. B.; Siters, K. E.; Spernyak, J. A.; Morrow, J. R. *J. Am. Chem. Soc.* **2011**, *133*, 14154.

(90) Crull, G. B.; Kennington, J. W.; Garber, A. R.; Ellis, P. D.; Dawson, J. H. *J. Biol. Chem.* **1989**, *264*, 2649.

(91) Tierney, D. L.; Gassner, G. T.; Luchinat, C.; Bertini, I.; Ballou, D. P.; Penner-Hahn, J. E. *Biochemistry* **1999**, *38*, 11051.

(92) Belle, C.; Béguin, C.; Hamman, S.; Pierre, J.-L. *Coord. Chem. Rev.* **2009**, *253*, 963.

(93) Tanaka, K.; Kitamura, N.; Takahashi, Y.; Chujo, Y. *Bioorg Med Chem* **2009**, *17*, 3818.

(94) Mandal, S. K.; Que, L. *Inorg. Chem.* **1997**, *36*, 5424.

(95) Bleaney, B. *Journal of Magnetic Resonance (1969)* **1972**, *8*, 91.

(96) Alpoim, M. C.; Urbano, A. M.; Geraldes, C. F. G. C.; Peters, J. A. *Journal of the Chemical Society-Dalton Transactions* **1992**, 463.

(97) Aime, S.; Barge, A.; Bruce, J. I.; Botta, M.; Howard, J. A. K.; Moloney, J. M.; Parker, D.; de Sousa, A. S.; Woods, M. *J Am Chem Soc* **1999**, *121*, 5762.

(98) Beeby, A.; M. Clarkson, I.; S. Dickins, R.; Faulkner, S.; Parker, D.; Royle, L.; S. de Sousa, A.; A. Gareth Williams, J.; Woods, M. *J. Chem. Soc., Perkin Trans. 2* **1999**, 493.

(99) Parker, D.; Dickins, R. S.; Puschmann, H.; Crossland, C.; Howard, J. A. K. *Chem. Rev.* **2002**, *102*, 1977.

(100) Di Bari, L.; Salvadori, P. *Chemphyschem* **2011**, *12*, 1490.

(101) Frisch, M. J. T., G. W.; Schlegel, H. B.; Scuseria, G. E.; Robb, M. A.; Cheeseman, J. R.; Scalmani, G.; Barone, V.; Mennucci, B.; Petersson, G. A.; Nakatsuji, H.; Caricato, M.; Li, X.; Hratchian, H. P.; Izmaylov, A. F.; Bloino, J.; Zheng, G.; Sonnenberg, J. L.; Hada, M.; Ehara, M.; Toyota, K.; Fukuda, R.; Hasegawa, J.; Ishida, M.; Nakajima, T.; Honda,

Y.; Kitao, O.; Nakai, H.; Vreven, T.; Montgomery, J. A., Jr.; Peralta, J. E.; Ogliaro, F.; Bearpark, M.; Heyd, J. J.; Brothers, E.; Kudin, K. N.; Staroverov, V. N.; Kobayashi, R.; Normand, J.; Raghavachari, K.; Rendell, A.; Burant, J. C.; Iyengar, S. S.; Tomasi, J.; Cossi, M.; Rega, N.; Millam, N. J.; Klene, M.; Knox, J. E.; Cross, J. B.; Bakken, V.; Adamo, C.; Jaramillo, J.; Gomperts, R.; Stratmann, R. E.; Yazyev, O.; Austin, A. J.; Cammi, R.; Pomelli, C.; Ochterski, J. W.; Martin, R. L.; Morokuma, K.; Zakrzewski, V. G.; Voth, G. A.; Salvador, P.; Dannenberg, J. J.; Dapprich, S.; Daniels, A. D.; Farkas, Ö.; Foresman, J. B.; Ortiz, J. V.; Cioslowski, J.; Fox, D. J. *Gaussian 09, Revision D.01*; Gaussian, Inc.: Wallingford CT, 2009.

(102) Dolg, M.; Stoll, H.; Preuss, H. *Theoretica chimica acta* **1993**, *85*, 441.

(103) Dolg, M.; Stoll, H.; Savin, A.; Preuss, H. *Theoretica chimica acta* **1989**, *75*, 173.

(104) Platas-Iglesias, C. *Eur. J. Inorg. Chem.* **2012**, *2012*, 2023.

(105) Amin, S.; Voss, D. A.; Horrocks, W. D.; Lake, C. H.; Churchill, M. R.; Morrow, J. R. *Inorg. Chem.* **1995**, *34*, 3294.

(106) Dickins, R. S.; Howard, J. A. K.; Maupin, C. L.; Moloney, J. M.; Parker, D.; Riehl, J. P.; Siligardi, G.; Williams, J. A. G. *Chem-Eur J* **1999**, *5*, 1095.

(107) Berger, R.; Resnati, G.; Metrangolo, P.; Weber, E.; Hulliger, J. *Chem. Soc. Rev.* **2011**, *40*, 3496.

(108) Jacoby, C.; Temme, S.; Mayenfels, F.; Benoit, N.; Krafft, M. P.; Schubert, R.; Schrader, J.; Flogel, U. *Nmr Biomed* **2014**, *27*, 261.

(109) Harvey, P.; Kuprov, I.; Parker, D. *Eur. J. Inorg. Chem.* **2012**, 2015.

(110) Bertini, I.; Turano, P.; Vila, A. J. *Chem. Rev.* **1993**, *93*, 2833.

(111) Bertini, I.; Capozzi, F.; Luchinat, C.; Nicastro, G.; Xia, Z. C. *J. Phys. Chem.* **1993**, *97*, 6351.

(112) Peters, J. A.; Huskens, J.; Raber, D. J. *Prog Nucl Mag Res Sp* **1996**, *28*, 283.

(113) Christian, G. D.; Dasgupta, P.; Schug, K. *Analytical Chemistry*; 7th ed.; John Wiley & Sons: New YorkS, 2014.

(114) Godek, M. L.; Michel, R.; Chamberlain, L. M.; Castner, D. G.; Grainger, D. W. *Journal of biomedical materials research. Part A* **2009**, *88*, 503.

(115) Kiaei, D.; Hoffman, A. S.; Horbett, T. A. *J Biomater Sci Polym Ed.* **1992**, *4*, 35.

(116) De Luca, E.; Harvey, P.; Chalmers, K.; Mishra, A.; Senanayake, P. K.; Wilson, J. I.; Botta, M.; Fekete, M.; Blamire, A.; Parker, D. *J. Biol. Inorg. Chem.* **2013**, 1.

(117) Idiyatullin, D.; Corum, C.; Park, J.-Y.; Garwood, M. *Journal of Magnetic Resonance* **2006**, *181*, 342.

(118) *SMART V5.054, Bruker Analytical X-ray Systems* Madison, WI 2001.

(119) Blessing, R. *Acta Cryst.* **1995**, *A51*, 33.

(120) *SAINT+ V6.45, Bruker Analytical X-Ray Systems* Madison, WI, 2003.

(121) *SHELXTL V6.14, Bruker Analytical X-Ray Systems* Madison, WI, 2000.

(122) Spek, A. L. *Acta Cryst.* **1990**, *A46*, C34.

(123) Spek, A. L. *PLATON, A Multipurpose Crystallographic Tool* Utrecht University, Utrecht, The Netherlands, 2000.

(124) Solomon, I. *Physical Review* **1955**, *99*, 559.

(125) Bloembergen, N. M., L. O. *J. Chem. Phys.* **1961**, *34*, 842.

(126) Chalmers, K. H.; Kenwright, A. M.; Parker, D.; Blamire, A. M. *Magnet Reson Med* **2011**, *66*, 931.

(127) Ren, J.; Whangbo, M. H.; Dai, D. D.; Li, L. M. *J Chem Phys* **1998**, *108*, 8479.

(128) Ishikawa, N. *J Phys Chem A* **2003**, *107*, 5831.

(129) Ishikawa, N.; Iino, T.; Kaizu, Y. *J Phys Chem A* **2002**, *106*, 9543.
(130) Zbiri, M.; Daul, C. A.; Wesolowski, T. A. *J Chem Theory Comput* **2006**, *2*, 1106.
(131) Ishikawa, N.; Sugita, M.; Okubo, T.; Tanaka, N.; Lino, T.; Kaizu, Y. *Inorg Chem* **2003**, *42*, 2440.
(132) Bleaney, B. *J. Magn. Reson.* **1972**, *8*, 91.
(133) Alsaadi, B. M.; Rossotti, F. J. C.; Williams, R. J. P. *J Chem Soc Dalton* **1980**, 2147.
(134) Aime, S.; Barbero, L.; Botta, M.; Ermondi, G. *J Chem Soc Dalton* **1992**, 225.
(135) Bertini, I.; Capozzi, F.; Luchinat, C.; Nicastro, G.; Xia, Z. C. *J Phys Chem-Us* **1993**, *97*, 6351.
(136) Funk, A. M.; Harvey, P.; Finney, K. L. N. A.; Fox, M. A.; Kenwright, A. M.; Rogers, N. J.; Senanayake, P. K.; Parker, D. *Phys Chem Chem Phys* **2015**, *17*, 16507.
(137) Bertini, I.; Turano, P.; Vila, A. J. *Chem Rev* **1993**, *93*, 2833.
(138) Chevalier, B. T., S.; Andre, G.; Matier, S. F.; Gaudin, E. *J. Phys. Conf., Ser.* **2010**, *200*.
(139) Gignoux, D.; Schmitt, D.; Zerguine, M. *J Magn Magn Mater* **1987**, *66*, 373.
(140) Quadrelli, E. A. *Inorg Chem* **2002**, *41*, 167.
(141) Liu, Q. D.; Gao, S.; Li, J. R.; Ma, B. Q.; Zhou, Q. Z.; Yu, K. B. *Polyhedron* **2002**, *21*, 1097.
(142) Seitz, M.; Oliver, A. G.; Raymond, K. N. *J Am Chem Soc* **2007**, *129*, 11153.
(143) Geraldes, C. F. G. C.; Sherry, A. D.; Lazar, I.; Miseta, A.; Bogner, P.; Berenyi, E.; Sumegi, B.; Kiefer, G. E.; Mcmillan, K.; Maton, F.; Muller, R. N. *Magnet Reson Med* **1993**, *30*, 696.
(144) Luz, Z. M., S. *J. Chem. Phys.* **1964**, *40*, 2686.
(145) Raghunand, N.; Zhang, S. R.; Sherry, A. D.; Gillies, R. J. *Acad. Radiol.* **2002**, *9*, S481.
(146) De, L.-R. L. M.; Lubag, A. J. M.; Malloy, C. R.; Martinez, G. V.; Gillies, R. J.; Sherry, A. D. *Acc. Chem. Res.* **2009**, *42*, 948.
(147) De Leon-Rodriguez, L. M.; Lubag, A. J. M.; Malloy, C. R.; Martinez, G. V.; Gillies, R. J.; Sherry, A. D. *Accounts Chem Res* **2009**, *42*, 948.
(148) Borden, M. A.; Zhang, H.; Gillies, R. J.; Dayton, P. A.; Ferrara, K. W. *Biomaterials* **2007**, *29*, 597.
(149) Gillies, R. J.; Raghunand, N.; Garcia-Martin, M. L.; Gatenby, R. A. *IEEE Eng. Med. Biol. Mag.* **2004**, *23*, 57.
(150) Garcia-Martin, M. L.; Martinez, G. V.; Raghunand, N.; Sherry, A. D.; Zhang, S. R.; Gillies, R. J. *Magn. Res. Med.* **2006**, *55*, 309.
(151) Raghunand, N.; Howison, C.; Sherry, A. D.; Zhang, S. R.; Gillies, R. J. *Magn. Res. Med.* **2003**, *49*, 249.
(152) Yu, J. X.; Otten, P.; Ma, Z. Y.; Cui, W. N.; Liu, L.; Mason, R. P. *Bioconjugate Chem.* **2004**, *15*, 1334.
(153) He, S.; Mason, R. P.; Hunjan, S.; Mehta, V. D.; Arora, V.; Katipally, R.; Kulkarni, P. V.; Antich, P. P. *Bioorgan Med Chem* **1998**, *6*, 1631.
(154) Mason, R. P. *Curr. Med. Chem.* **1999**, *6*, 481.
(155) Yu, J. X.; Kodibagkar, V. D.; Cui, W. N.; Mason, R. P. *Curr. Med. Chem.* **2005**, *12*, 819.
(156) Liu, L.; Kodibagkar, V. D.; Yu, J.-X.; Mason, R. P. *FASEB J.* **2007**, *21*, 2014.

(157) Mehta, V. D.; Kulkarni, P. V.; Mason, R. P.; Constantinescu, A.; Aravind, S.; Goomer, N.; Antich, P. P. *FEBS Lett.* **1994**, *349*, 234.

(158) Zhao, D. W.; Jiang, L.; Mason, R. P. *Imag. Biol. Res., Pt B* **2004**, *386*, 378.

(159) Hunjan, S.; Zhao, D. W.; Constantinescu, A.; Hahn, E. W.; Antich, P. P.; Mason, R. P. *Int. J. Rad. Onc. Biol. Phys.* **2001**, *49*, 1097.

(160) Mason, R. P.; Ran, S.; Thorpe, P. E. *J. Cell. Biochem.* **2002**, 45.

(161) Yu, J. X.; Mason, R. P. *J. Med. Chem.* **2006**, *49*, 1991.

(162) Kodibagkar, V. D.; Yu, J.; Liu, L.; Hetherington, H. P.; Mason, R. P. *Magn. Res. Im.* **2006**, *24*, 959.

(163) Cui, W. N.; Otten, P.; Li, Y. M.; Koeneman, K. S.; Yu, J. X.; Mason, R. P. *Magn. Res. Med.* **2004**, *51*, 616.

(164) Hunjan, S.; Mason, R. P.; Mehta, V. D.; Kulkarni, P. V.; Aravind, S.; Arora, V.; Antich, P. P. *Magn. Res. Med.* **1998**, *39*, 551.

(165) Yu, J.; Ma, Z.; Li, Y.; Koeneman, K. S.; Liu, L.; Mason, R. P. *Med. Chem.* **2005**, *1*, 255.

(166) Yu, J.-X.; Kodibagkar, V. D.; Liu, L.; Mason, R. P. *NMR Biomed.* **2008**, *21*, 704.

(167) Srinivas, M.; Morel, P. A.; Ernst, L. A.; Laidlaw, D. H.; Ahrens, E. T. *Magn. Res. Med.* **2007**, *58*, 725.

(168) Janjic, J. M.; Ahrens, E. T. *Nanomed. Nanobiotechnol.* **2009**, *1*, 492.

(169) Srinivas, M.; Turner, M. S.; Janjic, J. M.; Morel, P. A.; Laidlaw, D. H.; Ahrens, E. T. *Magn. Res. Med.* **2009**, *62*, 747.

(170) Helfer, B. M.; Balducci, A.; Nelson, A. D.; Janjic, J. M.; Gil, R. R.; Kalinski, P.; de Vries, I. J. M.; Ahrens, E. T.; Mailliard, R. B. *Cytotherapy* **2010**, *12*, 238.

(171) Kadayakkara, D. K. K.; Janjic, J. M.; Pusateri, L. K.; Young, W.-B.; Ahrens, E. T. *Magn. Res. Med.* **2010**, *64*, 1252.

(172) Srinivas, M.; Heerschap, A.; Ahrens, E. T.; Figdor, C. G.; Vries, I. J. M. d. *Trends Biotechnol.* **2010**, *28*, 363.

(173) Bonetto, F.; Srinivas, M.; Heerschap, A.; Mailliard, R.; Ahrens, E. T.; Figdor, C. G.; de Vries, I. J. M. *Int, J. Cancer* **2011**, *129*, 365.

(174) Hitchens, T. K.; Ye, Q.; Eytan, D. F.; Janjic, J. M.; Ahrens, E. T.; Ho, C. *Magn. Res. Med.* **2011**, *65*, 1144.

(175) Balducci, A.; Helfer, B.; Ahrens, E.; O'Hanlon, C.; Wesa, A. *J. Inflam.* **2012**, *9*, 24.

(176) Bible, E.; Dell'Acqua, F.; Solanky, B.; Balducci, A.; Crapo, P. M.; Badylak, S. F.; Ahrens, E. T.; Modo, M. *Biomaterials* **2012**, *33*, 2858.

(177) Kadayakkara, D. K.; Ranganathan, S.; Young, W.-B.; Ahrens, E. T. *Lab. Invest.* **2012**, *92*, 636.

(178) Ruiz-Cabello, J.; Barnett, B. P.; Bottomley, P. A.; Bulte, J. W. M. *NMR Biomed.* **2011**, *24*, 114.

(179) Yu, J.-X.; Hallac, R. R.; Chiguru, S.; Mason, R. P. *Prog. Nucl. Magn. Reson. Spectrosc.* **2013**, *70*, 25.

(180) Que, E. L.; Chang, C. J. *J Am Chem Soc* **2006**, *128*, 15942.

(181) Que, E. L.; Chang, C. J. *Chem Soc Rev* **2010**, *39*, 51.

(182) Que, E. L.; Domaille, D. W.; Chang, C. J. *Chem Rev* **2008**, *108*, 4328.

(183) Que, E. L.; Domaille, D. W.; Chang, C. J. *Chem Rev* **2008**, *108*, 1517.

(184) Que, E. L.; Gianolio, E.; Baker, S. L.; Aime, S.; Chang, C. J. *Dalton T* **2010**, *39*, 469.

(185) Que, E. L.; Gianolio, E.; Baker, S. L.; Wong, A. P.; Aime, S.; Chang, C. J. *J Am Chem Soc* **2009**, *131*, 8527.

(186) Que, E. L.; New, E. J.; Chang, C. J. *Chem Sci* **2012**, *3*, 1829.

(187) Squitti, R.; Quattrocchi, C. C.; Salustri, C.; Rossini, P. M. *Prion* **2008**, *2*, 23.

(188) Kardos, J.; Kovacs, I.; Hajos, F.; Kalman, M.; Simonyi, M. *Neurosci Lett* **1989**, *103*, 139.

(189) Maynard, C. J.; Bush, A. I.; Masters, C. L.; Cappai, R.; Li, Q. X. *Int J Exp Pathol* **2005**, *86*, 147.

(190) Hureau, C.; Faller, P. *Biochimie* **2009**, *91*, 1212.

(191) Allegrozzi, M.; Bertini, I.; Janik, M. B. L.; Lee, Y.-M.; Liu, G.; Luchinat, C. *J. Am. Chem. Soc.* **2000**, *122*, 4154.

(192) McConnell, H. M.; Robertson, R. E. *J. Chem. Phys.* **1958**, *29*, 1361.

(193) Peters, J. A.; Huskens, J.; Raber, D. J. *Prog. Nucl. Magn. Reson. Spectrosc.* **1996**, *28*, 283.

(194) Wangsness, R. K.; Bloch, F. *Phys. Rev.* **1953**, *89*, 728.

(195) Redfield, A. G. *IBM J. Res. Dev.* **1957**, *1*, 19.

(196) Kubo, R. *Hyperfine Interact.* **1981**, *8*, 731.

(197) Frenzel, T.; Lengsfeld, P.; Schirmer, H.; Hutter, J.; Weinmann, H. J. *Invest Radiol* **2008**, *43*, 817.

(198) Jiang, Z. X.; Liu, X.; Jeong, E. K.; Yu, Y. B. *Angewandte Chemie-International Edition* **2009**, *48*, 4755.

(199) Jiang, Z. X.; Feng, Y.; Yu, Y. B. *Chem Commun* **2011**, *47*, 7233.

(200) Pereira, G. A.; Ball, L.; Sherry, A. D.; Peters, J. A.; Geraldes, C. E. G. C. *Helv Chim Acta* **2009**, *92*, 2532.

(201) Woods, M.; Caravan, P.; Geraldes, C. F. G. C.; Greenfield, M. T.; Kiefer, G. E.; Lin, M.; McMillan, K.; Prata, M. I. M.; Santos, A. C.; Sun, X. K.; Wang, J. F.; Zhang, S. R.; Zhao, P. Y.; Sherry, A. D. *Invest Radiol* **2008**, *43*, 861.

(202) Agalakova, N. I.; Gusev, G. P. *Biol Trace Elem Res* **2013**, *153*, 340.

(203) Pierre, V. C.; Allen, M. J.; Caravan, P. *J Biol Inorg Chem* **2014**, *19*, 127.

(204) Chin-Thin, W.; Wei-Tun, C.; Tzu-Ming, P.; Ren-Tse, W. *Clin Chem Lab Med* **2002**, *40*, 1118.

(205) Ganz, T. *Physiol Rev* **2013**, *93*, 1721.

(206) Dorazio, S. J.; Tsitovich, P. B.; Gardina, S. A.; Morrow, J. R. *J Inorg Biochem* **2012**, *117*, 212.

(207) Averill, D. J.; Garcia, J.; Siriwardena-Mahanama, B. N.; Vithanarachchi, S. M.; Allen, M. J. *Jove-J Vis Exp* **2011**.